

August 2023

Topological Superconductors and Dark Matter Searches in Gravitational Wave Interferometers

Han Gyeol Suh
University of Wisconsin-Milwaukee

Follow this and additional works at: <https://dc.uwm.edu/etd>



Part of the [Physics Commons](#)

Recommended Citation

Suh, Han Gyeol, "Topological Superconductors and Dark Matter Searches in Gravitational Wave Interferometers" (2023). *Theses and Dissertations*. 3359.
<https://dc.uwm.edu/etd/3359>

This Dissertation is brought to you for free and open access by UWM Digital Commons. It has been accepted for inclusion in Theses and Dissertations by an authorized administrator of UWM Digital Commons. For more information, please contact scholarlycommunicationteam-group@uwm.edu.

TOPOLOGICAL SUPERCONDUCTORS AND DARK MATTER
SEARCHES IN GRAVITATIONAL WAVE INTERFEROMETERS

by
Han Gyeol Suh

A Dissertation Submitted in
Partial Fulfillment of the
Requirements for the Degree of

Doctor of Philosophy
in Physics

at
The University of Wisconsin-Milwaukee
August 2023

ABSTRACT

TOPOLOGICAL SUPERCONDUCTORS AND DARK MATTER SEARCHES IN GRAVITATIONAL WAVE INTERFEROMETERS

by

Han Gyeol Suh

The University of Wisconsin-Milwaukee, 2023

Under the Supervision of Professor Daniel F. Agterberg and Professor Jolien D. Creighton

This work is comprised of research in two areas: superconductors and gravitational waves.

Superconductors have led to novel fundamental discoveries, including new topological states. These states are robust, in that they are not altered by common changes to their environment. Here, I will introduce three studies focused on topological properties of various superconductors. First, newly proposed even-parity superconducting state in Sr_2RuO_4 introduces the emergence of topologically protected Bogoliubov Fermi surfaces. Next, I will discuss topological bands and odd-parity superconductivity in UTe_2 , which suggest Weyl nodes and their potential topological properties. Lastly, anomalous pseudospin in non-symmorphic materials shows different symmetry properties than the usual spin-1/2 and has its applications on BiS_2 , UPt_3 , Fe-based superconductors, and UCoGe .

LIGO and Virgo are laser interferometers designed to detect gravitational waves, enabling a variety of physical analyses. One important aspect involves measuring the spacetime volume sensitivity $\langle VT \rangle$. The researchers typically inject simulated signals to measure $\langle VT \rangle$ which is computationally expensive. I will present a machine learning method to reduce the computational cost of this process. Furthermore, these detectors can conduct dark matter searches. My research proposes a hypothesis that dark matter particles decay into gravitational waves, producing detectable blip glitches, which have traditionally been considered as noise. I will present a dimensional and data analysis to test the plausibility of my hypothesis.

© Copyright by Han Gyeol Suh, 2023
All Rights Reserved

To my family, friends, and Ji-In Jung for all their love and support throughout this endeavor.

TABLE OF CONTENTS

1 Superconducting Materials	1
1.1 Overview	1
1.2 Bogoliubov Fermi Surfaces - Sr_2RuO_4	3
1.2.1 Introduction	3
1.2.2 Normal-state Hamiltonian	4
1.2.3 Interactions and superconductivity	5
1.2.4 Results	7
1.2.5 Bogoliubov Fermi surfaces	10
1.2.6 Conclusions	11
1.3 Weyl point nodes - UTe_2	11
1.3.1 Introduction	11
1.3.2 Topological Band	13
1.3.3 Minimal Hamiltonian	14
1.3.4 Magnetic interactions	16
1.3.5 Role of H_N	17
1.3.6 Experimental Constraints	17
1.3.7 Weyl Nodes	18
1.3.8 Polar Kerr Effect	19
1.4 Anomalous Pseudospin	20
1.4.1 Introduction	20
1.4.2 Anomalous pseudospin: symmetry origin	23

1.4.3	Nodal plane space groups and single-particle kp Hamiltonians	25
1.4.4	Superconducting states	32
1.4.5	Role of Magnetic Fields	39
1.4.6	8-fold degenerate points: application to UCoGe	48
1.4.7	Conclusions	50
2	Gravitational Wave Physics	51
2.1	Overview	51
2.2	Determining LIGO Spacetime Volume Sensitivity by Machine Learning	52
2.2.1	Introduction	52
2.2.2	Deep Neural Network(DNN)	53
2.2.3	Spacetime-Volume Sensitivity $\langle VT \rangle$	54
2.2.4	Methods and Results	55
2.2.5	Discussion	57
2.3	Dark Matter Evidence in Blip Glitches	59
2.3.1	Introduction	59
2.3.2	Dark matter decay and blip glitch rates	60
2.3.3	Gabor-Morlet Wavelet Model	61
2.3.4	Dark matter parameters estimation	63
2.3.5	Bayesian statistics	65
2.3.6	Discussion	66
	Bibliography	67
	Appendix	82
A.1	ML model performance figures	82

LIST OF FIGURES

1-1	(a)Phase diagram showing the stability of A_{1g} and E_g pairing states and (b)Fermi-surface shapes	8
1-2	Projected gaps at the Fermi surfaces for different symmetry channels	9
1-3	BFSs for the chiral E_g state	10
1-4	(a) LDA+ U band dispersion along k_z axis (Λ line) and (b) Density of states	12
1-5	Schematics of F_y -band wavefunction at (a) Γ - and (b) X -points	14
1-6	Qualitative temperature-field phase diagrams	19
1-7	Evolution of Weyl nodes as the ratio of B_{2u} to B_{3u} gap amplitudes change in the $B_{3u} + iB_{2u}$ phase.	19
1-8	Example from space group 14	26
1-9	DFT bands of BiS ₂ near the X point	41
1-10	Schematic phase diagram for a spin-singlet superconductor under Zeeman effect.	44
1-11	The position of the bicritical point (T_b, H_b)	45
1-12	DFT Fermi surface of UCoGe.	50
2-1	Error curves of ML models.	57
2-2	Performance of ML models for BBH injections	58
2-3	A diagram of a dark matter particle X with mass M_X decaying into two gravitons in the limit of cone-shaped classical gravitational waves.	60
2-4	Rate of Blip Glitches(Weekly Statistics, ML confidence ≥ 0.99)	61
2-5	Representative blip glitch in O3b Virgo and cleaned q-scan by Gabor-Morlet wavelet	62
A-6	Performance of ML models for BNS injections.	82
A-7	Performance of ML models for NSBH injections.	83

LIST OF TABLES

1.1	All even-parity local gap functions classified by D_{4h} irreps.	6
1.2	Pairing gap functions due to ferromagnetic interactions between rung sublattice degrees of freedom.	16
1.3	Space groups with nodal planes	27
1.4	Classification of kp theories.	31
1.5	Classification of allowed pairing states for the kp theories.	35
1.6	Spin alignment of 8-fold degenerate TRIM.	49
2.1	Classes of the injections	56
2.2	Results of ML models.	57
2.3	List of dark matter parameters	65

LIST OF ABBREVIATIONS

ANN	artificial neural network
BBH	binary black hole
BCS	Bardeen-Cooper-Schrieffer
BFS	Bogoliubov Fermi surface
BNS	binary neutron star
BZ	Brillouin zone
BdG	Bogoliubov-de Gennes
DFT	density functional theory
DMFT	dynamical mean-field theory
DNN	deep neural network
DOF	degree of freedom
DOS	density of states
FFLO	Fulde-Ferrell-Larkin-Ovchinnikov
GGA	generalized gradient approximation
GW	gravitational wave
H	Hanford
GWTC	Gravitational Wave Transient Catalogue
IRREPS	irreducible representations
KNN	k-nearest neighbors
L	Livingston
LDA	local density approximation
LIGO	the laser interferometer gravitational-wave observatory
ML	machine learning
NSBH	neutron star black hole

OAST	orbital-antisymmetric spin-triplet
PE	parameter estimation
ReLU	rectified linear unit
SC	superconductor
SOC	spin-orbit coupling
SVM	support vector machine
TRIM	time-reversal invariant momentum
TRSB	time-reversal symmetry breaking
V	Virgo

ACKNOWLEDGEMENTS

- I would like to express my deepest gratitude to my mentor, Prof. Daniel F. Agterberg, for his continuous support and guidance throughout my Ph.D. journey. He imparted not only profound knowledge but also guided me to cultivate the mindset of a trend-leading researcher. Furthermore, he exemplified how to enjoy life with the dedication to both work and family, a life lesson that I am grateful.
- Equally, I would like to express my deepest gratitude to my mentor, Prof. Jolien D. Creighton, for his continuous support and guidance throughout my Ph.D. journey. Despite my unconventional research path within the LIGO projects, he remained incredibly supportive and consistently encouraged me to try new ideas. I learned from him how to manage and guide people within a large collaboration. Without his support, this dissertation would not have come to completion.
- This work is supported by the US Department of Energy, Office of Basic Energy Sciences, Division of Materials Sciences and Engineering under Award DE-SC0021971 and by a UWM Discovery and Innovation Grant.
- This work is supported by the National Science Foundation under grant PHY-2207728 and PHY-1912649.
- The contents of Chap. 1.2 are published in Ref. [1]:
Han Gyeol Suh, Henri Menke, P. M. R. Brydon, Carsten Timm, Aline Ramires, and Daniel F. Agterberg, *Stabilizing even-parity chiral superconductivity in Sr_2RuO_4* , Phys. Rev. Research **2**, 032023(R). ©2020 American Physical Society.
- The contents of Chap. 1.3 are published in Ref. [2]:
Tatsuya Shishidou, Han Gyeol Suh, P. M. R. Brydon, Michael Weinert, and Daniel F. Agter-

berg, *Topological band and superconductivity in UTe_2* , Phys. Rev. B **103**, 104504. ©2021 American Physical Society.

- The contents of Chap. 1.4 are available on arXiv in Ref. [3] and the preprint is currently under review for publication in Physical Review X:

Han Gyeol Suh, Yue Yu, Tatsuya Shishidou, Michael Weinert, P. M. R. Brydon, Daniel F. Agterberg, *Superconductivity of anomalous pseudospin*, arXiv:2301.11458.

Chapter 1

Superconducting Materials

1.1 Overview

Work and research in superconductors has led to novel fundamental discoveries, including new topologically protected states. Topologically protected states are robust, because they are protected by symmetry. Thus, they are not altered by common changes to their environment. In this chapter, the following sections are reprints of my published works on superconductors.

In Section 1.2, I will discuss the possibility of an even-parity chiral superconducting state in Sr_2RuO_4 . This material has long been thought to host a spin-triplet chiral p -wave superconducting state. However, the singletlike response observed in recent spin-susceptibility measurements casts serious doubts on this pairing state. Together with the evidence for broken time-reversal symmetry and a jump in the shear modulus c_{66} at the superconducting transition temperature, the available experiments point towards an even-parity chiral superconductor with $k_z(k_x \pm ik_y)$ -like E_g symmetry, which has consistently been dismissed based on the quasi-two-dimensional electronic structure of Sr_2RuO_4 . My collaborators and I show that E_g state can be stabilized and is energetically competitive with the A_{1g} state. This E_g state naturally gives rise to Bogoliubov Fermi surfaces (BFSs), which are quasiparticle zero energy surface topologically protected by a broken symmetry. This work is reprinted from Ref. [1], where I mainly contributed to showing the stability of E_g channel by solving linearized gap equation as shown in Fig. 1-1 and numerically finding the Bogoliubov Fermi surfaces as shown in Fig. 1-3.

In Section 1.3, I will discuss the topological band and superconductivity in UTe_2 . UTe_2 is a likely spin-triplet superconductor that also exhibits evidence for chiral Majorana edge states. A characteristic structural feature of UTe_2 is inversion-symmetry related pairs of U atoms, forming rungs of ladders. My collaborators and I show how each rung's two sublattice degrees of freedom play a key role in understanding the electronic structure and the origin of superconductivity. We also show that a previously identified strong ferromagnetic interaction within a U-U rung leads to a pseudospin-triplet superconducting state that accounts for a nonzero polar Kerr angle, the observed magnetic field-temperature phase diagrams, and nodal Weyl fermions. This work is reprinted from Ref. [2], where I mainly contributed to fitting our microscopic model to DFT data and analyzing the behavior of Weyl nodes in our model as shown in Fig. 1-7.

In Section 1.4, I will discuss the superconductivity of anomalous pseudospin. Spin-orbit coupling driven by broken inversion symmetry (I) is known to lead to unusual magnetic response of superconductors, including extremely large critical fields for spin-singlet superconductors. This unusual response is also known to appear in materials that have I , provided there is local I -breaking: fermions participating in superconductivity reside on crystal sites that lack I . Here my collaborators and I show that this unusual response exists even when the crystal sites preserve I . Indeed, we argue that the symmetry of Kramers degenerate fermionic pseudospin is more relevant than the local crystal site symmetry. We examine and classify non-symmorphic materials with momentum space spin-textures that exhibit an anomalous pseudospin with different symmetry properties than usual spin-1/2. We find that this anomalous pseudospin does not depend on the existence of local I breaking crystal sites and it optimizes the unusual magnetic response traditionally associated with locally noncentrosymmetric superconductors, dramatically extending the range of relevant materials. We further show this anomalous pseudospin leads to fully gapped 'nodal' superconductors and provides additional insight into the breakdown of Blount's theorem for pseudospin triplet superconductors. We apply our results to UPt_3 , BiS_2 -based superconductors, Fe-based superconductors, and paramagnetic UCoGe . This work is reprinted from Ref. [3], where I mainly contributed to classifying all possible symmetry based kp theories near TRIM points on these nodal planes in Table 1.4.

1.2 Bogoliubov Fermi Surfaces - Sr_2RuO_4

1.2.1 Introduction

Based on early Knight shift [4], polarized neutron scattering [5], muon-spin-resonance [6], and polar Kerr measurements [7], Sr_2RuO_4 has been widely thought to support a spin-triplet chiral p -wave superconducting state with E_u symmetry [8–24]. This proposed state has had difficulty reconciling other experimental results [24], including the absence of chiral edge currents [25], thermal transport consistent with a nodal state [26–28], apparent Pauli-limiting effects for in-plane fields [29], and the failure to observe a cusplike behavior of the critical temperature under nematic strain [30, 31]. Plausible explanations for each of these inconsistencies have nevertheless been presented [24, 32, 33]. Recently, however, the Knight shift has been revisited [34, 35] and, contrary to earlier results, a relatively large reduction of the Knight shift for in-plane fields in the superconducting state has been observed. This finding cannot be reconciled with the standard spin-triplet chiral p -wave state [9].

Although it now seems unlikely that Sr_2RuO_4 is a spin-triplet chiral p -wave superconductor, the observation of broken time-reversal symmetry [6, 7, 36] and a jump in the shear modulus c_{66} [37, 38] at the critical temperature still indicate a multicomponent order parameter [39]. The only other possible multicomponent channel within D_{4h} symmetry belongs to the E_g irreducible representation (irrep) [39]. At the Fermi surface, a chiral order parameter in this channel resembles a spin-singlet d -wave state, which has horizontal line nodes. Such a state would appear to imply that the dominant pairing instability involves electrons in different RuO_2 layers, which is difficult to understand in view of the pronounced quasi-two-dimensional nature of the normal state of Sr_2RuO_4 . Indeed, no microscopic calculation for Sr_2RuO_4 has found a leading weak-coupling E_g instability [40–42].

In this section, we show that *local* interactions can lead to a weak-coupling instability in the E_g channel, once we consider a complete three-dimensional (3D) model for the normal state. Physically, this E_g state is a local (i.e., s -wave) orbital-antisymmetric spin-triplet (OAST) state stabilized by on-site Hund’s coupling. When the renormalized low-energy Hund’s coupling J becomes larger than the interorbital Hubbard interaction U' , this channel develops an attractive interaction [43–48].

This pairing instability has been found in dynamical mean-field theory, which predicts it appears in the strong-coupling limit even when the unrenormalized high-energy J is less than U' [49], and also in the presence of strong charge fluctuations [50]. Pairing due to this type of interaction was considered for Sr_2RuO_4 in Ref. [43], where an A_{1g} pairing state was found to be stable. Motivated by the relevance of J for the normal state of Sr_2RuO_4 [51], we revisit the local-pairing scenario. We note that, remarkably, a similar OAST pairing state is believed to be responsible for nematic superconductivity in $\text{Cu}_x\text{Bi}_2\text{Se}_3$ [52–54]. In the following, we show that an E_g state can be stabilized over the A_{1g} state of Ref. [43] by including momentum-dependent spin-orbit coupling (SOC) corresponding to interlayer spin-dependent hopping with a hopping integral on the order of 10 meV. This small value leaves the quasi-two-dimensional nature of the band structure intact. Moreover, we use the concept of superconducting fitness [55, 56] to understand the importance of this term in stabilizing the E_g state. Finally, we show that this chiral multiorbital E_g state will display Bogoliubov Fermi surfaces [57, 58], instead of line nodes.

1.2.2 Normal-state Hamiltonian

An accurate description of the normal-state Hamiltonian is crucial for understanding superconductivity in the weak-coupling limit. Our starting point is a tight-binding parametrization of the normal-state Hamiltonian that includes all terms allowed by symmetry [59]. To determine the magnitude of each term, we carry out a fit to the density-functional theory (DFT) results of Veenstra *et al.* [60]. However, angle-resolved photoemission spectroscopy (ARPES) measurements [51, 61] suggest that some DFT parameters differ appreciably from the measured values, in particular the SOC strengths [60]. We therefore allow the SOC parameters to vary in order to understand how they affect the leading superconducting instability, under the constraint that the Fermi surfaces do not differ significantly from the DFT predictions and are hence still qualitatively in accordance with the ARPES results.

The relevant low-energy degrees of freedom (DOF) are the electrons in the t_{2g} -orbital manifold d_{yz} , d_{xz} , and d_{xy} of Ru. Using the spinor operator $\Phi_{\mathbf{k}}^\dagger = (c_{\mathbf{k},yz\uparrow}^\dagger, c_{\mathbf{k},yz\downarrow}^\dagger, c_{\mathbf{k},xz\uparrow}^\dagger, c_{\mathbf{k},xz\downarrow}^\dagger, c_{\mathbf{k},xy\uparrow}^\dagger, c_{\mathbf{k},xy\downarrow}^\dagger)$, where $c_{\mathbf{k},\gamma\sigma}^\dagger$ creates an electron with momentum \mathbf{k} and spin σ in orbital γ , we construct the most

general three-orbital single-particle Hamiltonian as $H_0 = \sum_{\mathbf{k}} \Phi_{\mathbf{k}}^\dagger \hat{H}_0(\mathbf{k}) \Phi_{\mathbf{k}}$ with

$$\hat{H}_0(\mathbf{k}) = \sum_{a=0}^8 \sum_{b=0}^3 h_{ab}(\mathbf{k}) \lambda_a \otimes \sigma_b, \quad (1.1)$$

where the λ_a are Gell-Mann matrices encoding the orbital DOF and the σ_b are Pauli matrices encoding the spin (λ_0 and σ_0 are unit matrices), and $h_{ab}(\mathbf{k})$ are even functions of momentum. Time-reversal and inversion symmetries allow only for 15 $h_{ab}(\mathbf{k})$ functions to be finite. The explicit form of the $h_{ab}(\mathbf{k})$ functions and the Gell-Mann matrices are given in the [1].

1.2.3 Interactions and superconductivity

We consider on-site interactions of the Hubbard-Kanamori type [62],

$$\begin{aligned} H_{\text{int}} = & \frac{U}{2} \sum_{i,\gamma,\sigma \neq \sigma'} n_{i\gamma\sigma} n_{i\gamma\sigma'} + \frac{U'}{2} \sum_{i,\gamma \neq \gamma',\sigma,\sigma'} n_{i\gamma\sigma} n_{i\gamma'\sigma'} \\ & + \frac{J}{2} \sum_{i,\gamma \neq \gamma',\sigma,\sigma'} c_{i\gamma\sigma}^\dagger c_{i\gamma'\sigma'}^\dagger c_{i\gamma\sigma'} c_{i\gamma'\sigma} \\ & + \frac{J'}{2} \sum_{i,\gamma \neq \gamma',\sigma \neq \sigma'} c_{i\gamma\sigma}^\dagger c_{i\gamma\sigma'}^\dagger c_{i\gamma'\sigma'} c_{i\gamma'\sigma}, \end{aligned} \quad (1.2)$$

where $c_{i\gamma\sigma}^\dagger$ ($c_{i\gamma\sigma}$) creates (annihilates) an electron at site i in orbital γ with spin σ , and $n_{i\gamma\sigma} = c_{i\gamma\sigma}^\dagger c_{i\gamma\sigma}$. The first two terms describe repulsion ($U, U' > 0$) between electrons in the same and in different orbitals, respectively. The third and fourth terms represent the Hund's exchange interaction and pair-hopping interactions respectively. We take $J = J'$ [62], where $J > 0$ is expected for Sr_2RuO_4 . In the context of Sr_2RuO_4 , H_{int} is usually taken as the starting point for the calculation of the spin- and charge-fluctuation propagators which enter into the effective interaction [19, 22]. Here, we take a different approach [43, 46] by directly decoupling the interaction in the Cooper channel, which, for $U' - J < 0$, yields an attractive interaction for on-site pairing in an OAST state. This scenario has previously been applied to a two-dimensional model of Sr_2RuO_4 , predicting an OAST A_{1g} state [43]. Although a strong-coupling instability towards an OAST E_g state in the absence of SOC has been predicted in Ref. [50], the superconductivity in Sr_2RuO_4 is likely in the weak-coupling regime [24]. It is therefore important to understand if an OAST E_g state can be the

Table 1.1: All even-parity local gap functions classified by irreps of the point group D_{4h} . Here, $[a, b]$ corresponds to the parametrization of the gap matrix as $\lambda_a \otimes \sigma_b (i\sigma_2)$. The other columns give the orbital and spin character, as well as the interaction g for each superconducting state derived from the Hubbard-Kanamori interaction H_{int} in Eq. (1.2). Note that the two components of the E_g order parameters can stem from the orbital DOF, as for $\{[2, 0], [3, 0]\}$ and $\{[6, 3], -[5, 3]\}$, or from the spin DOF, as for $\{[4, 1], [4, 2]\}$.

Irrep	$[a, b]$	Orbital	Spin	Interaction g
A_{1g}	$[0, 0]$	symmetric	singlet	$U + 2J$
	$[8, 0]$	symmetric	singlet	$U - J$
	$[4, 3]$	antisymmetric	triplet	$U' - J$
	$[5, 2] - [6, 1]$	antisymmetric	triplet	$U' - J$
A_{2g}	$[5, 1] + [6, 2]$	antisymmetric	triplet	$U' - J$
B_{1g}	$[7, 0]$	symmetric	singlet	$U - J$
	$[5, 2] + [6, 1]$	antisymmetric	triplet	$U' - J$
B_{2g}	$[1, 0]$	symmetric	singlet	$U' + J$
	$[5, 1] - [6, 2]$	antisymmetric	triplet	$U' - J$
E_g	$\{[2, 0], [3, 0]\}$	symmetric	singlet	$U' + J$
	$\{[4, 1], [4, 2]\}$	antisymmetric	triplet	$U' - J$
	$\{[6, 3], -[5, 3]\}$	antisymmetric	triplet	$U' - J$

leading instability in this limit.

In the spirit of Ref. [46], we treat H_{int} as a renormalized low-energy effective interaction. We tabulate the allowed local gap functions, their symmetries, and the interactions in the respective pairing channels in Table 1.1. Here, we adopt the common assumption of on-site rotational symmetry, which stipulates $U = U' + 2J$ [62]. This choice implies that all the OAST channels have the same attractive pairing interaction, which highlights the role of the normal-state Hamiltonian in selecting the most stable state. However, since the Ru sites have D_{4h} symmetry and not the assumed full rotational symmetry, the interaction strengths for the different pairing channels are generally different. Our results should therefore be interpreted as providing a guide to which superconducting states this form of attractive interaction can give rise to.

We write a free-energy expansion up to second order in the superconducting order parameter given by the gap matrices $\hat{\Delta}_i = \Delta_i \lambda_{a_i} \otimes \sigma_{b_i} (i\sigma_2)$,

$$\mathcal{F} = \frac{1}{2} \sum_i \frac{1}{g_i} \text{Tr} [\hat{\Delta}_i^\dagger \hat{\Delta}_i] - \frac{k_B T}{2} \sum_{\mathbf{k}, \omega, i, j} \text{Tr} [\hat{\Delta}_i \hat{G} \hat{\Delta}_j^\dagger \hat{G}], \quad (1.3)$$

where i and j sum over all channels of a chosen irrep, g_i are the corresponding interaction strengths from Table 1.1, $\omega_m = (2m+1)\pi k_B T$ are the fermionic Matsubara frequencies, and $\hat{G} = (i\omega_m - \hat{H}_0)^{-1}$

and $\hat{G} = (i\omega_m + \hat{H}_0^T)^{-1}$ are the normal-state Green's functions. Nontrivial solutions of the coupled linearized gap equations obtained from $\partial\mathcal{F}/\partial\Delta_i^* = 0$ give the critical temperature T_c and the linear combination of the $\hat{\Delta}_i$ corresponding to the leading instability. We include all channels in a chosen irrep, not just the attractive ones (see Table 1.1). In evaluating the last term in Eq. (1.3), we keep only intraband contributions; although the inclusion of interband terms will shift T_c , this effect is negligible in the weak-coupling regime.

1.2.4 Results

Weak-coupling OAST pairing states for an attractive Hund's interaction require nonvanishing SOC [46, 47, 56]. SOC appears in five terms in the Hamiltonian $\hat{H}_0(\mathbf{k})$ in Eq. (1.1), representing a large parameter space to explore. We shall focus on the effects of the following terms: the z component of the atomic SOC, $h_{43} = \eta_z$; the in-plane atomic SOC, $h_{52} - h_{61} = \eta_\perp$; and the momentum-dependent SOC associated with the interlayer hopping amplitude t_{56z}^{SOC} between the d_{xy} and the d_{xz} and d_{yz} orbitals, $\{h_{53}, h_{63}\} = 8 t_{56z}^{\text{SOC}} \sin(k_z c/2) \{\cos(k_x a/2) \sin(k_y a/2), -\sin(k_x a/2) \cos(k_y a/2)\}$. Here, we will ignore the anisotropy of the atomic SOC and set $\eta_z = \eta_\perp = \eta$. We have carried out a cursory exploration of the larger SOC parameter space and find that varying the other parameters within reasonable ranges such that the Fermi surfaces do not significantly deviate from the DFT predictions has little effect on the leading instability.

Figure 1-1(a) shows the phase diagram as a function of the atomic SOC η and the momentum-dependent SOC, parametrized by t_{56z}^{SOC} . We find leading instabilities in the A_{1g} and E_g channels. A_{2g} and B_{2g} states are not competitive anywhere in the phase diagram. A B_{1g} state is sometimes found as a subleading instability. The E_g solution is dominated by the $\{[6, 3], -[5, 3]\}$ channel and is stabilized for $t_{56z}^{\text{SOC}} \gtrsim \eta/4$. Under the constraint of realistic Fermi surfaces, the E_g state can be stabilized for t_{56z}^{SOC} as small as about 5 meV, although this requires a rather small value of the on-site SOC. It is remarkable that such a small energy scale determines the relative stability of qualitatively different pairing states. As shown in Fig. 1-1(b), the Fermi surfaces for parameters stabilizing A_{1g} or E_g states are indeed very similar. The SOC strength remains controversial [51, 60, 61], but here we have shown its importance for the determination of the most stable superconducting state. Our

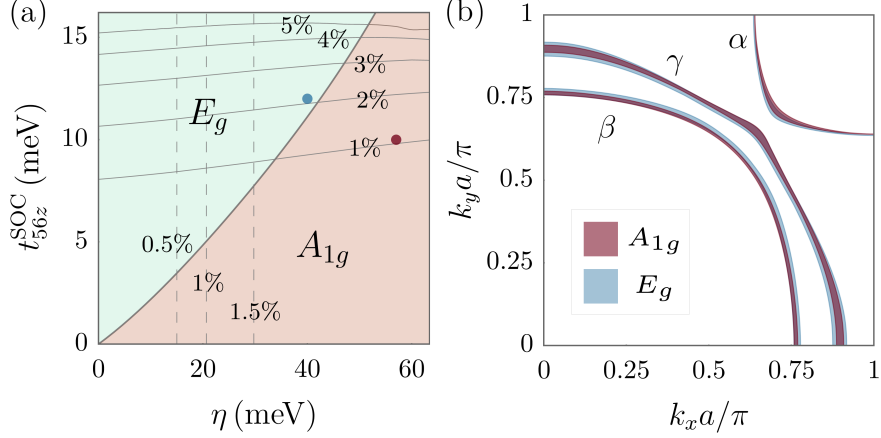


Figure 1-1: (a) Phase diagram showing the stability of A_{1g} and E_g pairing states as a function of the SOC parameters η and t_{56z}^{SOC} . The vertical dashed lines indicate the minimum distance between two Fermi surfaces. Percentages are defined as fractions of $2\pi/a$. For small η , the separation between the β and γ bands becomes too small, in view of the ARPES data [51]. The thin solid lines indicate the maximum variation of the Fermi surface along the k_z direction. For large t_{56z}^{SOC} , the Fermi surfaces become too dispersive. The blue and magenta dots denote the parameter choices for E_g and A_{1g} stable solutions used in (b). (b) Fermi-surface shapes, projected onto the $k_x k_y$ plane, for representative points in the A_{1g} (red) and E_g (blue) regions in (a). For A_{1g} , $\eta = 57$ meV and $t_{56z}^{\text{SOC}} = 10$ meV, while for E_g , $\eta = 40$ meV and $t_{56z}^{\text{SOC}} = 12$ meV.

results are a proof of principle that an E_g superconducting state can be realized in Sr_2RuO_4 , even for purely local interactions, once one properly takes into account a complete and plausible 3D model for the normal state.

Figure 1-2 displays the projected gaps at the Fermi surfaces for representative A_{1g} and E_g states. Note that in both cases the gap magnitude on the α sheet is very small, whereas the gaps on the β and γ sheets are comparable. This shows that we cannot simply identify the γ band [63] or the pair of almost one-dimensional α and β bands [19] as the dominant ones for superconductivity [22].

It is possible to understand why these SOC terms stabilize the respective ground states based on the notion of superconducting fitness [55, 56]. In particular, it has been shown for two-band superconductors that if the quantity $\hat{F}_A(\mathbf{k}) = \tilde{H}_0(\mathbf{k})\hat{\Delta}(\mathbf{k}) + \hat{\Delta}(\mathbf{k})\tilde{H}_0^*(-\mathbf{k})$ is zero there is no intraband pairing and hence no weak-coupling instability [here, $\tilde{H}_0(\mathbf{k})$ corresponds to $\hat{H}_0(\mathbf{k})$ with $h_{00}(\mathbf{k})$ set to zero]. Hence, adding terms to the normal-state Hamiltonian such that $\hat{F}_A(\mathbf{k})$ becomes nonzero for a particular gap function turns on a weak-coupling instability in this channel. The fitness analysis can be extended to our three-orbital model or, alternatively, we can construct an

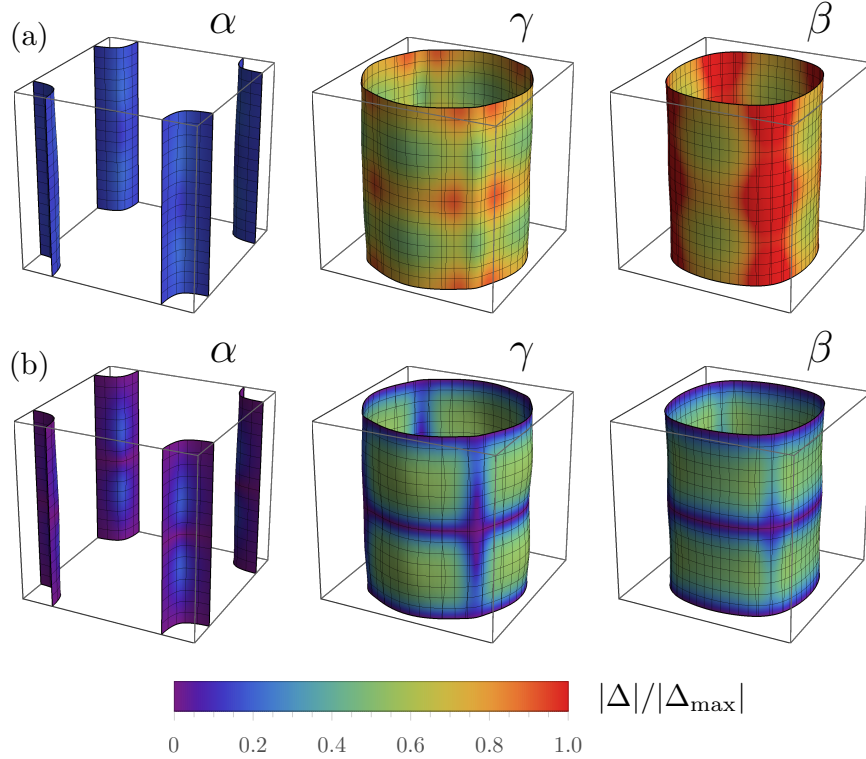


Figure 1-2: Projected gaps at the Fermi surfaces for a representative (a) A_{1g} and (b) chiral E_g state in the first Brillouin zone. Parameters are the same as in Fig. 1-1 (b). The color code is normalized to the maximum value of the A_{1g} gap.

effective two-orbital model valid sufficiently far from the Brillouin-zone diagonals. Applying the fitness argument to the effective two-band model, we find that the on-site SOC η turns on both the A_{1g} and B_{1g} pairing channels, whereas the parameter t_{56z}^{SOC} turns on the E_g $\{[6, 3], -[5, 3]\}$ channel, consistent with what we find numerically.

In view of the Knight-shift experiments [34, 35], it is important to comment on the spin susceptibility associated with the dominant E_g $\{[6, 3], -[5, 3]\}$ channel. Since it is a spin-triplet state with in-plane spin polarization of the Copper pairs, similar to the familiar chiral p -wave spin-triplet pairing with a \mathbf{d} -vector along the k_z direction, it might naively be expected to show a temperature-independent spin susceptibility for in-plane fields. This is not the case, however, since the even parity of E_g implies that the intraband pairing potential is a pseudo-spin singlet when expressed in the band basis and the low-energy response to a magnetic field is identical to a true spin singlet. This has been examined numerically for similar pairing states [48, 64], where it was found that

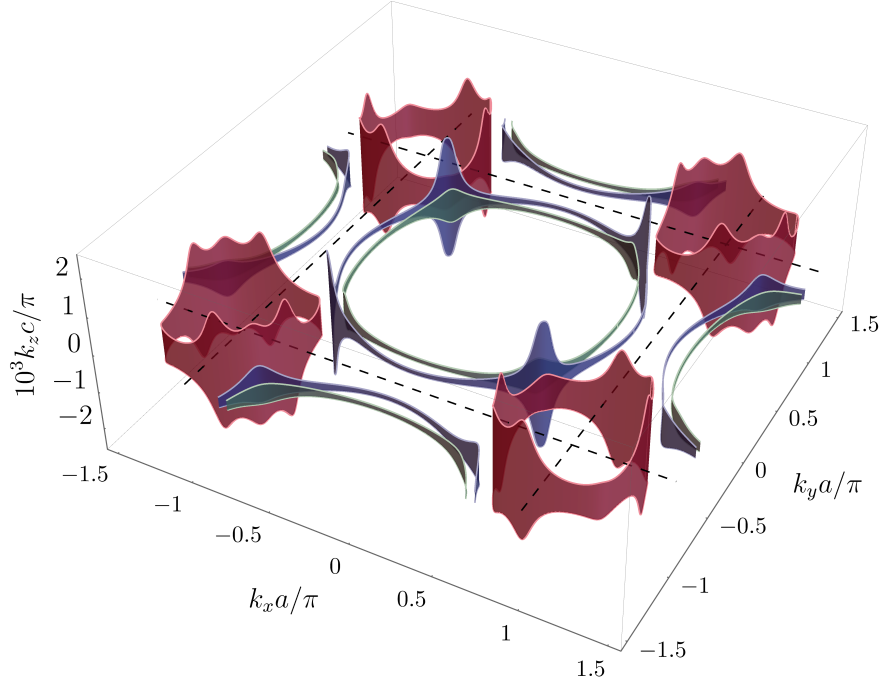


Figure 1-3: BFSs for the chiral E_g state. The Fermi surfaces in red, green, and blue correspond to inflated nodes stemming from the α , β , and γ band, respectively.

only a small fraction of the normal-state spin susceptibility persists at zero temperature in the superconducting state.

1.2.5 Bogoliubov Fermi surfaces

An E_g state is expected to have horizontal line nodes at $k_z = 0$ and $2\pi/c$ [24, 39], and it will have vertical line nodes in a time-reversal invariant nematic state [37, 39]. Although recent tunneling measurements have called into question time-reversal symmetry breaking in Sr_2RuO_4 [65], here we follow the indications of polar Kerr and μSR experiments [6, 7, 36], and explicitly consider a chiral E_g state which has no vertical line nodes. It has recently been shown that for an even-parity superconductor that spontaneously breaks time-reversal symmetry, the excitation spectrum is either fully gapped or contains Bogoliubov Fermi surfaces (BFSs) [57, 58]. Indeed, the chiral E_g state considered here has BFSs, which are shown in Fig. 1-3. These BFSs are very thin in the direction perpendicular to the normal-state Fermi surface, giving them a ribbon-like appearance that extends along the k_z axis by about 0.2% of the Brillouin zone. This value is proportional to the

gap amplitude, here set to 0.15 meV. While the total residual density of states from the BFSs is not large and may be difficult to observe [66], such a nodal structure implies that some experimental results require reinterpretation. In particular, given that the BFSs extend along the k_z -axis, the argument that thermal conductivity measurements rule out the E_g state because it has horizontal line nodes [27] no longer applies. The presence of BFSs may also require a reinterpretation of quasi-particle-interference experiments [67]. We leave a detailed study of experimental consequences of the E_g OAST state for future work.

1.2.6 Conclusions

We have argued that an E_g order parameter can be a realistic weak-coupling ground state for Sr_2RuO_4 , once we consider a complete 3D model for the normal state and interactions of the Hubbard-Kanamori type. Key to our construction are the usually neglected momentum-dependent SOC terms in the normal state. These terms can completely change the nature of the superconducting ground state, despite being so small that they do not significantly change the Fermi surfaces. Our theory reconciles the recent observation of a singlet-like spin susceptibility with measurements indicating a two-component order parameter and broken time-reversal symmetry.

1.3 Weyl point nodes - UTe_2

1.3.1 Introduction

UTe_2 [68] is poised to become a paradigmatic superconductor. There is strong evidence that it is unconventional. Superconductivity survives to much higher magnetic fields than expected [68] and shows a highly unusual re-entrant field induced superconductivity [69]. Furthermore, there is also evidence for multiple superconducting phases [70–72], spontaneous broken time-reversal symmetry [71], and chiral Majorana edge and surface states [73, 74], the nature of which are not yet understood.

Many important questions remain open in understanding this superconducting state. Key amongst these is the origin of the odd-parity superconductivity. On the related materials UGe_2 ,

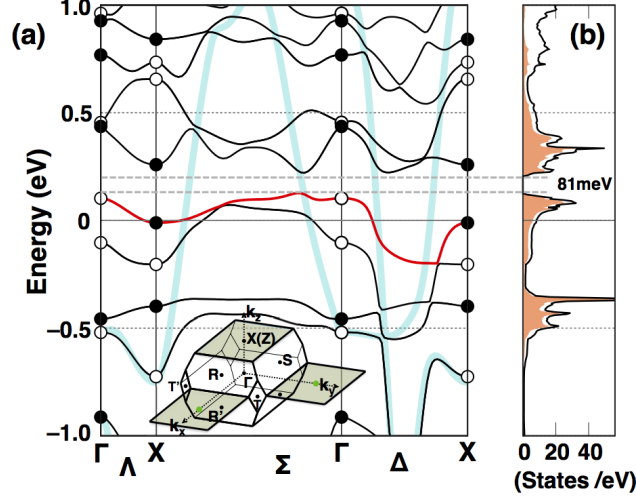


Figure 1-4: (a) LDA+ U band dispersion along k_z axis (Λ line), k_x (Σ) and k_y (Δ) with $U = 1.2$ eV. Topological band with parity inversion (even at Γ and odd at X) is highlighted by red line. A few bands selected from ThTe₂ calculation are overlaid by thick blurred lines (with upward energy shift of 0.4 eV to account for the atomic number difference of Th and U), which provide a good idea of how the coherent bands and Fermi surface would be when all U 5f electrons are localized. (b) Density of states. Shaded (orange) area shows U 5f $j = 5/2$ components.

URhGe, and UCoGe there is a consensus that ferromagnetic fluctuations is the origin [75]. However, there is a debate as to the nature of these ferromagnetic fluctuations [75]. This debate is related to the uncertainty of the underlying electronic model in this class of materials. Recently, this has been addressed in UTe₂ [76–78]. Here LDA+ U and DMFT have developed a family of bandstructures that depend upon U . The consequences of this family of bandstructures on superconductivity have been explored, suggesting topological superconductivity [78]. In addition, effective Heisenberg theories have been developed, with the insight that the strongest magnetic interaction, for all U used, is a ferromagnetic interaction between the two inequivalent U atoms on a ladder rung [77], providing a potential mechanism for superconductivity.

Here we revisit the LDA+ U calculations, finding good agreement with previous results and newly identifying a topological band that appears near the chemical potential for all values of U . This topological band has its origin in 5f electrons located predominantly on the rung sublattice degrees of freedom. On the two U atoms of the rung, even parity and odd-parity orbital combinations can be made, a band inversion between such odd and even parity combinations provides the origin of the topological band. The appearance of the topological band together with the rung fer-

romagnetic interaction discussed above indicates that the rung sublattice degrees of freedom play a central role in the electronic description. Consequently, we construct a symmetry-based electronic model that explicitly includes these rung sublattice degrees of freedom and the ferromagnetic interaction between them. This model: yields magnetic field-temperature phase diagrams that agree with experiment; and allows a superconducting state with Weyl nodes, providing a potential explanation for the observed surface chiral edge states [74], the observed polar Kerr effect [71], and observed low energy excitations in the superconducting state [79].

1.3.2 Topological Band

A likely scenario for the electronic structure of UTe₂ is a low temperature renormalized Fermi liquid ground state in which Uranium 5f electrons are participants. This is consistent with scanning tunneling microscopy [74] and the observed Fermi pocket about the Z -point seen in ARPES data [80]. This point of view has been adopted in recent DMFT and GGA+ U calculations [76–78]. The latter reveal that the band structure depends strongly on the choice of U , suggesting that any theory of the superconducting state needs to be developed for a range of band structures, emphasizing properties that are generic across the relevant possibilities. Here, we have carried out DFT calculations of the bandstructure of UTe₂ using the full-potential linearized augmented plane wave method and including a Coulomb U to account for interactions of the Uranium 5f electrons. Our results agree with those found earlier [77, 78]. A key new finding is that for all values of U included here, we find a topological band at or near the chemical potential.

A typical band structure with a moderate U value ($U = 1.2$ eV) is shown in Fig. 1-4. Due to the large U 5f spin-orbit interaction, the energy range shown reveals only $j = 5/2$ electronic states. This $j = 5/2$ manifold splits into three groups: (1) a lowest energy set of two bands which are less dispersive with large spectral weight centering around 0.5 eV; (2) a middle group of bands that are responsible for the Fermi surface; and (3) a highest energy set of two bands. Between groups (2) and (3) there is a band gap and we have calculated the Z_2 topological index for bands below this band gap. This Z_2 index is calculated from the band parity at the eight time-reversal-invariant momenta (TRIMs). Only two of the TRIMs (Γ and X) can give rise to a non-trivial Z_2 invariant,

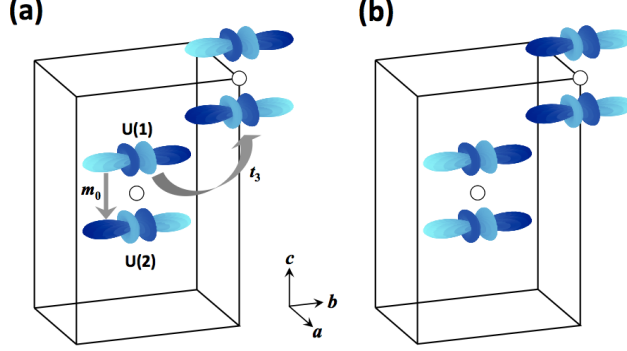


Figure 1-5: Schematics of F_y -band wavefunction at (a) Γ - and (b) X -points. A conventional orthorhombic cell and two lattice points (open circles), $(1/2, 1/2, 1/2)$ and $(1, 1, 1)$, are drawn. Each lattice point is a spatial-inversion center and comes with a ladder rung of the shortest distance U(1)-U(2). The wavefunction sign is represented by colors (dark and light). Two-types of U(1)-U(2) hopping are shown: m_0 is along c axis within a rung (Π hybridization) and t_3 connects U(1) and U(2) of different lattice points. Note that Bloch phase at these two lattice points is in-phase at Γ and out-of-phase at X .

since the other six TRIMs have a mirror symmetry parity duplication. In Fig. 1-4, these parities are given by black (odd-parity) and white (even-parity) dots. The non-trivial Z_2 index is a consequence of the top band (highlighted in red in Fig 1) for which there is a parity inversion in going from Γ to X . The topological band is made up mainly from $5f y(5y^2 - 3r^2)$ orbitals on the two rung U atoms, as shown in Fig. 1-5. For the U used here, this topological band gives rise to a Fermi surface that is centered on Z point when viewed from the \hat{b} direction, in agreement with the Fermi pocket observed experimentally [80, 81].

1.3.3 Minimal Hamiltonian

The topological band and the ferromagnetic rung interaction found by DFT indicates that the two U rung sublattice degrees of freedom play an important role in the underlying physics. Surprisingly, this degree of freedom has not been explicitly considered in understanding the superconducting state in UTe_2 . In addition, the related materials UGe_2 , $URhGe$, and $UCoGe$ also have similar U atom sublattice degrees of freedom that have not been explicitly included in microscopic models [75]. Here we consider the role of these rung degrees of freedom through the construction of a minimal model that includes these. In particular, The U atoms sit on sites of C_{2v} symmetry, for which only a single spinor symmetry representation exists. A minimal model therefore includes

a single spinor pair centered on each of the two rung sublattice degrees of freedom. While these spinors share the same symmetry properties as usual spin-1/2 fermions under C_{2v} symmetry, DFT reveals they are generally a linear combination of $j = 5/2$ states. We consider the most general symmetry allowed non-interacting description that includes these rung sublattice and spin degrees of freedom. The general form of a theory containing these electronic degrees of freedom is

$$\begin{aligned}
H_N = & \quad \epsilon_0(k) - \mu + f_{Ag}(k)\tau_x + f_z(k)\tau_y + f_y(k)\sigma_x\tau_z \\
& + f_x(k)\sigma_y\tau_z + f_{Au}(k)\sigma_z\tau_z
\end{aligned} \tag{1.4}$$

where the functions $f_i(k)$ carry the symmetry properties given by the label i , in particular $f_{Ag}(k) \approx \text{const}$, $f_z(k) \approx k_z$, $f_y(k) \approx k_y$, $f_x(k) \approx k_x$, and $f_{Au}(k) \approx k_x k_y k_z$. Here the Pauli matrices σ_i describe the spin degrees of freedom and the Pauli matrices τ_i describe the rung degrees of freedom. While our analysis below does not depend upon the detailed form of $f_i(k)$, we nevertheless show specific results the Fermi surface due to the F_y orbitals discussed above. For these orbitals, we take the following tight-binding theory

$$\begin{aligned}
\epsilon_0(k) &= t_1 \cos(k_x) + t_2 \cos(k_y) \\
f_{Ag}(k) &= m_0 + t_3 \cos(k_x/2) \cos(k_y/2) \cos(k_z/2) \\
f_z(k) &= t_z \sin(k_z/2) \cos(k_x/2) \cos(k_y/2) \\
f_y(k) &= t_y \sin(k_y) \\
f_x(k) &= t_x \sin(k_x) \\
f_{Au}(k) &= t_u \sin(k_x/2) \sin(k_y/2) \sin(k_z/2)
\end{aligned} \tag{1.5}$$

Note that to have a topological band requires f_{Ag} to have opposite sign at Γ and at $Z = (0, 0, 2\pi)$, this will occur if $|t_3| > |m_0|$ and both parameters have the same sign. Specifically, we use $(\mu, t_1, t_2, m_0, t_3, t_z, t_x, t_y, t_u) = (0.129, -0.0892, 0.0678, -0.062, 0.0742, -0.0742, 0.006, 0.008, 0.01)$ which were found by fitting to the DFT band near the Fermi surface. For a simple tight binding model based on the F_y orbitals shown in Fig. 1-5, we find that $t_3 = -t_z$ and that the momentum

Table 1.2: Pairing gap functions due to ferromagnetic interactions between rung sublattice degrees of freedom. The first column gives the local gap function and the last column gives the corresponding $\vec{d}(k)$ in the band basis when the spin-orbit coupling terms are vanishing ($f_x = f_y = f_{Au} = 0$).

Gap	Irrep	Interaction	Momentum dependence
$\Delta_z \tau_y \sigma_z$	A_u	$J_x + J_y - J_z$	$\frac{f_z(k)}{\sqrt{f_{Ag}^2(k) + f_z^2(k)}} \hat{z}$
$\Delta_x \tau_y \sigma_x$	B_{2u}	$-J_x + J_y + J_z$	$\frac{f_x(k)}{\sqrt{f_{Ag}^2(k) + f_x^2(k)}} \hat{x}$
$\Delta_y \tau_y \sigma_y$	B_{3u}	$J_x - J_y + J_z$	$\frac{f_y(k)}{\sqrt{f_{Ag}^2(k) + f_y^2(k)}} \hat{y}$

dependent spin-orbit coupling terms t_x, t_y, t_{cu} are longer-range hopping parameters, so we take them to be small.

1.3.4 Magnetic interactions

DFT calculations have found that the dominant magnetic interaction is a ferromagnetic interaction between the rung sublattice U atoms [77]. Note that this local ferromagnetic interaction does not imply a global ferromagnetic state, but only that these two U atoms have the same spin-orientation. Indeed, DFT finds ferromagnetic and anti-ferromagnetic ground states consistent with this local configuration [77]. These different global ground states may account for two magnetically ordered states observed experimentally [72]. This interaction is given by

$$H_{\text{int}} = - \sum_i \{ J_x S_{i,1}^x S_{i,2}^x + J_y S_{i,1}^y S_{i,2}^y + J_z S_{i,1}^z S_{i,2}^z \} \quad (1.6)$$

where 1,2 label the two U atoms on the rung, i labels a lattice site, and in general, due to the orthorhombic structure, the ferromagnetic interactions $J_i > 0$ are unequal. Treating this as an effective coupling for superconductivity, we find this gives rise to three possible pairing states as shown in Table 1.2. Due to the inter-rung sublattice nature of the magnetic interactions, the pairing states are necessarily proportional to a non-trivial τ_y rung operator and take the form $\Delta_i \tau_y \sigma_i$ which describes a local, intra-unit cell, spin-triplet pairing function. While the interactions reveal the role of magnetic anisotropy on pairing interaction, we will now set $J_x = J_y = J_z$ to examine the effect of H_N on these pairing states.

1.3.5 Role of H_N

Naively, the stable pairing state is determined by the largest interaction parameter listed in Table 1. However, this is not the case, H_N alters the relative stability of the pairing states. It is possible to quantify the role of the individual terms of H_N on the transition temperatures T_{c_i} without specifying fully the functions $f_i(k)$ [82, 83]. In particular, this is determined by superconducting fitness, which is specified by commutation and anticommutation relations between the gap functions $\Delta_i\tau_y\sigma_i$ and the terms of the form $\sigma_i\tau_j$ in H_N . If a particular term anticommutes with $\Delta_i\tau_y\sigma_i$, then $T_{c,i}$ is enhanced by this term, if it commutes with $\Delta_i\tau_y\sigma_i$, then $T_{c,i}$ is this term suppressed by this term [83]. This yields the result that the f_{Ag} term suppresses all the $T_{c,i}$ and the $f_z(k)$ term enhances all the $T_{c,i}$. Consequently, if $J_x = J_y = J_z$, the spin-orbit coupling terms will dictate which $T_{c,i}$ is highest. In particular, the largest $T_{c,i}$ is given by the smallest of $\langle f_{Au}^2 \rangle$ (A_u stable), $\langle f_x^2 \rangle$ (B_{3u} stable), or $\langle f_y^2 \rangle$ (B_{2u} stable) where $\langle f \rangle$ represents an average over the Fermi surface. The terms in the tight binding expression will be altered by pressure, providing a potential explanation for the appearance of different superconducting states.

H_N also dictates the form of the pseudospin triplet \vec{d} -vector on the Fermi surface. We do not give the details here but point out that generically, all three pseudospin components $\hat{x}, \hat{y}, \hat{z}$ appear for each gap function. In the limit that the momentum dependent spin-orbit coupling terms can be ignored, $f_x = f_y = f_{Au} = 0$, then the spin-triplet \vec{d} vectors are given as in Table 1.2. Note that it is likely that $f_z^2 \gg f_x^2, f_y^2, f_{Au}^2$ when averaged over the Fermi surface since f_z is determined by a nearest neighbor hopping and f_x, f_y, f_{Au} by a third nearest neighbor hopping. In this case Table 1.2 provides an approximately correct description of \vec{d} , except near $k_z = 0, 2\pi$, in the following this is called the weak spin orbit coupling limit.

1.3.6 Experimental Constraints

At ambient pressure, two superconducting transitions have been observed in zero field [71]. The response of this phase diagram to a field along the \hat{b} (\hat{y}) and \hat{a} (\hat{x}) directions place constraints on the order parameters. In particular, a reasonable interpretation of the experimental data is than an applied field along the \hat{b} direction suppresses the upper transition strongly and suppressed the

lower transition weakly [78, 84]. These data suggest that, in zero field, the upper transition has a \vec{d} predominantly along the \hat{y} and the lower transition has a \vec{d} predominantly along the \hat{x} direction. This naturally occurs within our theory in the weak spin-orbit coupling limit by attributing the upper transition to B_{3u} symmetry and the lower transition to B_{2u} symmetry. This symmetry assignment also naturally accounts for the evolution of the field-temperature phase diagram under pressure. In particular, it has been observed that under pressure, the lower and upper transitions switch [72] at a pressure $P \approx 0.2$ GPa. Consequently, in the high pressure regime, a field along \hat{a} should play a similar role to the field along \hat{b} in the low pressure regime. This has been observed [85, 86]. Our symmetry assignment also agrees with the observation of a polar Kerr effect at low temperatures at ambient pressure, which dictates a low temperature $B_{3u} + iB_{2u}$ (or $A_u + iB_{1u}$) pairing state [71]. Based on our theory in the weak spin-orbit coupling limit, a qualitative phase diagram consistent with these results is shown in Fig. 1-6.

We also note that the weak spin-orbit coupling limit naturally explains why thermal conductivity exhibits nodal behavior that is similar along both the \hat{a} and \hat{b} directions [79]. When $f_x = f_y = f_{Au} = 0$, all the gap functions have accidental line nodes when $k_z = 0$, yielding nodal thermal conductivity behavior along both \hat{a} and \hat{b} . These accidental line nodes will be lifted when the spin-orbit coupling terms are non-zero but small, but a local gap minimum is still expected near $k_z = 0, 2\pi$ which can mimic nodes in thermal conductivity.

1.3.7 Weyl Nodes

A $B_{3u} + iB_{2u}$ pairing state can be stabilized through the coupling to ferromagnetic fluctuations [71]. Here we examine more carefully the nodal structure of a $B_{3u} + iB_{2u}$ pairing state. Using the tight-binding theory given above, we find that Weyl nodes generically exist. These nodes are topologically protected but do not sit at positions of high symmetry. The position of these nodes are determined by the relative amplitudes of the B_{2u} and the B_{3u} order parameters. The evolution of these nodes is shown in Fig. 1-7. We have also computed the Weyl charge of these nodes. Generically, there exists four Weyl nodes, two of charge +1 and two of charge -1. These Weyl nodes imply the existence of surface Fermi arc states which provide an explanation for the chiral

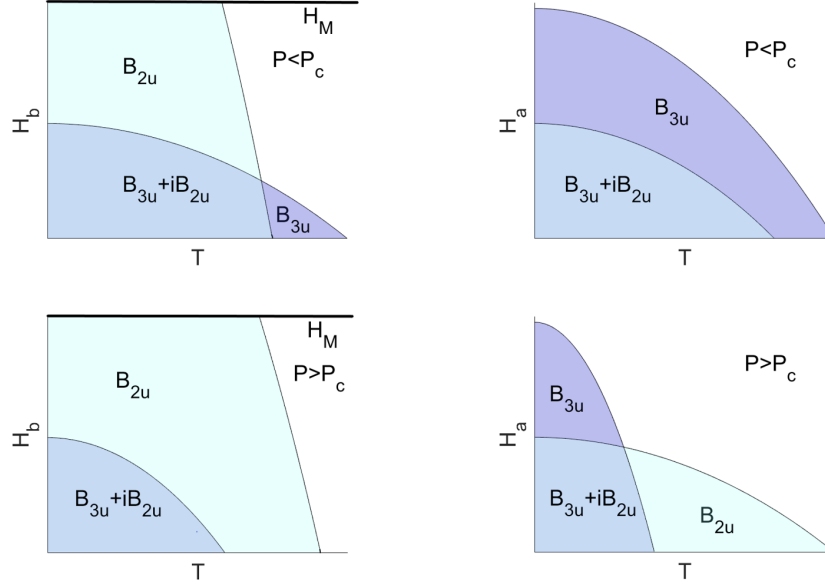


Figure 1-6: Qualitative temperature-field phase diagrams. The top two phase diagrams correspond to $P < 0.2$ GPa and the bottom two to $P > 0.2$ GPa.

edges states seen with scanning tunneling microscopy [74].

1.3.8 Polar Kerr Effect

Now we turn to polar Kerr effect. Our theory generically gives rise to an imaginary anomalous Hall conductivity, which is expected to be proportional to the polar Kerr signal. By a sum rule, we have that the integrated imaginary anomalous Hall conductivity is given by $\int_{-\infty}^{\infty} \omega \sigma_H(\omega) d\omega =$

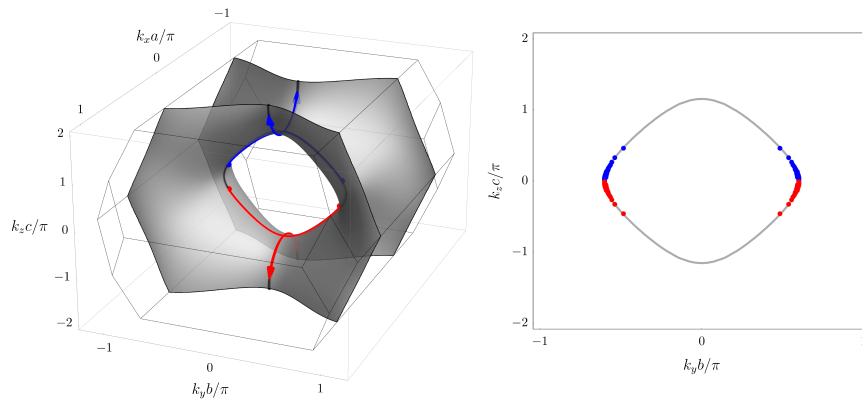


Figure 1-7: Evolution of Weyl nodes as the ratio of B_{2u} to B_{3u} gap amplitudes change in the $B_{3u} + iB_{2u}$ phase.

$-i\pi e^2 \langle [\partial_{k_x} H_N, \partial_{k_y} H_N] \rangle$. The full expansion of the commutator is very complicated and will be analyzed elsewhere, but we note that the contribution $(\partial_{k_x} f_y \partial_{k_y} f_x - \partial_{k_x} f_x \partial_{k_y} f_y) \sigma_z \tau_0$ is directly proportional to the so-called time-reversal-odd bilinear of the $B_{2u} + iB_{2u}$ pairing state [87, 88]. This implies that expectation value of the commutator is nonzero, ensuring the existence of the anomalous Hall conductivity and hence the polar Kerr signal. The sublattice structure of the normal-state Hamiltonian is critical to this argument; in a single-band model, the commutator is vanishing (Taylor and Kallin).

We have found the DFT results yield a topological band near the chemical potential in UTe_2 . This together with a second DFT prediction as to the origin of magnetism suggest that U atom rung degrees of freedom play an important role in UTe_2 . Based on this, we have developed a model that can capture topological bands, $B_{2u} + iB_{3u}$ pairing states that exhibit Weyl point that originate from these rung ferromagnetic interactions, and yield a polar Kerr effect, providing a simple promising model with which to gain an understand of UTe_2 in more detail. In addition, we note that in all U-based ferromagnetic superconductors, there exist U site degrees of freedom that are related by parity symmetry, just as the rung degrees of freedom considered here. These degrees of freedom are typically not included in theories of these superconductors. Our work suggests that these U site degrees of freedom can provide a unifying theme for this class of materials.

1.4 Anomalous Pseudospin

1.4.1 Introduction

Momentum space spin-textures of electronic bands are known to underlie spintronic and superconducting properties of quantum materials [89–91]. In the spintronics context, Rashba-like spin textures allow control of electronic spin through applied electric fields [89, 91]. In superconductors, these same spin textures lead to unusual and counter-intuitive magnetic response, such as the robustness of spin-singlet superconductivity to applied magnetic fields, pair density wave states, and singlet-triplet mixing [90]. While such spin-textures are common when inversion symmetry (I) is broken, it has been realized that these can also occur when I is present. This has lead

to the notion of hidden spin-textures [92] and locally non-centrosymmetric superconductivity [93], where I related sectors each allow a Rashba-like spin-texture due to the local I breaking. These spin-textures are of opposite sign on the two sectors, so that global inversion symmetry is restored. These hidden spin-textures allow the novel physics associated with spin-orbit coupling (SOC) to emerge even when I is not broken. It further allows for new physics to emerge. One notable example is a field induced transition from an even-parity (pseudospin singlet) to odd-parity (pseudospin triplet) observed in CeRh_2As_2 [94–97].

In materials with inversion symmetry, we call the above mentioned strongly anisotropic Pauli limiting fields (and related anisotropic spin susceptibilities), fields far exceeding the usual Pauli limiting field, and field induced transitions between different superconducting states, unusual magnetic response. Key to observing this unusual magnetic response associated with the spin-textures in inversion symmetric materials, is that the I related sectors are weakly coupled [93, 97–99]. Theoretical proposals for how to achieve this fall under two approaches: the first is to tailor weak coupling between the inversion related sectors, for example by separating two inversion symmetry related layers so that the interlayer coupling is weak [94]; the second is to exploit symmetries that ensure that this inter-sector coupling vanishes. The symmetry based approach has been applied to points and lines in momentum space. Examples include two-dimensional (2D) transition metal dichalcogenides near the K-point [100] and non-symmorphic symmetries near the $X - M$ line in BaNiS_2 with space group 129 (P4/nmm) [98]. Recently, we have generalized this to planes in momentum space through an analysis of the locally non-centrosymmetric superconductor CeRh_2As_2 [97]. In all these cases, the only energy splitting between the inversion-related sectors is due to SOC - a situation conceptually similar to materials with broken I , where the usual two-fold pseudospin degeneracy is broken solely by SOC. Indeed, this suggests another route toward tailoring unusual magnetic response of superconductors with inversion symmetry: Instead of emphasizing the local I breaking, as has been done in the examples described above, it may be fruitful to identify electronic degeneracies that are broken solely by SOC. This is the approach we take here and we find it naturally leads to the desired unusual magnetic response. Furthermore, we find it does not require crystal site symmetries with local I breaking, but rather is dictated by the symmetry of

the Bloch fermion pseudospin. As pointed out by Anderson in 1984, [101], fermion pseudospin, derived from the two-fold Kramer’s degeneracy originating from TI symmetry (where T is time-reversal symmetry), plays a fundamental role in superconductivity. Here we find that when the band degeneracy is lifted solely by SOC, this pseudospin has different symmetry properties than usual spin-1/2 pseudospin.

Specifically, we identify electronic band degeneracies that are split *solely* by SOC in materials with both inversion, I and time-reversal T , symmetries. This requires bands that are at least four-fold degenerate when SOC is ignored. Such band degeneracies are not generic and require symmetries beyond the usual two-fold pseudospin (or Kramers) degeneracy that arises from TI symmetry. As discussed in a variety of contexts [102–105], such degeneracies can arise in non-symmorphic crystal structures. Here we focus on the largest momentum region in the 3D Brillouin zone that allows such degeneracies. This occurs on 2D momentum planes, which are often called nodal planes. More specifically, this is the largest region in momentum space for which the required four-fold electronic degeneracies can appear when SOC is ignored. Here we provide a complete list of space groups for which this occurs and provide symmetry based kp theories for all time-reversal-invariant momenta (TRIM) on these nodal planes. As discussed later, many relevant superconductors exhibit Fermi surfaces near these TRIM. We find that the SOC-split electronic states on these nodal planes generically exhibit a pseudospin that has a different symmetry than that of usual spin-1/2 fermions (this generalizes a result we found for space group $P4/nmm$ in the context of locally non-centrosymmetric superconductor $CeRh_2As_2$ [97]). Here we name this anomalous pseudospin and examine the consequences of this anomalous pseudospin on superconductivity. We find that this anomalous pseudospin plays a central role on the superconducting magnetic response and on the properties of spin-triplet superconductivity. Our results provide further insight on earlier nodal and topological classifications of superconductivity in non-symmorphic materials [106–115]. Furthermore, all the non-symmorphic crystal structures we examine have Wyckoff positions with site symmetries that contain inversion symmetry. So, although unusual magnetic response is typically associated with locally noncentrosymmetric superconductors, our theory establishes that the local I breaking is not an essential ingredient, and our classification may guide the experimental

search for new materials where local I breaking is not a feature.

In this section we begin by defining anomalous pseudospin on nodal momenta planes, we then characterize all possible symmetry based kp theories near TRIM points on these nodal planes. Using these kp theories, we analyze the magnetic response and nodal excitations of superconducting states formed from anomalous pseudospin. We apply this analysis to a series of materials that exhibit Fermi surfaces that lie on or near these nodal planes. More specifically we reveal how anomalous pseudospin: explains critical fields that far exceed the Pauli field in BiS₂-based materials [116] and the observed magnetic response 3D Fe-based superconductors [117]; identifies which space groups and TRIM are ideal to find a field induced even parity to odd parity transition akin to that observed in CeRh₂As₂ [95]; provides insight into the gap symmetry of UPt₃ [118]; and shines new light on re-entrant superconductivity in UCoGe [75].

1.4.2 Anomalous pseudospin: symmetry origin

Our aim is to exploit symmetry to find nodal plane band degeneracies that are lifted solely by SOC. As discussed below, once these band degeneracies are lifted, a two-fold pseudospin degeneracy will remain. We find that generically, the pseudospin that results from this procedure does not share the same symmetry properties as usual spin 1/2 and hence we name this anomalous pseudospin.

Pseudospin describes the two-fold Kramers degeneracy that arises at each momentum point \mathbf{k} when the product of time-reversal T and inversion I symmetries, TI , is present. The product TI is anti-unitary and for fermions satisfies $(TI)^2 = -1$, ensuring at least a two-fold degeneracy. It is often the case that this pseudospin behaves as spin-1/2 under rotations [119]. However, when symmetries beyond TI are present, it is possible that this is not the case. One example of this is the angular momentum $j_z = \pm 3/2$ electronic states that arise when cubic symmetry or a three-fold rotation axis is present [90, 120, 121]. In the latter case, this gives rise to so-called type-II Ising superconductivity in 2D materials [121, 122] where large in-plane critical fields appear when the Fermi surface is sufficiently close to momentum points with this three-fold rotation symmetry. A systematic analysis of the appearance of anomalous pseudospin for fermions near the Γ point has been carried out [123–125]. In our case, the anomalous pseudospin appears on momentum

planes in the Brillouin zone, allowing a larger phase space for the physical properties of anomalous pseudospin to manifest.

To ensure the requisite band degeneracy on a nodal plane, consider the symmetry elements that keep a momentum point on the plane invariant (here taken to be normal to the $\hat{\mathbf{n}}$ axis). These are $\{E, \tilde{M}_{\hat{\mathbf{n}}}, TI, T\tilde{C}_{2,\hat{\mathbf{n}}}\}$, where $\tilde{M}_{\hat{\mathbf{n}}}$ is a translation mirror symmetry and $\tilde{C}_{2,\hat{\mathbf{n}}}$ is a translation two-fold rotation symmetry. Their point group rotation and translation component can be denoted using Seitz notation, for example $\tilde{M}_{\hat{\mathbf{n}}} = \{M_{\hat{\mathbf{n}}}|t_1, t_2, t_3\}$ where $M_{\hat{\mathbf{n}}}$ is a point group mirror symmetry along $\hat{\mathbf{n}}$ and (t_1, t_2, t_3) is a fractional translation vector (here the t_3 is the translation component parallel to $\hat{\mathbf{n}}$). Since we are searching for a degeneracy that appears without SOC, we consider orbital or sublattice degrees of freedom for which $(TI)^2 = 1$. The only remaining symmetry that can enforce a two-fold degeneracy is $T\tilde{C}_{2,\hat{\mathbf{n}}}$, since this is anti-unitary, it must satisfy $(T\tilde{C}_{2,\hat{\mathbf{n}}})^2 = -1$ to do so. Since T commutes with rotations, this implies $\tilde{C}_{2,\hat{\mathbf{n}}}^2 = -1$. When operating on orbital or sublattice degrees of freedom, $\tilde{C}_{2,\hat{\mathbf{n}}}^2$ is typically 1, suggesting it is not possible to have the required degeneracy. However, in non-symmorphic groups, $\tilde{C}_{2,\hat{\mathbf{n}}}$ can be a screw axis, for which it is possible to satisfy $\tilde{C}_{2,\hat{\mathbf{n}}}^2 = -1$. In particular, using Seitz notation $\tilde{C}_{2,\hat{\mathbf{n}}} = \{C_{2\hat{\mathbf{n}}}|t_1, t_2, 1/2\}$ (here t_1 and t_2 correspond to either a half in-plane translation vector or to no translation) we have $(\tilde{C}_{2,\hat{\mathbf{n}}})^2 = \{E|0, 0, 1\}$. When operating on a state carrying momentum \mathbf{k} , $(\tilde{C}_{2,\hat{\mathbf{n}}})^2$ is represented by $e^{i\mathbf{k}\cdot\hat{\mathbf{n}}}$. Hence if the nodal plane sits at momentum $\mathbf{k}\cdot\hat{\mathbf{n}} = \pi$, then $\tilde{C}_{2,\hat{\mathbf{n}}}^2 = -1$ and a two-fold orbital or sublattice degeneracy is ensured. When spin-degeneracy is also included, these states are then four-fold degenerate when SOC is ignored.

When SOC is included, it is possible to show that the TI pseudospin partners have the same $M_{\hat{\mathbf{n}}}$ mirror eigenvalue (this result is generalization of that given in Ref. [97] where $t_1 = 0$ and $t_2 = 0$ was used). That is, labeling the two Kramers degenerate states as $|+\rangle$ and $TI|+\rangle$, both belong to the same eigenstate of $\tilde{M}_{\hat{\mathbf{n}}}$. As a consequence, all Pauli matrices $\tilde{\sigma}_i$ made from the two states $|+\rangle$ $TI|+\rangle$ must all be invariant under $\tilde{M}_{\hat{\mathbf{n}}}$. It is this feature that differs from usual spin-1/2. Of the three Pauli matrices σ_i , constructed from usual spin-1/2 states, two will be odd under $\tilde{M}_{\hat{\mathbf{n}}}$ and one will be even under $\tilde{M}_{\hat{\mathbf{n}}}$. It is this symmetry distinction between the anomalous pseudospin operators ($\tilde{\sigma}_i$) and usual spin 1/2 operators (σ_i) that underlie the unusual superconducting properties discussed

below.

The above argument can also be applied to nodal lines generated by the symmetry elements $\{E, \tilde{C}_{2,\hat{n}}, TI, T\tilde{M}_{\hat{n}}\}$ with $(T\tilde{M}_{\hat{n}})^2 = -1$ when applied to orbital or sublattice degrees of freedom. In this case, repeating the same arguments above show that SOC will also split the band degeneracy and lead to anomalous pseudospin. Here, due to the larger available momentum phase space, we restrict our analysis and classification to nodal planes and leave an analysis of nodal lines to a later work. For all space groups that host nodal planes, we develop symmetry-based kp theories valid near all TRIM on these nodal planes. We emphasize these TRIM since Cooper pairs are formed by pairing states at momenta \mathbf{k} and $-\mathbf{k}$ with the momentum origin given by a TRIM. We then consider Fermi surfaces near these TRIM and discuss the resultant superconducting properties. Figure 1 illustrates our approach. Here, in green, we show the nodal planes and lines that exhibit anomalous pseudospin. Here we examine the properties of superconductivity for a Fermi surface near the Z point, which is a TRIM on the nodal plane. The properties of superconductivity for a Fermi surface near the Γ point, for which pseudospin is typically not anomalous, are described in earlier review articles [126, 127]. We note that many superconducting materials, including the examples discussed in this section, exhibit Fermi surfaces near nodal planes.

1.4.3 Nodal plane space groups and single-particle kp Hamiltonians

Here we identify all space groups that allow anomalous pseudospin on nodal planes and construct the corresponding symmetry-based kp -like Hamiltonians for all TRIM on these planes. A key new result is that these kp theories are of two types. Type 1 kp theories have Hamiltonians of the same form generically examined in locally non-centrosymmetric superconductors and explicitly contain SOC terms that are odd in momentum \mathbf{k} . Type 2 kp theories contain SOC terms that are *even* in momentum \mathbf{k} , and have not appeared in the context of locally non-centrosymmetric superconductors.

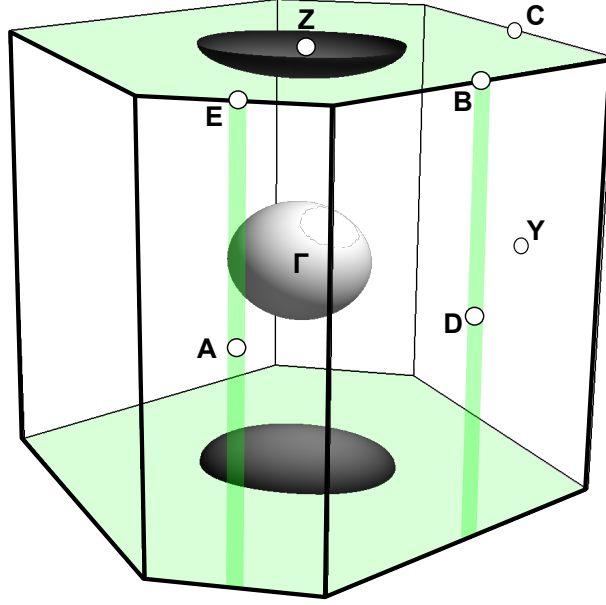


Figure 1-8: Example from space group 14 where the green shading reveals the planes and lines in momentum space on which anomalous pseudospin exists. A Fermi surface located near the momentum plane $k_z = \pi$ (as depicted by the dark Fermi surface near the Z point) will have its superconducting properties governed by pairing of anomalous pseudospin. However, Fermi surfaces far from these planes (such as that depicted near the Γ point) will exhibit more usual superconducting properties.

Space groups with nodal planes

To identify these nodal planes, all space groups containing inversion symmetry $I = \{I|0, 0, 0\}$ and the screw axis $\tilde{C}_{2,\hat{n}} = \{C_{2\hat{n}}|t_1, t_2, 1/2\}$ (where $t_1 = 0, 1/2$ and $t_2 = 0, 1/2$) were identified. For these space groups, the nodal planes lie on the Brillouin zone boundary. Table 1.3 lists the resultant space groups, point groups, nodal planes, and types of kp theories allowed for these space groups. As discussed in the previous section, the degeneracies of these nodal planes are generically lifted by SOC, yielding anomalous pseudospin.

Symmetry based kp theories near TRIM

Understanding the consequences of anomalous pseudospin on superconductivity requires a theory for the normal state. Cooper pairs rely on the degeneracy between states of momenta \mathbf{k} and $-\mathbf{k}$ and this degeneracy is ensured by both T and I symmetries. For this reason, we develop symmetry-based kp theories expanded around TRIM. To derive these kp -like Hamiltonians, we have used the real representations for the TRIM given in the Bilbao Crystallographic server [128–130]. For these

Table 1.3: Space groups with nodal planes

Crystal Type	Number	Name	Nodal planes	kp theory classes	
Monoclinic (C_{2h})	11	$P2_1/m$	$(u, 1/2, w)$	$C_{2h,1}^{\text{type1}}$	
	14	$P2_1/c$	$(u, 1/2, w)$	$C_{2h,1}^{\text{type1}}, C_{2h,2}^{\text{type2}}$	
Orthorhombic (D_{2h})	51	$Pmma$	$(1/2, v, w)$	$D_{2h,3}^{\text{type1}}$	
	52	$Pnna$	$(u, 1/2, w)$	$D_{2h,3}^{\text{type1}}, D_{2h,4}^{\text{type2}}, 8\text{-fold}$	
	53	$Pmna$	$(u, v, 1/2)$	$D_{2h,3}^{\text{type1}}, D_{2h,4}^{\text{type2}}$	
	54	$Pcca$	$(1/2, v, w)$	$D_{2h,3}^{\text{type1}}, 8\text{-fold}$	
	55	$Pbam$	$(1/2, v, w), (u, 1/2, w)$	$D_{2h,2}^{\text{type1}}, D_{2h,3}^{\text{type1}}$	
	56	$Pccn$	$(1/2, v, w), (u, 1/2, w)$	$D_{2h,2}^{\text{type1}}, D_{2h,2}^{\text{type2}}, 8\text{-fold}$	
	57	$Pbcm$	$(u, v, 1/2), (u, 1/2, w)$	$D_{2h,3}^{\text{type1}}, 8\text{-fold}$	
	58	$Pnmm$	$(1/2, v, w), (u, 1/2, w)$	$D_{2h,1}^{\text{type1}}, D_{2h,2}^{\text{type1}}, D_{2h,3}^{\text{type1}}, D_{2h,4}^{\text{type2}}$	
	59	$Pmnn$	$(1/2, v, w), (u, 1/2, w)$	$D_{2h,1}^{\text{type1}}, D_{2h,3}^{\text{type1}}$	
	60	$Pbcn$	$(1/2, v, w), (u, v, 1/2)$	$D_{2h,3}^{\text{type1}}, D_{2h,4}^{\text{type2}}, 8\text{-fold}$	
	61	$Pbca$	$(1/2, v, w), (u, v, 1/2), (u, 1/2, w)$	$D_{2h,1}^{\text{type1}}, D_{2h,3}^{\text{type1}}, 8\text{-fold}$	
	62	$Pnma$	$(1/2, v, w), (u, v, 1/2), (u, 1/2, w)$	$D_{2h,1}^{\text{type1}}, D_{2h,3}^{\text{type1}}, 8\text{-fold}$	
	63	$Cmcm$	$(u, v, 1/2)$	$C_{2h,1}^{\text{type1}}, D_{2h,3}^{\text{type1}}$	
	64	$Cmce$	$(u, v, 1/2)$	$C_{2h,2}^{\text{type2}}, D_{2h,3}^{\text{type1}}$	
	Tetragonal (D_{4h})	127	$P4/mbm$	$(u, 1/2, w)$	$D_{2h,3}^{\text{type1}}, D_{4h,2}^{\text{type2}}, D_{4h,4}^{\text{type2}}$
		128	$P4/mnc$	$(u, 1/2, w)$	$D_{2h,3}^{\text{type1}}, D_{2h,4}^{\text{type2}}, D_{4h,2}^{\text{type2}}, D_{4h,4}^{\text{type2}}, D_{4h,5}^{\text{type1}}, 8\text{-fold}$
129		$P4/nmm$	$(u, 1/2, w)$	$D_{2h,3}^{\text{type1}}, D_{4h,1}^{\text{type1}}, D_{4h,3}^{\text{type1}}$	
130		$P4/ncc$	$(u, 1/2, w)$	$D_{2h,3}^{\text{type1}}, D_{4h,1}^{\text{type1}}, D_{4h,3}^{\text{type1}}, 8\text{-fold}$	
135		$P4_2/mbc$	$(u, 1/2, w)$	$D_{2h,3}^{\text{type1}}, D_{4h,2}^{\text{type2}}, D_{4h,4}^{\text{type2}}, 8\text{-fold}$	
136		$P4_2/mnm$	$(u, 1/2, w)$	$D_{2h,3}^{\text{type1}}, D_{4h,1}^{\text{type1}}, D_{4h,2}^{\text{type2}}, D_{4h,3}^{\text{type1}}, D_{4h,4}^{\text{type2}}$	
137		$P4_2/nmc$	$(u, 1/2, w)$	$D_{2h,3}^{\text{type1}}, D_{4h,1}^{\text{type1}}, D_{4h,3}^{\text{type1}}, D_{4h,5}^{\text{type1}}, 8\text{-fold}$	
138		$P4_2/ncm$	$(u, 1/2, w)$	$D_{2h,3}^{\text{type1}}, D_{4h,1}^{\text{type1}}, D_{4h,2}^{\text{type2}}, D_{4h,3}^{\text{type1}}, D_{4h,4}^{\text{type2}}, 8\text{-fold}$	
Hexagonal (C_{6h})	176	$P6_3/m$	$(u, v, 1/2)$	$C_{2h,1}^{\text{type1}}, C_{6h}^{\text{type1}}, 8\text{-fold}$	
Hexagonal (D_{6h})	193	$P6_3/mcm$	$(u, v, 1/2)$	$D_{2h,3}^{\text{type1}}, D_{6h}^{\text{type1}}, 8\text{-fold}$	
	194	$P6_3/mmc$	$(u, v, 1/2)$	$D_{2h,3}^{\text{type1}}, D_{6h}^{\text{type1}}, 8\text{-fold}$	
Cubic (T_h)	205	$Pa\bar{3}$	$(u, 1/2, w)$	$D_{2h,3}^{\text{type1}}, 8\text{-fold}$	

TRIM, we initially consider space group irreducible representations that do not include spin, which, for simplicity, we name orbital representations. These representations are either 2-fold or 4-fold degenerate (when spin is added, these become 4-fold and 8-fold degenerate respectively). The full kp -like Hamiltonians are only listed for the 2-fold degenerate representations. We present a partial classification of the 4-fold degenerate orbital representations near the end of this section.

In constructing the kp theories for the 2-fold orbital degenerate TRIM points, we choose τ_i to be Pauli matrices that encode the orbital degrees of freedom, and σ_i to be spin Pauli matrices. We take $T = \tau_0(i\sigma_y)K$ where K is the complex conjugation operator, hence the τ_2 operator is odd under time-reversal. For a given doubly degenerate space group representation on a TRIM, constructing its direct product leads to four irreducible point group representations. These four representations each correspond to an orbital operator τ_i , and this partially dictates the momentum dependencies of symmetry allowed terms in the kp Hamiltonian. We present our results for the kp Hamiltonians in Table 1.4. The first row of each box gives the type of the kp theory class and the point group representations of the orbital operators that are given by Pauli matrices τ_i . In this decomposition, the square brackets correspond to the antisymmetric τ_2 operator and remaining terms correspond to τ_0 , τ_1 , and τ_3 . The second row of a box gives the kp Hamiltonian, and the last part of a box lists the space groups and TRIM points representations that belong to the kp Hamiltonian class. We have tabulated the kp Hamiltonians for 122 TRIM points and we find that only 13 different kp theories appear. These are of two types, which we call type 1 and type 2. Type 1 kp theories have degenerate even and odd parity orbital basis functions. These Hamiltonians have a structure similar to those examined in the context of locally non-centrosymmetric superconductors [93]. However, we note that local I breaking on crystal sites is not required to generate Type 1 kp theories. These Hamiltonians apply to all Wyckoff position site symmetries and the non-symmorphic groups we consider all include site symmetries that include I . For site symmetries that include I , the degenerate even and odd parity basis functions for type 1 Hamiltonians originate from the combination of non-symmorphic symmetries and Bloch momenta at the zone boundary. Type 2 kp theories have two degenerate orbital basis functions with the same parity symmetry. These Hamiltonian have a structure unlike that seen in locally noncentrosymmetric superconductors, yet

as we show below, they exhibit a similar magnetic response.

The generic form of these kp theories are

$$H(\mathbf{k}) = \varepsilon_{0,\mathbf{k}} + t_{1,\mathbf{k}}\tau_1 + t_{\alpha,\mathbf{k}}\tau_\alpha + \tau_\beta(\boldsymbol{\lambda}_{\mathbf{k}} \cdot \boldsymbol{\sigma}) = \varepsilon_{0,\mathbf{k}} + H_\delta(\mathbf{k}) , \quad (1.7)$$

$$(I, \tau_\alpha, \tau_\beta) = \begin{cases} (\tau_1, \tau_2, \tau_3) & \text{for type 1 ,} \\ (\tau_0, \tau_3, \tau_2) & \text{for type 2 ,} \end{cases} \quad (1.8)$$

where $H_\delta(\mathbf{k}) = H(\mathbf{k}) - \varepsilon_{0,\mathbf{k}}$ and α and β are type indices will be used the remaining context. For parity mixed, type 1, kp theories, the degeneracy at TRIM points is not broken by SOC. This is because the non-symmorphic symmetries combined with topological arguments imply these TRIM must have an odd number of Dirac lines passing through them [131]. These Dirac lines lie in the nodal plane. Elsewhere in the nodal plane, SOC lifts the 4-fold degeneracy. We will discuss some consequences of these Dirac lines later. The non trivial inversion symmetry for type 1, $I = \tau_1$, implies the parity of the momentum functions that $\varepsilon_{0,\mathbf{k}} = \varepsilon_{0,-\mathbf{k}}$, $t_{1,\mathbf{k}} = t_{1,-\mathbf{k}}$, $t_{2,\mathbf{k}} = -t_{2,-\mathbf{k}}$, and $\boldsymbol{\lambda}_{\mathbf{k}} = -\boldsymbol{\lambda}_{-\mathbf{k}}$. This form of Hamiltonian has often been used to understand locally non-centrosymmetric superconductors [90] and hidden spin polarization in inversion symmetric materials [99]. In these contexts, the orbital degrees of freedom reside on different sectors that are related by inversion symmetry and there is typically no symmetry requirement that ensures the SOC dominates. The τ_3 matrix is odd under inversion symmetry, allowing the odd-parity SOC $\boldsymbol{\lambda}_{\mathbf{k}}$ to appear. Many superconductors of interest have Fermi surfaces near type 1 TRIM points, examples include: Fe-based superconductors, which often have electron pockets near the M point in space group 129 (classes $D_{4h,1}^{\text{type1}}$ or $D_{4h,3}^{\text{type1}}$) [117], in this context the high T_c superconductor monolayer FeSe is of interest, since it only has Fermi surfaces near the M point [132]; CeRh₂As₂ which exhibits a field induced transition from an even parity to an odd-parity superconducting state [95, 96] and has Fermi surfaces near the M point in space group 129 (classes $D_{4h,1}^{\text{type1}}$ or $D_{4h,3}^{\text{type1}}$); BiS₂-based superconductors [116] which has superconductivity that survives to very high fields and which has electron pockets near the X point in space group 129 (class $D_{2h,3}^{\text{type1}}$); the odd-parity heavy fermion superconductor UPt₃ [118] which has a pancake-like Fermi surface at $k_z = \pi/c$ in space

group 193 (class D_{6h}^{type1}); and the ferromagnetic superconductor UCoGe [75] with space group 62 and a Fermi surface near the T point (class $D_{2h,1}^{\text{type1}}$).

For type 2 kp theories, the 4-fold degeneracy is sometimes already split into 2 at the TRIM point when SOC is added, unlike what occurs for type 1 kp theories. This happens in classes $C_{2h,2}^{\text{type2}}$ and $D_{2h,1}^{\text{type2}}$. For the other type 2 classes, this degeneracy at the TRIM point is not split. In these cases, an even number of Dirac lines pass through the TRIM point. These Dirac lines lie in the nodal plane. Since $I = \tau_0$ for type 2, all terms in the Hamiltonian are even parity, that is, unchanged under $\mathbf{k} \rightarrow -\mathbf{k}$. One example where type 2 kp theories apply is in strain induced superconductivity in RuO₂[133, 134]. Without strain, RuO₂ is thought to be a non-superconducting altermagnet [135]. When strain is applied, bands near the X - M - R - A Brillouin zone face are most strongly affected [133]. RuO₂ has space group 136 with the R and M points belonging to classes $D_{2h,4}^{\text{type2}}$, $D_{4h,2}^{\text{type2}}$, or $D_{4h,4}^{\text{type2}}$. Later we discuss the ferromagnetic superconductor UCoGe with space group 62 [75]. In this example, we highlight the role of 8-fold degenerate points which exhibit some properties similar to that found for type 2 TRIM points.

Type 1 and type 2 kp Hamiltonians share some common features that play an important role in understanding the properties of the superconducting states. The first is that the non-symmorphic symmetry dictates that these Hamiltonians are best described as two-band systems with eigenenergies given by

$$E_{\pm}(\mathbf{k}) = \varepsilon_{0,\mathbf{k}} \pm \sqrt{t_{1,\mathbf{k}}^2 + t_{\alpha,\mathbf{k}}^2 + |\boldsymbol{\lambda}_{\mathbf{k}}|^2} = \varepsilon_{0,\mathbf{k}} \pm \varepsilon_{\delta,\mathbf{k}} , \quad (1.9)$$

where α is the type index in Eq. 1.8. The second feature is that both simplify dramatically on the nodal plane, where only the coefficient functions $\varepsilon_{0,\mathbf{k}}$ and $\boldsymbol{\lambda}_{\mathbf{k}} \cdot \hat{\mathbf{n}}$ are non-vanishing (that is $t_{1,\mathbf{k}} = t_{2,\mathbf{k}} = t_{3,\mathbf{k}} = |\boldsymbol{\lambda}_{\mathbf{k}} \times \hat{\mathbf{n}}| = 0$). This property is a direct consequence of the anomalous pseudospin. The symmetry arguments discussed in the previous section enforce this condition. In particular, for momenta on the nodal plane, the mirror operator through the nodal plane, U_M , takes the form $U_M = -i\tau_{\beta}(\boldsymbol{\sigma} \cdot \hat{\mathbf{n}})$. The requirement that these Hamiltonians obey time-reversal and inversion symmetries and commute with U_M leads to this simple form of the kp theories in the nodal plane. The final important property of these kp Hamiltonians is that the SOC terms are often the leading order terms in the kp expansions, that is, they appear with the lowest powers

Table 1.4: Classification of kp theories. Subscript numbering of momenta represents different real representations on the same momentum point, and a permutation of the axes is denoted by the cyclic notation. For example, $128(X_{1,2}(xyz))$ represents that there are two representations X_1 and X_2 on $X = (0, 1/2, 0)$ space group 128, and their local theory is obtained by $D_{2h,3}^{\text{type1}}$ Hamiltonian under $x \rightarrow y \rightarrow z \rightarrow x$ relabelling. The representation convention is following Bilbao Crystallographic server^a[128–130] except for the L point in 193 and 194.

Class	Symmetry		
	Hamiltonian		
	Space Group Momenta		
$C_{2h,1}^{\text{type1}}$	$A_g + B_g + [A_u] + B_u$	$D_{2h,4}^{\text{type2}}$	$A_g + B_{1g} + B_{3g} + [B_{2g}]$
	$H = \epsilon_0 + (t_{1x}k_x + t_{1z}k_z)k_y\tau_1 + t_2k_y\tau_2$ $+ \tau_3[\lambda_xk_y\sigma_x + (\lambda_{yz}k_x + \lambda_{yz}k_z)\sigma_y + \lambda_zk_y\sigma_z]$		$H = \epsilon_0 + t_1k_xk_y\tau_1 + t_3k_yk_z\tau_3$ $+ \tau_2[\lambda_xk_xk_y\sigma_x + \lambda_y\sigma_y + \lambda_zk_yk_z\sigma_z]$
	11(C_1, D_1, E_1, Z_1), 14(C_1, Z_1) 63($R_1(yz)$), 176($L_1(yz)$)		52(T_1^\pm), 53($U_1^\pm(yz)$), $R_1^\pm(yz)$ 58($T_1^\pm, U_1^\pm(xy)$), 60($S_1^\pm(xy)$) 128(R_1^\pm), 136(R_1^\pm)
$C_{2h,2}^{\text{type2}}$	$A_g + 2B_g + [A_g]$	$D_{4h,1}^{\text{type1}}$	$A_{1g} + B_{2g} + [A_{1u}] + B_{2u}$
	$H = \epsilon_0 + (t_{1x}k_x + t_{1z}k_z)k_y\tau_1 + (t_{3x}k_x + t_{3z}k_z)k_y\tau_3$ $+ \tau_2[(\lambda_{xx}k_x + \lambda_{xz}k_z)k_y\sigma_x + \lambda_y\sigma_y + (\lambda_{zx}k_x + \lambda_{zz}k_z)k_y\sigma_z]$		$H = \epsilon_0 + t_1k_xk_y\tau_1 + t_2k_xk_yk_z(k_x^2 - k_y^2)\tau_2$ $+ \tau_3[\lambda_x(k_x\sigma_y + k_y\sigma_x) + \lambda_3k_xk_yk_z\sigma_z]$
	14($D_1^\pm D_2^\pm, E_1^\pm E_2^\pm$), 64($R_1^\pm R_2^\pm(yz)$)		129($M_{1,2}, A_{1,2}$), 130($M_{1,2}$) 136($A_{3,4}$), 137($M_{1,2}$), 138($M_{1,2}$)
$D_{2h,1}^{\text{type1}}$	$A_g + B_{1g} + [A_u] + B_{1u}$	$D_{4h,2}^{\text{type2}}$	$A_{1g} + 2B_{2g} + [A_{1g}]$
	$H = \epsilon_0 + t_1k_xk_y\tau_1 + t_2k_xk_yk_z\tau_2$ $+ \tau_3[\lambda_xk_y\sigma_x + \lambda_yk_x\sigma_y + \lambda_zk_xk_yk_z\sigma_z]$		$H = \epsilon_0 + t_1k_xk_y\tau_1 + t_3k_xk_y\tau_3$ $+ \tau_2[\lambda_x(k_yk_z\sigma_x + k_xk_z\sigma_y) + \lambda_zk_xk_y(k_x^2 - k_y^2)\sigma_z]$
	56($S_{1,2}$), 58($R_{1,2}$) 59($S_{1,2}, R_{1,2}$), 62($T_{1,2}(xz)$)		127($M_1^\pm M_4^\pm, M_2^\pm M_3^\pm, A_1^\pm A_4^\pm, A_2^\pm A_3^\pm$) 128($M_1^\pm M_4^\pm, M_2^\pm M_3^\pm$), 135($M_1^\pm M_4^\pm, M_2^\pm M_3^\pm$) 136($M_1^\pm M_4^\pm, M_2^\pm M_3^\pm$), 138($A_1^\pm A_4^\pm, A_2^\pm A_3^\pm$)
$D_{2h,2}^{\text{type2}}$	$A_g + 2B_{1g} + [A_g]$	$D_{4h,3}^{\text{type1}}$	$A_{1g} + B_{2g} + [B_{1u}] + A_{2u}$
	$H = \epsilon_0 + t_1k_xk_y\tau_1 + t_3k_xk_y\tau_3$ $+ \tau_2[\lambda_xk_yk_z\sigma_x + \lambda_yk_xk_z\sigma_y + \lambda_zk_xk_y\sigma_z]$		$H = \epsilon_0 + t_1k_xk_y\tau_1 + t_2k_xk_yk_z\tau_2$ $+ \tau_3[\lambda_x(k_x\sigma_y - k_y\sigma_x) + \lambda_zk_xk_yk_z(k_x^2 - k_y^2)\sigma_z]$
	55($S_1^\pm S_2^\pm, S_3^\pm S_4^\pm, R_1^\pm R_2^\pm, R_3^\pm R_4^\pm$), 56($R_1^\pm R_2^\pm, R_3^\pm R_4^\pm$) 58($S_1^\pm S_2^\pm, S_3^\pm S_4^\pm$), 62($U_1^\pm U_4^\pm, U_2^\pm U_3^\pm$)		129($M_{3,4}, A_{3,4}$), 130($M_{3,4}$) 136($A_{1,2}$), 137($M_{3,4}$), 138($M_{3,4}$)
$D_{2h,3}^{\text{type1}}$	$A_g + B_{2g} + [B_{3u}] + B_{1u}$	$D_{4h,4}^{\text{type2}}$	$A_{1g} + A_{2g} + B_{2g} + [B_{1g}]$
	$H = \epsilon_0 + t_1k_xk_z\tau_1 + t_2k_x\tau_2$ $+ \tau_3[\lambda_xk_y\sigma_x + \lambda_yk_x\sigma_y + \lambda_zk_xk_yk_z\sigma_z]$		$H = \epsilon_0 + t_1k_xk_y(k_x^2 - k_y^2)\tau_1 + t_3k_xk_y\tau_3$ $+ \tau_2[\lambda_x(k_yk_z\sigma_x + k_xk_z\sigma_y) + \lambda_zk_xk_y\sigma_z]$
	51($X_{1,2}, S_{1,2}, U_{1,2}, R_{1,2}$), 52($R_{1,2}(xy), Y_{1,2}(xyz)$) 53($Z_{1,2}(zyx), T_{1,2}(zyx)$), 54($X_{1,2}, S_{1,2}$) 55($U_{1,2}(yz), X_{1,2}(yz), Y_{1,2}(xyz), T_{1,2}(xyz)$) 56($X_{1,2}, Y_{1,2}(xy)$) 57($S_{1,2}(xyz), Y_{1,2}(xyz), Z_{1,2}(zyx), U_{1,2}(zyx)$) 58($X_{1,2}(yz), Y_{1,2}(xyz)$) 59($X_{1,2}, U_{1,2}, T_{1,2}(xy), Y_{1,2}(xy)$), 60($X_{1,2}, Z_{1,2}(zyx)$) 61($X_{1,2}, Y_{1,2}(xyz), Z_{1,2}(zyx)$) 62($X_{1,2}, Z_{1,2}(xz), Y_{1,2}(xyz)$) 63($T_{1,2}(zyx), Z_{1,2}(zyx)$), 64($T_{1,2}(zyx), Z_{1,2}(zyx)$) 127($X_{1,2}(xyz), R_{1,2}(xyz)$), 128($X_{1,2}(xyz)$) 129($X_{1,2}(xy), R_{1,2}(xy)$), 130($X_{1,2}(xy)$) 135($X_{1,2}(xyz), R_{1,2}(xyz)$), 136($X_{1,2}(xyz)$) 137($R_{1,2}(xy), X_{1,2}(xy)$), 138($X_{1,2}(xy)$) 193($L_{1,2}$), 194($L_{1,2}(xy)$) 205($X_{1,2}(xyz)$)		127(M_5^\pm, A_5^\pm), 128(M_5^\pm) 135(M_5^\pm), 136(M_5^\pm), 138(A_5^\pm)
		$D_{4h,5}^{\text{type1}}$	$A_{1g} + A_{2g} + [B_{1u}] + B_{2u}$
			$H = \epsilon_0 + t_1k_xk_y(k_x^2 - k_y^2)\tau_1 + t_2k_xk_yk_z\tau_2$ $+ \tau_3[\lambda_x(k_x\sigma_y + k_y\sigma_x) + \lambda_zk_xk_yk_z\sigma_z]$
			128($A_{1,2}$), 137($A_{1,2}$)
		C_{6h}^{type1}	$A_g + B_g + [A_u] + B_u$
			$H = \epsilon_0 + (t_{1x}k_x(k_x^2 - 3k_y^2) + t_{1y}k_y(3k_x^2 - k_y^2))k_z\tau_1$ $+ t_2k_z\tau_2 + \tau_3[\lambda_xk_z(2k_xk_y\sigma_x + (k_x^2 - k_y^2)\sigma_y)$ $+ (\lambda_{zx}k_x(k_x^2 - 3k_y^2) + \lambda_{zy}k_y(3k_x^2 - k_y^2))\sigma_z]$
			176(A_1)
		D_{6h}^{type1}	$A_{1g} + B_{2g} + [A_{2u}] + B_{1u}$
			$H = \epsilon_0 + t_1k_xk_z(k_x^2 - 3k_y^2)\tau_1 + t_2k_z\tau_2$ $+ \tau_3[\lambda_xk_z(2k_xk_y\sigma_x + (k_x^2 - k_y^2)\sigma_y) + \lambda_zk_y(3k_x^2 - k_y^2)\sigma_z]$
			193($A_{1,2}$), 194($A_{1,2}(xy)$)

^a<https://www.cryst.ehu.es/> Representations and Applications \rightarrow Point and Space Groups \rightarrow - Representations \rightarrow SG Physically irreducible representations given in a real basis

of k_i . This is the case for classes $C_{2h,2}^{type2}$, $D_{2h,1}^{type1}$, $D_{2h,4}^{type2}$, $D_{4h,2}^{type1}$, $D_{4h,3}^{type1}$, and $D_{4h,5}^{type1}$. This feature ensures that there exists a limit in which the SOC is the dominant single-particle interaction on the Fermi surface and hence the unusual magnetic superconducting response we later discuss must exist.

1.4.4 Superconducting states

In the previous section, complete symmetry-dictated kp theories were found for anomalous pseudospin. These theories are complete in the sense that they include all operators of the form $\tau_i\sigma_j$ allowed by symmetry. For superconductivity, the orbital degree of freedom enlarges the corresponding space of possible gap functions compared to the usual even-parity (pseudospin-singlet) $\tilde{\Delta}(\mathbf{k}) = \psi_{\mathbf{k}}(i\sigma_y)$ and odd-parity (pseudospin-triplet) $\tilde{\Delta}(\mathbf{k}) = \mathbf{d}_{\mathbf{k}} \cdot \boldsymbol{\sigma}(i\sigma_y)$ states that appear in single-band theories [126, 127]. Nevertheless, it is possible to understand some general properties of the allowed pairing states.

To deduce the symmetry properties of possible pairing channels in this larger space of electronic states, it is useful to define gap function differently than usual [136, 137]. In particular, we take

$$\mathcal{H} = \sum_{i,j,\mathbf{k}} H_{ij}(\mathbf{k}) c_{\mathbf{k},i}^\dagger c_{\mathbf{k},j} + \frac{1}{2} \sum_{i,j,\mathbf{k}} [\Delta_{ij}(\mathbf{k}) c_{\mathbf{k},i}^\dagger \tilde{c}_{\mathbf{k},j}^\dagger + h.c.]. \quad (1.10)$$

where i, j are combined spin and orbital indices, $h.c.$ means Hermitian conjugate, $c_{\mathbf{k}}(c_{\mathbf{k}}^\dagger)$ is the Fermionic spin-half particle creation(annihilation) operator, and $\tilde{c}_{\mathbf{k}}(\tilde{c}_{\mathbf{k}}^\dagger)$ is the time reversed partner of $c_{\mathbf{k}}(c_{\mathbf{k}}^\dagger)$. In the usual formulation $\tilde{c}_{\mathbf{k},j}^\dagger$ is replaced $c_{-k,j}^\dagger$ which leads to a different gap function $\tilde{\Delta}_{ij}$ and to difficulties in interpreting the symmetry transformation properties of this gap function [136, 137]. For a single-band, these new gap functions become $\Delta(\mathbf{k}) = \psi_{\mathbf{k}}\sigma_0$ for even-parity and $\Delta(\mathbf{k}) = \mathbf{d}_{\mathbf{k}} \cdot \boldsymbol{\sigma}$ for odd-parity. The key use of Eq. 1.10 is that the $\Delta_{ij}(\mathbf{k})$ transform under rotations in the same way as the $H_{ij}(\mathbf{k})$, allowing the symmetry properties of the gap functions to be deduced. The disadvantage of this approach is that the antisymmetry of the gap functions that follow from the Pauli exclusion principle is not as readily apparent compared to the usual formulation [136, 137].

Enforcing the Pauli exclusion principle leads to eight types of gap functions that generalize

the pseudospin-singlet and pseudospin-triplet of single-band gap functions. Six of these are simple generalizations of the single-band gap functions: $\tau_i\psi_{\mathbf{k}}$ and $\tau_i(\mathbf{d}_{\mathbf{k}} \cdot \boldsymbol{\sigma})$ for $i = 0, 1$, and 3 where $\psi_{-\mathbf{k}} = \psi_{\mathbf{k}}$ and $\mathbf{d}_{-\mathbf{k}} = -\mathbf{d}_{\mathbf{k}}$. Two are new gap functions: $\tau_2(\boldsymbol{\psi}_{\mathbf{k}} \cdot \boldsymbol{\sigma})$ and $\tau_2 d_{\mathbf{k}}$ with $\boldsymbol{\psi}_{-\mathbf{k}} = \boldsymbol{\psi}_{\mathbf{k}}$ and $d_{-\mathbf{k}} = -d_{\mathbf{k}}$. It is possible to determine whether these gap functions are either even or odd-parity and this depends upon whether the $k\mathcal{P}$ Hamiltonian is type 1 or type 2. These gap functions and their parity symmetry are listed in Table 1.5. Without further consideration of additional symmetries, the gap function will in general be a linear combination of all the even (or odd) parity gap functions.

To gain an understanding of the relative importance of these pairing states it is useful to project these gaps onto the band basis. Such a projection is meaningful if the energy separation between the two bands is much larger than the gap magnitude. For many of the $k\mathcal{P}$ Hamiltonians, due to the presence of Dirac lines, there will exist regions in momentum space for which this condition is not satisfied. However, these regions represent a small portion of the Fermi surface when the SOC energies are much larger than the gap energies, so that an examination of the projected gap is still qualitatively useful in this limit. Provided the superconducting state does not break time-reversal symmetry, the projected gap magnitude on band a can be found through [138]

$$\tilde{\Delta}_{\pm}^2 = \frac{\text{Tr}[\{H_{\delta}, \Delta\}^2 P_{\pm}]}{\text{Tr}[|H_{\delta}|^2]}. \quad (1.11)$$

where $P_{\pm}(\mathbf{k}) = \frac{1}{2}(1 \pm H_{\delta}(\mathbf{k})/\varepsilon_{\delta,\mathbf{k}})$ which is a projection operator onto \pm band by the energy dispersion Eq. 1.9. This projected gap magnitude is related to superconducting fitness [82, 83]: if it vanishes, the corresponding gap function is called unfit and will have a $T_c = 0$ in the weak coupling limit. Table 1.5 gives the projected gap functions for the pairing states discussed above. The projection generally reduces the size of the gap, with the exception of the usual even-parity $\tau_0\psi_{\mathbf{k}}$ state (interestingly, the odd-parity $\tau_0(\mathbf{d}_{\mathbf{k}} \cdot \boldsymbol{\sigma})$ state has a gap that is generically reduced). This reduction strongly suppresses the T_c of the pairings state, where it enters exponentially in the weak-coupling limit. We later examine the different $k\mathcal{P}$ classes to identify fit gap functions since the T_c of these states will be the largest, given a fixed attractive interaction strength.

On the nodal plane, the projected gap functions, shown in Table 1.5, simplify considerably since

only ε_0 and $\boldsymbol{\lambda}_{\mathbf{k}} \cdot \hat{\mathbf{n}}$ are non-zero. For both type 1 and type 2 Hamiltonians, this leads to two gap functions that are fully fit, that is, not reduced by the projection. For type 1 Hamiltonians, these fully fit states are $\tau_0\psi_{\mathbf{k}}$ and $\tau_3\psi_{\mathbf{k}}$. The state $\tau_0\psi_{\mathbf{k}}$ is even-parity and the state $\tau_3\psi_{\mathbf{k}}$ is odd-parity and, as discussed later, these two states play an important role in the appearance of a field-induced transition from even to odd parity superconductivity as observed in CeRh₂As₂. For gap functions described by vectors, for example $\mathbf{d}_{\mathbf{k}}$, the projected gaps on the nodal plane are of the form $|\mathbf{d}_{\mathbf{k}} \cdot \hat{\mathbf{n}}|^2$ or $|\mathbf{d}_{\mathbf{k}} \times \hat{\mathbf{n}}|^2$. This is qualitatively different than the usual odd-parity single-band gap, where the gap magnitude is $|\mathbf{d}_{\mathbf{k}}|^2$. The latter requires that all three components of $\mathbf{d}_{\mathbf{k}}$ must vanish to have nodes. For the projected gaps on the nodal planes, this requirement is less stringent: only one or two components of $\mathbf{d}_{\mathbf{k}}$ need to vanish to have nodes. This is closely related to the violation of Blount's theorem on the nodal planes.

Gap projection and the violation of Blount's theorem

Blount's theorem states that time-reversal symmetric odd-parity superconductors cannot have line nodes when SOC is present [136]. Key to Blount's theorem is the assumption that pseudospin shares the same symmetry properties as usual spin [136]. The violation of Blount's theorem in non-symmorphic space groups has been demonstrated through an examination of Cooper pair representations formed from antisymmetric direct products of the relevant fermions states.[106–108, 110, 113, 114, 139]. Here we use an alternate approach that exploits the completeness of the kp Hamiltonian space and the inclusion of all gap functions in this space that are allowed by symmetry to directly compute the general form of the superconducting excitation spectrum. This approach closely links the anomalous pseudospin to the violation of Blount's theorem.

The existence of anomalous pseudospin requires the presence of the translation mirror symmetry $\tilde{M}_{\hat{\mathbf{n}}}$. Consequently, the gap function can be classified as even or odd under this symmetry. Momenta on the nodal plane are invariant under $\tilde{M}_{\hat{\mathbf{n}}}$. Hence, for these momenta, $U_M^\dagger \Delta(\mathbf{k}) U_M = \pm \Delta(\mathbf{k})$ where the + (–) holds for a mirror-even (mirror-odd) gap function. For our basis choice $U_M = -i\tau_\beta(\boldsymbol{\sigma} \cdot \hat{\mathbf{n}})$. Importantly, for both types the kp theories on the nodal plane are given by $H(\mathbf{k}) = \varepsilon_{0,\mathbf{k}} + iU_M(\boldsymbol{\lambda}_{\mathbf{k}} \cdot \hat{\mathbf{n}})$. This defines the two bands $E_\pm(\mathbf{k}) = \varepsilon_{0,\mathbf{k}} \pm |\boldsymbol{\lambda}_{\mathbf{k}} \cdot \hat{\mathbf{n}}|$. Written in the band basis, we can divide

Table 1.5: Classification of allowed pairing states for the kp theories. For both type I and II TRIMs we give the symmetry under inversion, the gap projection onto the Fermi surface, and the gap on the nodal plane. The momentum subscript indices \mathbf{k} of the coefficient functions are omitted here.

Type 1

Gap function	Inversion	Gap projection	Gap on nodal plane
$\tau_0\psi$	+	$ \psi ^2$	$ \psi ^2$
$\tau_0(\mathbf{d} \cdot \boldsymbol{\sigma})$	-	$\frac{(t_1^2 + t_2^2) \mathbf{d} ^2 + \mathbf{d} \cdot \boldsymbol{\lambda} ^2}{t_1^2 + t_2^2 + \boldsymbol{\lambda} ^2}$	$ \mathbf{d} \cdot \hat{\mathbf{n}} ^2$
$\tau_3\psi$	-	$\frac{ \boldsymbol{\lambda} ^2 \psi ^2}{t_1^2 + t_2^2 + \boldsymbol{\lambda} ^2}$	$ \psi ^2$
$\tau_3(\mathbf{d} \cdot \boldsymbol{\sigma})$	+	$\frac{ \mathbf{d} \cdot \boldsymbol{\lambda} ^2}{t_1^2 + t_2^2 + \boldsymbol{\lambda} ^2}$	$ \mathbf{d} \cdot \hat{\mathbf{n}} ^2$
$\tau_1\psi$	+	$\frac{t_1^2 \psi ^2}{t_1^2 + t_2^2 + \boldsymbol{\lambda} ^2}$	0
$\tau_1(\mathbf{d} \cdot \boldsymbol{\sigma})$	-	$\frac{t_1^2 \mathbf{d} ^2 + \mathbf{d} \times \boldsymbol{\lambda} ^2}{t_1^2 + t_2^2 + \boldsymbol{\lambda} ^2}$	$ \mathbf{d} \times \hat{\mathbf{n}} ^2$
τ_2d	+	$\frac{t_2^2 \mathbf{d} ^2}{t_1^2 + t_2^2 + \boldsymbol{\lambda} ^2}$	0
$\tau_2(\boldsymbol{\psi} \cdot \boldsymbol{\sigma})$	-	$\frac{t_2^2 \boldsymbol{\psi} ^2 + \boldsymbol{\psi} \times \boldsymbol{\lambda} ^2}{t_1^2 + t_2^2 + \boldsymbol{\lambda} ^2}$	$ \boldsymbol{\psi} \times \hat{\mathbf{n}} ^2$

Type 2

Gap function	Inversion	Gap projection	Gap on nodal plane
$\tau_0\psi$	+	$ \psi ^2$	$ \psi ^2$
$\tau_0(\mathbf{d} \cdot \boldsymbol{\sigma})$	-	$\frac{(t_1^2 + t_2^2) \mathbf{d} ^2 + \mathbf{d} \cdot \boldsymbol{\lambda} ^2}{t_1^2 + t_2^2 + \boldsymbol{\lambda} ^2}$	$ \mathbf{d} \cdot \hat{\mathbf{n}} ^2$
$\tau_3\psi$	+	$\frac{t_3^2 \psi ^2}{t_1^2 + t_3^2 + \boldsymbol{\lambda} ^2}$	0
$\tau_3(\mathbf{d} \cdot \boldsymbol{\sigma})$	-	$\frac{t_3^2 \mathbf{d} ^2 + \mathbf{d} \times \boldsymbol{\lambda} ^2}{t_1^2 + t_3^2 + \boldsymbol{\lambda} ^2}$	$ \mathbf{d} \times \hat{\mathbf{n}} ^2$
$\tau_1\psi$	+	$\frac{t_1^2 \psi ^2}{t_1^2 + t_3^2 + \boldsymbol{\lambda} ^2}$	0
$\tau_1(\mathbf{d} \cdot \boldsymbol{\sigma})$	-	$\frac{t_1^2 \mathbf{d} ^2 + \mathbf{d} \times \boldsymbol{\lambda} ^2}{t_1^2 + t_3^2 + \boldsymbol{\lambda} ^2}$	$ \mathbf{d} \times \hat{\mathbf{n}} ^2$
τ_2d	-	$\frac{ \boldsymbol{\lambda} ^2 \mathbf{d} ^2}{t_1^2 + t_3^2 + \boldsymbol{\lambda} ^2}$	$ \mathbf{d} ^2$
$\tau_2(\boldsymbol{\psi} \cdot \boldsymbol{\sigma})$	+	$\frac{ \boldsymbol{\psi} \cdot \boldsymbol{\lambda} ^2}{t_1^2 + t_3^2 + \boldsymbol{\lambda} ^2}$	$ \boldsymbol{\psi} \cdot \hat{\mathbf{n}} ^2$

the pairing potential into intraband and interband components. On the nodal plane the intraband gap functions are explicitly given by

$$P_{\pm}\Delta P_{\pm} = \frac{1}{4}(-U_M \pm i \operatorname{sgn}(\boldsymbol{\lambda}_{\mathbf{k}} \cdot \hat{\mathbf{n}}))\{U_M, \Delta\}, \quad (1.12)$$

while the interband components are

$$P_{\pm}\Delta P_{\mp} = \frac{1}{4}(-U_M \pm i \operatorname{sgn}(\boldsymbol{\lambda}_{\mathbf{k}} \cdot \hat{\mathbf{n}}))[U_M, \Delta] \quad (1.13)$$

We observe that since a mirror-even gap function satisfies $[U_M, \Delta] = 0$, the interband gap components must vanish on the nodal plane, i.e. the pairing only involves particles from the same band.

The general form of the BdG energy dispersion relation is then

$$\pm' \sqrt{(\varepsilon_{0,\mathbf{k}} \pm |\boldsymbol{\lambda}_{\mathbf{k}} \cdot \hat{\mathbf{n}}|)^2 + |\Delta_{\pm\pm}|^2}, \quad (1.14)$$

where intraband gap magnitude $|\Delta_{\pm\pm}|^2 = \frac{1}{4}\operatorname{Tr}[|P_{\pm}\Delta P_{\pm}|^2]$ and \pm' is the particle-hole symmetry index which is independent of band index \pm . Since there is no requirement that $|\Delta_{\pm\pm}|^2 = 0$, line nodes are therefore not expected on the nodal plane, but rather we should generically find two-gap behavior with different size gaps on the two bands. In contrast, for the mirror-odd gap functions we have $\{U_M, \Delta\} = 0$, so there is no intraband pairing on the nodal plane. The general form of the eigenenergies for this interband pairing state is then

$$\pm' \left(\pm |\boldsymbol{\lambda}_{\mathbf{k}} \cdot \hat{\mathbf{n}}| + \sqrt{\varepsilon_{0,\mathbf{k}}^2 + |\Delta_{\pm\mp}|^2} \right), \quad (1.15)$$

where intraband gap magnitude $|\Delta_{\pm\mp}|^2 = \frac{1}{4}\operatorname{Tr}[|P_{\pm}\Delta P_{\mp}|^2]$. The gap has line nodes provided $|\boldsymbol{\lambda}_{\mathbf{k}} \cdot \hat{\mathbf{n}}|^2 > |\Delta_{\pm\mp}|^2$. This result depends only on the mirror-odd symmetry of the gap, and not on the parity symmetry. Since gaps that are odd under both mirror and parity symmetry are allowed, this result shows that odd-parity gaps can have line nodes, thus demonstrating a violation of Blount's theorem.

The origin of these nodes due to purely interband pairing implies that the nodes are shifted off

the Fermi surface [140]. If the spin-orbit coupling is too weak, i.e. $|\boldsymbol{\lambda}_{\mathbf{k}} \cdot \hat{\mathbf{n}}|^2 < |\Delta_{\pm\mp}|^2$, the nodes can annihilate with each other and are absent. This possibility has been discussed in the context of even parity superconductivity in monolayer FeSe [141] and odd-parity superconductivity in UPt₃ [139]. The analysis above is valid even when Dirac lines pass through the TRIM points, as is the case in most of the derived kp theories. On the Dirac lines, the condition $|\boldsymbol{\lambda}_{\mathbf{k}} \cdot \hat{\mathbf{n}}|^2 < |\Delta_{\pm\mp}|^2$ must occur and the spectrum is therefore gapped.

Unconventional pairing states from electron-phonon interactions

To highlight how the pairing of anomalous pseudospin can differ from the single-band superconductivity, it is instructive to consider an attractive U Hubbard model. Such a model is often used to capture the physics of electron-phonon driven s -wave superconductivity in single-band models. Here we show that this coupling also allows unconventional pairings states. In particular, odd-parity states in type 1 kp Hamiltonians. Such a state has recently likely been observed in CeRh₂As₂.

Here we consider a local Hubbard- U attraction on each site of the lattice and do not consider any longer range Coulomb interactions. These sites are defined by their Wyckoff positions. Importantly, for the non-symmorphic groups we have considered here, each Wyckoff position has a multiplicity greater than one. Here we limit our discussion to Wyckoff positions with multiplicity two, which implies that there are two inequivalent atoms per unit cell. An attractive U on these sites stabilizes a local spin-singlet Cooper pair. Since there are two sites per unit cell this implies that there are two stable superconducting degrees of freedom per unit cell. These two superconducting states can be constructed by setting the phase of Cooper pair wavefunction on each site to be the same or opposite. Since only local interactions are included, both these two states will have the same pairing interaction. The in-phase state is a usual s -wave $\tau_0\psi_{\mathbf{k}}$ state. Identifying the other, out of phase, superconducting state requires an understanding of the relationship between the basis states for the kp Hamiltonians and orbitals located at the Wyckoff positions. In general, this will depend on the specific orbitals included in the theory. However, the condition that the resultant pairing states must be spin-singlet and local in space (hence momentum independent) allows only two possibilities for this additional pairing state: it is either a $\tau_1\psi_{\mathbf{k}}$ or a $\tau_3\psi_{\mathbf{k}}$ pairing state. Of

these states, for two reasons, the $\tau_3\psi_{\mathbf{k}}$ state for type 1 Hamiltonians is of particular interest. The first reason is that this state is odd-parity and therefore offers a route towards topological superconductivity [142, 143]. The second reason is that of the four possible states ($\tau_1\psi_{\mathbf{k}}$ or $\tau_3\psi_{\mathbf{k}}$ for type 1 or type 2 Hamiltonians), this is the only state that is fully fit on the nodal plane (as can be seen in Table 1.5, the other three states have zero gap projection on the nodal plane). This implies that for type 1 Hamiltonians, the odd-parity $\tau_3\psi_{\mathbf{k}}$ and the s -wave $\tau_0\psi_{\mathbf{k}}$ states can have comparable T_c since they both have the same pairing interaction. In practice, the $\tau_3\psi_{\mathbf{k}}$ state will have a lower T_c than the $\tau_0\psi_{\mathbf{k}}$ state since it will not be fully fit away from the nodal plane. Table 1.5 reveals that this projection is given by the ratio $|\lambda_{\mathbf{k}}|^2/(t_{1,\mathbf{k}}^2 + t_{2,\mathbf{k}}^2 + |\lambda_{\mathbf{k}}|^2)$. For classes $D_{2h,1}^{\text{type1}}$, $D_{4h,1}^{\text{type1}}$, $D_{4h,3}^{\text{type1}}$, and $D_{4h,5}^{\text{type1}}$, this ratio is nearly one since the SOC terms are the largest in the kp Hamiltonian. This suggests that these classes offer a promising route toward stabilizing odd-parity superconductivity. We stress that because $|\lambda_{\mathbf{k}}|^2/(t_{1,\mathbf{k}}^2 + t_{2,\mathbf{k}}^2 + |\lambda_{\mathbf{k}}|^2)$ is slightly less than one, the T_c of the odd-parity $\tau_3\psi_{\mathbf{k}}$ will be comparable but less than that of the usual s -wave state. However, as we discuss later, the $\tau_3\psi_{\mathbf{k}}$ state can be stabilized over the usual s -wave $\tau_0\psi_{\mathbf{k}}$ state in an applied field. The identification of classes $D_{2h,1}^{\text{type1}}$, $D_{4h,1}^{\text{type1}}$, $D_{4h,3}^{\text{type1}}$, and $D_{4h,5}^{\text{type1}}$ that maximize the T_c of odd-parity pairing from electron-phonon interactions allows the earlier theory for a field induced even to odd parity transition CeRh₂As₂ [97] (with space group 129) to be generalized to many other space groups.

While the above odd-parity state is only relevant for type 1 Hamiltonians, for type 2 Hamiltonians, the usual s -wave interaction can develop a novel structure. In particular, for the classes $C_{2h,2}^{\text{type2}}$ and $D_{2h,4}^{\text{type2}}$, Table 1.4 shows that the state $\tau_2\sigma_y$ is maximally fit and has s -wave symmetry. Consequently, this state will admix with the usual s -wave $\tau_0\psi$ state. The theory describing this admixture formally resembles that of a Hund pairing mechanism proposed to explain the appearance of nodes in the likely s -wave superconductor KFe₂As₂ [144]. The results of this analysis and a follow up analysis [145] allow some of the properties of this state to be understood. An important conclusion of these works is that an s -wave superconducting state can emerge even when pairing for the usual s -wave state is repulsive (that is for the Hubbard $U > 0$). This holds if two conditions are met: the effective interaction for the $\tau_2\sigma_y$ state is attractive (to first approximation, this effective

interaction does not depend upon U [144, 145]) and the two bands that emerge in the kp theory both cross the chemical potential. This s -wave pairing state naturally leads to nodes.

1.4.5 Role of Magnetic Fields

The role of anomalous pseudospin is perhaps most unusual in response to magnetic fields. In many superconductors, there has been a push to drive up the magnetic field at which these are operational. Ising superconductors are one class of materials for which this has been successful, the in-plane critical field far surpasses the Pauli field, opening the door to applications [146]. Another relevant example is the field induced transition from an even parity to an odd-parity state observed in CeRh_2As_2 [95, 96].

Recently, a powerful method to examine the response of superconductors to time-reversal symmetry-breaking fields has been developed by the projection onto the band-basis[138]. The form of the kp theories we have developed allows for the direct application of this projection method. The response of superconductivity to time-reversal symmetry-breaking is described by a time-reversal symmetry-breaking interaction $H_{\mathbf{h}}(\mathbf{k})$. A common form of TRSB Hamiltonian, and the one we emphasize here, is the Zeeman field interaction term, which is represented by

$$H_{\mathbf{h}}(\mathbf{k}) = \tau_0(\mathbf{h} \cdot \boldsymbol{\sigma}) , \quad (1.16)$$

where \mathbf{h} is a magnetic field parameter in the system. We note that our qualitative results apply to a broader range of TRSB Hamiltonians. In particular, this is true if the TRSB field shares the same symmetry properties as a Zeeman field (for example if $H_{\mathbf{h}}(\mathbf{k})$ describes the coupling between orbital angular momentum and an applied field).

The theory introduces two parameters that quantify the response of superconductivity to time-reversal symmetry-breaking. The first parameter is an effective g -factor given by

$$\tilde{g}_{\pm, \mathbf{k}, \mathbf{h}}^2 = \frac{2\text{Tr}[\{H_{\delta}, H_{\mathbf{h}}\}^2 P_{\pm}]}{\text{Tr}[|H_{\delta}|^2]\text{Tr}[|H_{\mathbf{h}}|^2]} . \quad (1.17)$$

The second parameter is the field-fitness, given by

$$\tilde{F}_{\pm, \mathbf{k}, \mathbf{h}} = \frac{\text{Tr}[|\{\{H_\delta, \tilde{\Delta}\}, \{H_\delta, H_{\mathbf{h}}\}\}|^2 P_\pm]}{2\text{Tr}[|\{H_\delta, H_{\mathbf{h}}\}|^2 P_\pm] \text{Tr}[|\{H_\delta, \tilde{\Delta}\}|^2 P_\pm]} . \quad (1.18)$$

This field-fitness function ranges in value from zero to one. When the field-fitness is zero, the superconducting state is not suppressed by the time-reversal symmetry breaking perturbation. With these two parameters, the response of superconductivity to applied fields and the temperature dependence of magnetic susceptibility in the superconducting state can be determined. With the choice of the time-reversal symmetry-breaking field as the Zeeman field, Eq. 1.16, one finds

$$\tilde{g}_{\pm, \mathbf{k}, \mathbf{h}}^2 = \frac{t_{1, \mathbf{k}}^2 + t_{\alpha, \mathbf{k}}^2 + (\boldsymbol{\lambda}_{\mathbf{k}} \cdot \hat{\mathbf{h}})^2}{t_{1, \mathbf{k}}^2 + t_{\alpha, \mathbf{k}}^2 + \boldsymbol{\lambda}_{\mathbf{k}}^2} \quad (1.19)$$

where α is a type index that is 2 for type 1 and 3 for type 2. This agrees with results in [147] derived for Hamiltonians that resemble type 1 Hamiltonians. We note that the band index \pm and the magnitude of field \mathbf{h} in the field-fitness and the g -factor do not change the outcome, thus they will be omitted in the subsequent sections and they will be denoted by $\tilde{F}_{\mathbf{k}, \hat{\mathbf{h}}}^2$ and $\tilde{g}_{\mathbf{k}, \hat{\mathbf{h}}}^2$.

Even parity superconductors

It can be shown that the field-fitness parameter in Eq. 1.18 is 1 for all even parity states. Consequently, the magnetic response is governed solely by the generalized g -factor given in Eq. 1.19. For momenta on the nodal plane, where $t_{1, \mathbf{k}} = t_{2, \mathbf{k}} = t_{3, \mathbf{k}} = \boldsymbol{\lambda}_{\mathbf{k}} \times \hat{\mathbf{n}} = 0$, the g -factor vanishes for magnetic fields orthogonal to $\hat{\mathbf{n}}$. This is a direct consequence of the anomalous pseudospin, since the symmetries of the Pauli matrices formed from anomalous pseudospin do not allow any coupling to a Zeeman field perpendicular to $\hat{\mathbf{n}}$. An immediate consequence is that superconductivity survives to much stronger fields than expected for these field orientations. However, momenta that do not sit on the nodal plane also contribute to the superconducting state and their contribution needs to be included as well. To quantify this, we solve for the Pauli limiting field within weak coupling

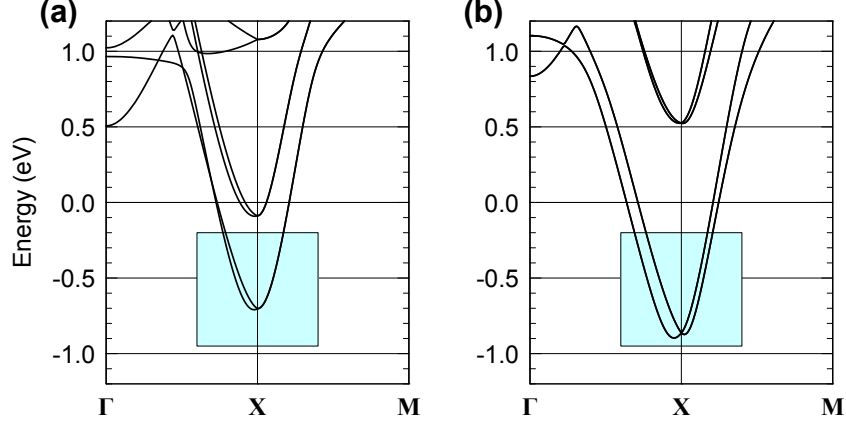


Figure 1-9: DFT bands of BiS₂ near the X point (a) without and (b) with the SOC. The bands highlighted in the box are our focus.

theory at zero temperature. For an isotropic s -wave superconductor, we find

$$\ln \frac{h_{P,\hat{h}}}{h_0} = -\langle \ln |\tilde{g}_{\mathbf{k},\hat{h}}| \rangle_{\mathbf{k}} \quad (1.20)$$

for field along direction \hat{h} , where h_0 is the usual Pauli limiting field (found when the SOC is ignored), and $\langle \cdot \rangle_{\mathbf{k}}$ means an average over the Fermi surface weighted by the density of states. Below, we apply this formula to BiS₂-based superconductors. We note that the spin susceptibility in the superconducting state can also be expressed using $\tilde{g}_{\mathbf{k},\hat{h}}$ as well [138], and this shows that a non-zero spin susceptibility is predicted at zero temperature whenever the critical field surpasses h_0 .

Enhanced in plane field Pauli for BiS₂-based superconductors

Here we turn to recent experimental results on BiS₂-based superconductors [116, 148]. This material has the tetragonal space group 129 (P4/nmm) and it exhibits two electron pockets about the two equivalent X points [149, 150]. When S is replaced with Se, it has been observed that the in-plane upper critical field surpasses the usual Pauli limiting field by a factor of 7 [148]. While it has been suggested that the local non-centrosymmetric structure is the source of this large critical field [148], there has been no quantitative calculation for this. Here we apply Eq. 1.20 to the kp theory at the X -point to see if it is possible to account for this large critical field. The X point in space group 129 belongs to class $D_{2h,3}^{\text{type1}}$. For BiS₂, the dispersion is known to be strongly

two-dimensional (2D) [116, 149] so we consider the kp theory in the 2D limit. This kp theory is

$$H_{\text{BiS}_2} = \frac{\hbar^2}{2m} (k_x^2 + \gamma^2 k_y^2) - \mu + t_2 k_y \tau_2 + \lambda_x k_y \tau_3 \sigma_x + \lambda_y k_x \tau_3 \sigma_y. \quad (1.21)$$

Assuming s -wave superconductivity and accounting for the two equivalent pockets yields

$$h_{P,\hat{\mathbf{x}}} = h_0 \frac{\sqrt{t_2^2 + \lambda_x^2} + |\gamma \lambda_y|}{\sqrt{|t_2| + |\gamma \lambda_y|} (t_2^2 + \lambda_x^2)^{1/4}} \quad (1.22)$$

where h_0 is the usual Pauli limiting field. For simplicity we consider $\gamma = 1$ in the following. Eq. 1.22 reveals that a large enhancement of the limiting field is possible and requires two conditions. The first is that $t_2 \ll \lambda_x, \lambda_y$ and second is that there is substantial anisotropy in λ_x and λ_y . To understand if these conditions are reasonable, we have carried out density-functional theory (DFT) calculations on $\text{LaO}_{1/2}\text{F}_{1/2}\text{BiS}_2$ with and without SOC. DFT calculations for $\text{LaO}_{1/2}\text{F}_{1/2}\text{BiS}_2$ were carried out by the full-potential linearized augmented plane wave method [151]. The Perdew-Burke-Ernzerhof form of the exchange correlation functional [152], wave function and potential energy cutoffs of 14 and 200 Ry, respectively, muffin-tin sphere radii of 1.15, 1.2, 1.3, 1.0 Å for Bi, S, La, O atoms, respectively, the experimental lattice parameters [153], and an $15 \times 15 \times 5$ k -point mesh were employed for the self-consistent field calculation. The virtual crystal approximation was used by setting the nuclear charge $Z = 8.5$ at O(F) sites. The resultant bands are shown in Fig. 1-9. Without SOC, the band splitting along Γ to X yields an estimate for t_2 . When SOC is present, the band splitting along the X to M yields λ_y and the band splitting along Γ to X yields $\sqrt{\lambda_x^2 + t_2^2}$. The DFT calculated splittings suggest that λ_x is the largest parameter by a factor of 3-4, while t_2 and λ_y are comparable. This suggests that the conditions to achieve a large critical field are realistic in BiS_2 -based superconductors. Note that the largest observed Pauli fields are found when the S is substituted by Se [148]. Se has a larger SOC than S, suggesting that the λ_i parameters will be increased from what we estimate here. This is currently under exploration.

It is worthwhile contrasting the above theory with that for Fe-based materials in which electron pockets exist near the M point of space group 129. The M -point is described by class $D_{4h,1}^{\text{type1}}$. In this case, an analysis similar to BiS_2 gives an enhancement of only $\sqrt{2}$ of the Pauli field for in-plane

fields. For c -axis fields, this class implies a significantly enhanced Pauli limiting field. These results are consistent with experimental fits to upper critical fields in Fe-based superconductors that reveal that the upper critical field for in-plane fields are Pauli suppressed while those for field along the c -axis are not [154]. The contrast between Fe-based materials and BiS₂-based materials highlights the importance of the different classes. In particular, the lower orthorhombic symmetry of the X point allows protection to in-plane fields not afforded to the M point, where the theory is strongly constrained by tetragonal symmetry.

Pair density wave states. In BCS theory, a spin-singlet superconductor is suppressed by the Zeeman effect. Under a sufficiently strong magnetic field, the pairing susceptibility can be peaked at non-zero Cooper pair momenta, leading to a pair density wave or FFLO state [155–157]. A schematic phase diagram for a centrosymmetric system is shown in the left panel of Fig. 1-10. The typically first order phase transition (double solid line) between the uniform and FFLO state ends at a bicritical point (T_b, H_b) , i.e. FFLO state only exists for $T < T_b$. A weak-coupling calculation reveals that for the usual FFLO phase, $T_b/T_c = 0.56$

It is known that for locally non-centrosymmetric superconductors, FFLO-like phases can appear at lower fields H_b and higher temperatures T_b than the usual FFLO-like instability [93]. This is closely linked to the symmetry required instability to a pair density wave state for non-centrosymmetric superconductors when a field is applied [90]. For a non-centrosymmetric system under magnetic field, both inversion and time-reversal symmetry are broken. As a result, the pairing susceptibility is generically peaked at non-zero momentum and $T_b = T_c$. For locally non-centrosymmetric superconductors, inversion symmetry is locally broken on each sublattice. In an extreme case, if the two sublattices are decoupled, then the system effectively becomes non-centrosymmetric, and under a small magnetic field, an FFLO state can exist right below the zero-field superconducting T_c . However, these sublattices are generically coupled so that $T_b = T_c$ is not realized in practice. Here we show that for type 1 Hamiltonians, FFLO-like states can in principle exist up to $T_b = T_c$.

To show this, we consider the 2D version of class $D_{4h,1}^{\text{type1}}$ and use the pairing susceptibility to

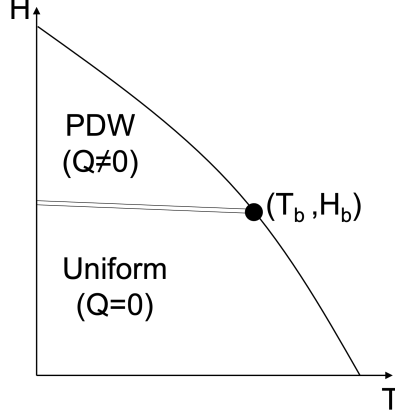


Figure 1-10: Schematic phase diagram for a spin-singlet superconductor under Zeeman effect. Single solid lines denote continuous phase transitions while double solid lines denote first-order phase transitions.

calculate T_b and H_b . In 2D, class $D_{4h,1}^{\text{type1}}$ has the following normal state Hamiltonian:

$$H_{D_{4h,1}} = \frac{\hbar^2}{2m}(k_x^2 + k_y^2) - \mu + t_1 k_x k_y \tau_1 + \lambda_x \tau_3 (k_y \sigma_x + k_x \sigma_y) + H_x \sigma_x \quad (1.23)$$

λ_x denotes the strength of the local inversion symmetry breaking (local Rashba SOC), while t_1 is the inter-sublattice coupling. The pairing susceptibility for an s -wave state with gap function $\tau_0 \psi_{\mathbf{k}}$ is

$$\chi_{\text{pairing}}(\mathbf{Q}) = -\frac{1}{\beta} \sum_{\omega_n} \sum_{(\mathbf{p}, \mathbf{p}+\mathbf{Q}) \in \text{FS}} \text{Tr} [G_0(\mathbf{Q} + \mathbf{p}, \omega_n) G_0(\mathbf{p}, \omega_n)], \quad (1.24)$$

where G_0 is the normal state Green's function written in Nambu space. The FFLO state is favored, if the pairing susceptibility is peaked at non-zero \mathbf{Q} . We examine the position of the bicritical point (T_b, H_b) , as a function of $\lambda_x/(t_1 k_F)$. We use the following two equations to locate the bicritical point: (1) The bicritical point lies on the BCS transition for the uniform superconductivity. (2) The bicritical point is a continuous phase transition between uniform and FFLO superconductivity, where $\nabla_{\mathbf{Q}}^2 \chi_{\text{pairing}}(\mathbf{Q}) = 0$. The result is in Fig. 1-11. 1000×1000 points are sampled in the 2D Brillouin zone. Other parameters are $t_1 = 0.2$, $t = \mu = 1$. An energy cutoff of $E_c = 0.1$ is applied to determine the position of the Fermi surface.

These results show that for zero $\lambda_x/k_F t_1$, a usual FFLO phase is found (that is $T_b/T_c \approx 0.56$).

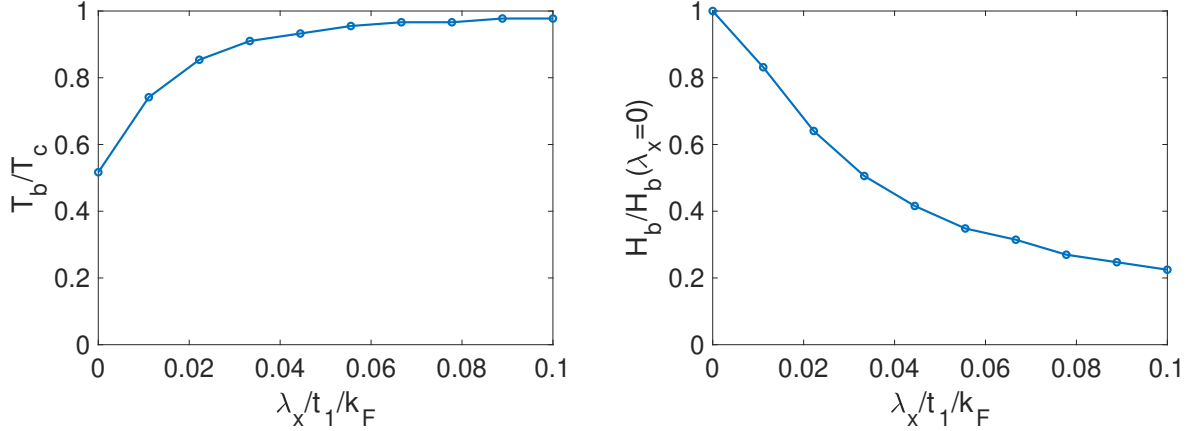


Figure 1-11: The position of the bicritical point (T_b, H_b) , as a function of $\lambda_x / k_F t_1$.

As the SOC λ_x increases or equivalently, as k_F decreases, T_b increases and approaches the zero-field critical temperature. In the meantime, H_b monotonically decreases.

We have shown that the FFLO phase can exist up to $T_b = T_c$ for a 2D version of class $D_{4h,1}^{\text{type1}}$. Key is that SOC is the leading order term in the kp theory and this is also the case for other type 1 Hamiltonians. Hence the optimal conditions for an enhanced FFLO phase to occur are when fields are applied in-plane (perpendicular to the c -axis) for classes $D_{2h,1}^{\text{type1}}$, $D_{4h,1}^{\text{type1}}$, $D_{4h,3}^{\text{type1}}$, and $D_{4h,5}^{\text{type1}}$.

Odd-parity superconductors

For odd parity superconductors, the field fitness parameter $\tilde{F}_{\mathbf{k}, \hat{\mathbf{h}}}$ can become less than 1 [138]. Of particular interest is when $\tilde{F}_{\mathbf{k}, \hat{\mathbf{h}}} = 0$ since this implies that T_c is unchanged by the time-reversal symmetry breaking field (this is independent of the effective g -factor) [138]. For anomalous pseudospin this possibility leads to two consequences not expected for spin-triplet states made from usual spin-1/2 fermions. The first is a field induced transition from an even to an odd parity state. The second is that, in spite of the presence of strong SOC, the superconducting state is immune to magnetic fields for all field orientations. We discuss these each in turn.

Field induced even to odd parity transitions

In CeRh_2As_2 , a field induced even to odd parity transition has been observed for the field oriented along the c -axis in this tetragonal material [95, 96]. Earlier, we argued that this was due the anomalous pseudospin that arises on the Brillouin zone faces in the non-symmorphic space

group P4/nmm [97]. Here we show how this can be generalized to other space groups that admit type 1 kp theories and determine which classes are optimal for observing such a transition. As discussed in Section IV C, an attractive electron-phonon like interaction gives rise to both both a usual s -wave $\tau_0\psi_{\mathbf{k}}$ state and an odd-parity $\tau_3\psi_{\mathbf{k}}$ state. These two states have the same pairing interaction, but the gap projected onto the band basis is generally smaller for the $\tau_3\psi_{\mathbf{k}}$ state than for the $\tau_0\psi_{\mathbf{k}}$ state, implying that $\tau_0\psi_{\mathbf{k}}$ state has the higher T_c . For the type 1 classes $D_{2h,1}^{\text{type1}}$, $D_{4h,1}^{\text{type1}}$, $D_{4h,3}^{\text{type1}}$, and $D_{4h,5}^{\text{type1}}$, anomalous pseudospin leads to T_c 's that are nearly the same for the even $\tau_0\psi$ and odd-parity $\tau_3\psi$ states. These classes are therefore promising for observing a field induced transition from an even-parity to an odd-parity state.

To determine if a such a field induced transition occurs we compute $\tilde{F}_{\mathbf{k},\hat{\mathbf{h}}}$ for a pairing state $\tilde{\Delta} = \tau_3$. We find for type 1 kp theories

$$\tilde{F}_{\mathbf{k},\hat{\mathbf{h}}} = \frac{(\hat{\mathbf{h}} \cdot \boldsymbol{\lambda}_{\mathbf{k}})^2 (t_{1,\mathbf{k}}^2 + t_{2,\mathbf{k}}^2 + |\boldsymbol{\lambda}_{\mathbf{k}}|^2)}{|\boldsymbol{\lambda}_{\mathbf{k}}|^2 [\hat{\mathbf{h}}^2 (t_{1,\mathbf{k}}^2 + t_{2,\mathbf{k}}^2) + (\hat{\mathbf{h}} \cdot \boldsymbol{\lambda}_{\mathbf{k}})^2]}. \quad (1.25)$$

Notice if $\hat{\mathbf{h}} \cdot \boldsymbol{\lambda}_{\mathbf{k}} = 0$, then $\tilde{F}_{\mathbf{k},\hat{\mathbf{h}}} = 0$ which maximizes T_c . To determine the field orientations for which $\tilde{F}_{\mathbf{k},\hat{\mathbf{h}}} = 0$, we examine the form of $\boldsymbol{\lambda}_{\mathbf{k}}$ in the type 1 classes discussed above. In all these classes, the $\lambda_{z,\mathbf{k}}$ component appears with a higher power of momenta than the other components. Consequently, the field should be applied along the \hat{z} direction. As an example, consider the class $D_{4h,3}^{\text{type1}}$. Here $\lambda_{z,\mathbf{k}} \propto k_x k_y k_z (k_x^2 - k_y^2)$ while $\lambda_{x,\mathbf{k}} \propto k_y$ and $\lambda_{y,\mathbf{k}} \propto k_x$. In this case $\boldsymbol{\lambda}_{\mathbf{k}}$ will be in-plane to an excellent approximation, and an even to odd-parity transition can be expected for the field along the c -axis. Consequently, classes $D_{2h,1}^{\text{type1}}$, $D_{4h,1}^{\text{type1}}$, $D_{4h,3}^{\text{type1}}$, and $D_{4h,5}^{\text{type1}}$ and, hence, space groups 56, 58, 59, 62, 128, 129, 130, 136, 137, and 138 are promising for realizing a field-induced even to odd parity transition.

Field immune odd-parity superconductivity For a conventional spin-triplet superconductor (with $\Delta = \mathbf{d}_{\mathbf{k}} \cdot \boldsymbol{\sigma}$) formed from usual spin-1/2 pseudospin, SOC typically pins the direction of the vector $\mathbf{d}_{\mathbf{k}}$. If the applied field is perpendicular to $\mathbf{d}_{\mathbf{k}}$, that is if $\mathbf{d}_{\mathbf{k}} \cdot \hat{\mathbf{h}} = 0$, then the T_c for this field orientation is unchanged [158–160]. Since there exists at least one field direction for which $\mathbf{d}_{\mathbf{k}} \cdot \hat{\mathbf{h}} \neq 0$, it is not expected that usual spin-triplet superconductors are immune to fields applied

in all directions. For anomalous pseudospin, this is not the case, it is possible for an odd-parity state to be robust against suppression for arbitrarily oriented magnetic fields. To show how this is possible, we calculate $\tilde{F}_{\mathbf{k},\hat{\mathbf{h}}}$ for $\Delta = \tau_0(\mathbf{d}_{\mathbf{k}} \cdot \boldsymbol{\sigma})$ for type 1 kp theories, this yields

$$\tilde{F}_{\mathbf{k},\hat{\mathbf{h}}} = \frac{[(t_{1,\mathbf{k}}^2 + t_{2,\mathbf{k}}^2)\mathbf{d}_{\mathbf{k}} \cdot \hat{\mathbf{h}} + (\mathbf{d}_{\mathbf{k}} \cdot \boldsymbol{\lambda}_{\mathbf{k}})(\boldsymbol{\lambda}_{\mathbf{k}} \cdot \hat{\mathbf{h}})]^2}{[(t_{1,\mathbf{k}}^2 + t_{2,\mathbf{k}}^2)\hat{\mathbf{h}}^2 + (\boldsymbol{\lambda}_{\mathbf{k}} \cdot \hat{\mathbf{h}})^2][(t_{1,\mathbf{k}}^2 + t_{2,\mathbf{k}}^2)|\mathbf{d}_{\mathbf{k}}|^2 + (\mathbf{d}_{\mathbf{k}} \cdot \boldsymbol{\lambda}_{\mathbf{k}})^2]}. \quad (1.26)$$

We first note that near the nodal plane, the effective g -factor is small for in-plane fields $\hat{\mathbf{n}} \cdot \mathbf{h} = 0$, so that for these field orientations superconductivity is not strongly suppressed (this is true for both even and odd-parity superconducting states). Hence, to show that an odd-parity state survives for all field orientations, we need to show that $\tilde{F}_{\mathbf{k},\hat{\mathbf{h}}} \approx 0$ for a field applied along the nodal plane normal where $\boldsymbol{\lambda}_{\mathbf{k}} \cdot \hat{\mathbf{h}}$ becomes maximal. Near the plane we expect that $\boldsymbol{\lambda}_{\mathbf{k}} \cdot \hat{\mathbf{h}} \gg \sqrt{t_{1,\mathbf{k}}^2 + t_{2,\mathbf{k}}^2}$. Also, $(t_{1,\mathbf{k}}^2 + t_{2,\mathbf{k}}^2)$ is small compared to $\boldsymbol{\lambda}_{\mathbf{k}}^2$, so $\tilde{F}_{\mathbf{k},\hat{\mathbf{h}}}$ is dominated by the $\mathbf{d}_{\mathbf{k}} \cdot \boldsymbol{\lambda}_{\mathbf{k}}$ term in the numerator. Hence if the denominator $|t_{1,2}\mathbf{d}_{\mathbf{k}}|$ is much bigger than $\mathbf{d}_{\mathbf{k}} \cdot \boldsymbol{\lambda}_{\mathbf{k}}$, then $\tilde{F}_{\mathbf{k},\hat{\mathbf{h}}} \approx 0$. Given that $\lambda_{\hat{\mathbf{n}}}$ is the largest SOC component, this requirement is equivalent to $\lambda_{\perp} \ll t_{1,2}$ and $\mathbf{d}_{\mathbf{k}} \perp \hat{\mathbf{n}}$ (where λ_{\perp} is the magnitude of the SOC perpendicular to $\hat{\mathbf{n}}$).

As a relevant example of the above mechanism we consider UPt₃ [118]. The superconducting state in UPt₃ is believed to be an E_{2u} state, with order parameter $\Delta = \eta_p(\sigma_x k_y + \sigma_y k_x) + \eta_f \sigma_z k_z k_x k_y$ (we only include one component of this two-component order parameter since similar arguments hold for the second component). In general, since the p-wave and f-wave components have the same symmetry, both η_p and η_f are non-zero. However, theories based on the usual pseudospin typically require $\eta_p = 0$ due to the experimental observations discussed below [110, 161, 162]. Below we further show that $\eta_p = 0$ is not required for these experimental observations when anomalous pseudospin is considered. Indeed, these experiments are consistent with $\eta_f = 0$ and $\eta_p \neq 0$ if pairing occurs predominantly near the nodal plane $k_z = \pi/c$.

Thermal conductivity experiments suggest the existence of line nodes [118]. For usual pseudospin, the state $\sigma_x k_y + \sigma_y k_x$ is either fully gapped or has only point nodes. This is one reason to expect that $\eta_p = 0$. However, as illustrated in Table 1.4, line nodes are expected for this state on the $k_z = \pi/c$ plane (note this conclusion also follows from Refs [111, 112, 114]). This is relevant

for UPt_3 since it is known to have the ‘starfish’ Fermi surface near this nodal plane [118] which belongs to class D_{6h}^{type1}

In terms of paramagnetic suppression, the superconducting state is known to be more robust under $\mathbf{B} \perp \hat{z}$ compared to $\mathbf{B} \parallel \hat{z}$ [162]. For the usual pseudospin, this requires $\mathbf{d}_{\mathbf{k}} \parallel \hat{z}$, and thus $\eta_p = 0$. However, on the ‘starfish’ Fermi surface, the small g -factor for $\mathbf{B} \perp \hat{z}$ can serve to protect the p-wave state against paramagnetic suppression. As discussed above, the suppression from $\mathbf{B} \parallel \hat{z}$ depends on the ratio $\lambda_{x,y}/t_{1,2}$, while the g -factor for $\mathbf{B} \perp \hat{z}$ depends on the ratio $(t_{1,2}, \lambda_{x,y})/\lambda_z$. The requirement $\lambda_{x,y}/t_{1,2} > (t_{1,2}, \lambda_{x,y})/\lambda_z$ is thus sufficient to match the observations on the upper critical fields. If both ratios are much smaller than one, the p-wave state is immune to paramagnetic suppression for field along arbitrary directions. This could be relevant to the approximately unchanged Knight shift in the superconducting state [163]. We note that the use of $\tilde{F}_{\mathbf{k}, \hat{\mathbf{h}}}$ to determine the magnetic response relies on the validity of projection to a single band. However, for class D_{6h}^{type1} band degeneracies exist along three Dirac lines for which this projection is not valid.

1.4.6 8-fold degenerate points: application to UCoGe

The arguments presented above relied on the 4-fold degeneracy at TRIM points when SOC is not present. However, some of these TRIM points have an 8-fold degeneracy without SOC. It is reasonable to ask if the conclusions found for kp theories of 4-fold degenerate points discussed above survive to 8-fold degenerate points. We find that in most cases, the 8-fold degeneracy at these TRIM is split by a single SOC term of the form $O\sigma_i$ where O is a momentum independent 4 by 4 orbital matrix. In Table 1.6, we give the direction of the spin component σ_i that appears in this SOC term at the TRIM point. The existence of this single SOC term ensures small effective g -factors for fields perpendicular to the spin-component direction. Consequently, the conclusions associated with the effective g -factor anisotropy discussed in Section V still hold for these 8-fold degenerate points. We note that the 8-fold degeneracy at the A point of space groups 130 and 135 are not split by SOC and these points provide examples of double Dirac points examined in [164, 165].

Table 1.6: Spin alignment of 8-fold degenerate TRIM.

Spin Alignment	Space Group Momenta
σ_x	54(U_1U_2),54(R_1R_2),56(U_1U_2),60(R_1R_2),61(S_1S_2),62(S_1S_2),205(M_1M_2)
σ_y	52(S_1S_2),56(T_1T_2),57(T_1T_2),57(R_1R_2),61(T_1T_2),130(R_1R_2),138(R_1R_2)
σ_z	60(T_1T_2),60(U_1U_2),61(U_1U_2),62(R_1R_2),128(A_3A_4), 137(A_3A_4),176(A_2A_3),193(A_3),194(A_3)

One material for which these 8-fold degenerate points are likely to be relevant is the ferromagnetic superconductor UCoGe, which crystalizes in space group 62 (Pnma) [75]. UCoGe is believed to be a possibly topological odd-parity superconductor [75, 109]. Our Fermi surface (given in Figure 3) reveals that all Fermi surface sheets lie near nodal planes with anomalous pseudospin and further reveal tube-shaped pockets that enclose the zone-boundary S point and stretch along the S-R axis. Here we focus on these Fermi surfaces. This feature reasonably agrees with previous works [166–168] using local density approximation and the existence of these tube shaped Fermi surfaces is consistent with quantum oscillation measurements [169]. Here density-functional theory calculations for UCoGe were carried out by the full-potential linearized augmented plane wave method [151]. Perdew-Burke-Ernzerhof form of exchange correlation functional [152], wave function and potential energy cutoffs of 16 and 200 Ry, respectively, muffin-tin sphere radii of 1.4 Å for U and 1.2 Å for Co and Ge, respectively, the experimental lattice parameters [170], and an $8 \times 12 \times 8$ k -point mesh were employed for the self-consistent field calculation. Spin-orbit was fully taken into account in the assumed nonmagnetic state. Fermi surface was determined on a dense $30 \times 50 \times 30$ k -point mesh and visualized by using FermiSurfer [171].

Both the R and S points are 8-fold degenerate TRIM when SOC is not included for space group 62. Interestingly, from Table 1.6, the effective g -factors for fields along \hat{y} and \hat{z} directions are zero at the S-point and are zero for fields along \hat{x} and \hat{y} directions at the R-point. This indicates that superconductivity (both even and odd-parity) on the tube-shaped Fermi surfaces will be robust against magnetic fields applied along the \hat{y} direction. This is the field direction for which the upper critical field is observed to be the highest and for which an unusual S-shaped critical field curve appears [75]. We leave a detailed examination of the consequences of anomalous pseudospin in space group 62 on superconductivity to a later work.

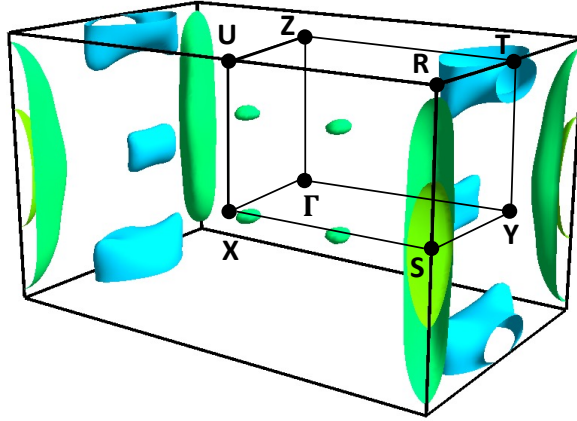


Figure 1-12: DFT Fermi surface of UCoGe.

1.4.7 Conclusions

Non-symmorphic symmetries allow the existence of nodal planes at Brillouin zone edges when no SOC is present. When SOC is added, the pseudospin on these nodal planes has different symmetry properties than usual pseudospin-1/2. Here we have classified all space groups and effective single-particle theories near TRIM points on these nodal planes and examined the consequences of this anomalous pseudospin on the superconducting state. We have shown how this enhances the T_c for odd-parity superconducting states due to attractive interactions, leads to unexpected superconducting nodal properties, allows large Pauli limiting fields and pair density wave states for spin-singlet superconductors, gives rise to field immune odd-parity superconductivity, and to field driven even to odd-parity superconducting transitions. Some of these properties have also been predicted for locally non-centrosymmetric superconductors, however anomalous pseudospin applies even when the crystal site symmetry contains inversion symmetry. This greatly extends the number of materials that can exhibit this superconducting response. While we have emphasized nodal planes on which anomalous pseudospin exists, there are also materials for which anomalous pseudospin develops on nodal lines and not on nodal planes. Some such materials also exhibit unusual response to magnetic fields [172–174], suggesting a broader range of applicability for anomalous pseudospin superconductivity.

Chapter 2

Gravitational Wave Physics

2.1 Overview

Since the first detection of gravitational waves in 2015 [175], collaborations from LIGO (Laser Interferometer Gravitational-Wave Observatory), Virgo, and KAGRA (Kamioka Gravitational Wave Detector) have detected 90 mergers, comprising binary black holes (BBH), binary neutron stars (BNS), and neutron star-black hole (NSBH) pairs, during the first three observing runs (O1, O2, and O3) [176–178]. The fourth observing run (O4) began on 24 May 2023 and is currently ongoing. With the increasing number of detections, it allows a statistical study on the astrophysical rates and the population of mergers [179]. Beyond the binary merger events, the collaborations have also been conducting researches on different gravitational wave origins, such as dark matter searches [180]. In this chapter, I will discuss two topics related to the gravitational wave physics: the application of machine learning in spacetime volume sensitivity measurements and the search for dark matter evidence from glitch events in LIGO detectors.

2.2 Determining LIGO Spacetime Volume Sensitivity by Machine Learning

2.2.1 Introduction

$\langle VT \rangle$ represents the spatial volume surveyed by the detectors multiplied by duration of observation, which is mathematically defined later as Eq. 2.3 [181]. The rate of compact binary coalescence events is proportional to $\langle VT \rangle$, which is a key parameter in the gravitational wave astronomy. The spacetime volume sensitivity is a measure of the detector's ability to detect gravitational waves. $\langle VT \rangle$ is often measured through injection campaigns, where simulated signals are injected into the detector noise and the detection pipeline is run to determine how many signals are successfully recovered. However, the injection campaign demands substantial computational resources and varies with population models. This means that testing all intriguing population models through injection campaigns would require a large amount of computational resources and efforts. In this section, I utilize deep neural networks (DNN) to reduce the computational load in measuring $\langle VT \rangle$. This will eventually enable easier testing of $\langle VT \rangle$ across different population models.

The primary objective of this research is to train machine learning (ML) models to estimate $\Delta\Lambda$ for each injection trigger, which is a constituent element of $\langle VT \rangle$ mathematically defined later by Eq. 2.5. While the conventional injection campaign involves heavy calculations of an actual pipeline, machine learning models make a rapid prediction of $\Delta\Lambda$ values through a pretrained algorithm to enhance computation speed.

This section is organized as follows. In the following subsection I explain the mathematical background of the spacetime volume sensitivity $\langle VT \rangle$ in terms of likelihood, mainly revisiting Ref. [181]. Then I outline machine learning method that includes data preparation, model building, and performance results. Finally, I discuss the characteristics and limitations of my DNN models and suggest potential applications for future work.

2.2.2 Deep Neural Network(DNN)

Machine learning is a category of computer algorithms that allow a machine to develop independently, solving a specific task without explicit human instruction. For instance, support vector machine (SVM) and k-nearest neighbors (KNN) algorithms are machine learning examples inspired by linear algebra. Artificial neural networks (ANN) exemplify machine learning inspired by the emulation of biological neuron cells. A simple ANN model comprises three layers: the input layer, the hidden layer, and the output layer. Each cell in the hidden layer is an operational unit that receives input parameters from the input layer and delivers the operation output to the output layer. The first successful implementation of ANN was by Frank Rosenblatt in 1957 [182]. Although the ANN concept is long-established, the development of computer hardware, particularly GPUs, has facilitated a rapid ascent of deep learning since 2009. Deep neural networks (DNN) typically refer to neural networks with multiple hidden layers.

In machine learning, algorithms are represented by a model with a parameter set, and a training scheme guides the model to find the optimal parameter set to solve the task. The DNN parameters are weights w_{ijk} and thresholds σ_{ij} . Let y_{ij} denote the state of each cell in the DNN where i indicates the i -th layer and j indicates the j -th cell in the layer. It is determined by the equation,

$$y_{ij} = f\left(\sum_k w_{ijk}y_{(i-1)k} - \sigma_{ij}\right), \quad (2.1)$$

where f is an activation function. Although a sigmoid function is used as the activation function in a traditional ANN. However, sigmoid function often causes a problem with the training process due to the vanishing gradient problem that I will discuss later. Rectified linear unit (ReLU) is a popular activation function in DNN because it does not suffer from the vanishing gradient problem. The ReLU function is defined as

$$f(x) = \max(0, x). \quad (2.2)$$

The most common way to train an ML model is through gradient-based optimization method such as Stochastic Gradient Descent (SGD) method, which updates parameters according to the gradient of the loss function. The loss function is a real number measure of the difference between

the model output and the ground truth value. The training method first calculate the error values of celled in the output layer. Then, the contribution to the error of each cell in the previous layer is determined by the derivative of the activation function, and the errors are distributed to them. This process repeats until every cell in the model is attributed some error values by reaching the initial layer. This process is called error backpropagation. The SGD method updates weights and thresholds according to these error values. This entire process constitutes one epoch and is repeated until the averaged error of the model converges to a minimum point. Because the derivative sigmoid function is mostly zero except near zero, error values are multiplied by zeros while backpropagating through the layers. This means the learning procedure unable to reduce the final error in DNN because parameters in the front layers are not updated. On the other hand, the derivative of ReLU is a step or sigmoidal function, which maintains non-vanishing errors during backpropagation. There are several programming libraries for machine learning, such as *TensorFlow* [183] and *PyTorch* [184]. In this project, I used *TensorFlow* to implement my ML models.

2.2.3 Spacetime-Volume Sensitivity $\langle VT \rangle$

The averaged spacetime volume sensitivity $\langle VT \rangle$ for a specific astrophysical event is expressed by

$$\langle VT \rangle = T \int dz d\theta \frac{dV_c}{dz} \frac{1}{1+z} \text{Pr}(\theta) f(z, \theta), \quad (2.3)$$

where T is the time duration of the observation, z is the redshift factor, V_c is the comoving volume, $\text{Pr}(\theta)$ is the probability distribution of the event with source-parameters θ , and the astrophysical distribution $f(z, \theta)$ is a selection function that estimates how likely it is to detect sources of z and θ . For example, one might have $\theta = \{m_1, m_2\}$ for a population model describing the distribution of binary component masses m_1 and m_2 . Injections are sampling points of Monte-Carlo methods of the above integration. Denote the total number of injections N_{inj} and the total spacetime volume of injection range $\langle VT \rangle^{\text{inj}}$. The spacetime volume sensitivity is expressed as

$$\langle VT \rangle = \frac{N_{\text{rec}}}{N_{\text{inj}}} \langle VT \rangle^{\text{inj}}, \quad (2.4)$$

where N_{rec} is the number of injections were detected (recovered) by the pipeline. One way to get the N_{rec} value is imposing a explicit threshold on the Bayes factor of the injections. However, there is a problem of ambiguity in which hard cut value to choose. Since N_{rec} is used to calculate the actual signal rates, N_{rec} needs to be calculated in a statistical way by using the list of real event triggers produced during the search. Define the rate of gravitational wave triggers by Λ_α , where Λ_0 is the expectation counts of terrestrial events and $\alpha=1,2$, and 3 corresponding to BBH, BNS, and NSBH respectively. First, calculate Λ_α from the real triggers. Let $\{\gamma_i\}$ is a set of injections. Consider the situation that one of an injection γ_i is added to the set of real triggers, then Λ_α value will be change because of the new trigger γ_i . Let $\Delta\Lambda_\alpha(\gamma_i)$ be the difference. After some algebra it is given by

$$\Delta\Lambda_\alpha(\gamma_i) = \frac{\text{cov}_N(\Lambda_0, \Lambda_\alpha) + \sum_\beta \text{cov}_N(\Lambda_\alpha, \Lambda_\beta) K_\beta(\gamma_i)}{\langle\Lambda_0\rangle_N + \sum_\beta K_\beta(\gamma_i) \langle\Lambda_\beta\rangle_N}, \quad (2.5)$$

where $K_\beta(\gamma_i)$ is the Bayes factor of γ_i in the astrophysical category β . Since Λ_α is the expectation number of events during the search, increasing of its value means increasement of the expectation value of N_{rec} . Repeat this argument over all injections, then the final N_{rec} is given by the summation over $\Delta\Lambda_\alpha(\gamma_i)$,

$$N_{\text{rec}} = \sum_i \Delta\Lambda(\gamma_i) = \sum_i \sum_{\alpha=1,2,3} \Delta\Lambda_\alpha(\gamma_i). \quad (2.6)$$

This relation shows that calculating $\Delta\Lambda_\alpha$ for every injection is equivalent to calculating the $\langle VT \rangle$.

2.2.4 Methods and Results

Data Preparation and Model Building

Injections during O1 and O2 before Virgo joined on Aug 1st, 2017 were used in this project. There are several classes of injections listed in Table 2.1 below. Only the injections from the broad class were used in training the ML models. In the broad class, injections are uniformly distributed in distance. There are three ML models corresponding to the three broad classes: BBH, BNS, and NSBH. Each models were trained on randomly picked 80% of the corresponding broad injections. They were tested on the remaining 20% of broad injections and also tested on injections in other classes: the astrophysical and peak distribution classes.

Table 2.1: Classes of the injections. Broad injections are uniformly distributed in distance. Astrophysical injections are uniformly distributed in spacetime volume which implies that $f(z, \theta)$ is increasing with redshift z . Peak distribution injections are using Dirac delta function for a distribution. The astrophysical and peak distribution injections are not used in training the ML models but only used in testing the models.

Class Type	BBH	BNS	NSBH
Broad (including training set)	bbh-broad-aligned bbh-broad-isotropic	bns-broad	nsbh-broad
Astrophysical or peak distribution	bbh-astrophysical-imf	bns-astrophysical	nsbh-delta-1p4-10-aligned nsbh-delta-1p4-10-isotropic

Each injection has several injected parameters. For deep learning I use M_{chirp} , η , χ_{eff} , $\log d_H$, $\log d_L$, z , and t_{GPS} . The first three of them are the chirp mass, symmetric mass ratio, and effective spin parameter respectively defined as

$$M_{\text{chirp}} = \frac{(m_1 m_2)^{3/5}}{(m_1 + m_2)^{1/5}}, \quad \eta = \frac{m_1 m_2}{(m_1 + m_2)^2}, \quad \chi_{\text{eff}} = \frac{m_1 \chi_1 + m_2 \chi_2}{m_1 + m_2}, \quad (2.7)$$

where $m_{1,2}$ are the masses and $\chi_{1,2}$ are the spin parameters of the two compact objects, $\log d_{H,L}$ are the log effective distances from the source to each detector sites Hanford and Livingston, z is the redshift, and t_{GPS} is the GPS time of the injection. The GPS time is required to capture the time evolution of the detector sensitivity. Each parameter is batch normalized to have zero mean and unit variance before feeding into the ML model. The true values of $\Delta\Lambda$ were calculated using the *pAstro* package[181].

The ML models used in this research have a 5-layer architecture which includes the input and output layers. The input layer has 7 nodes corresponding to the input parameters mentioned above. The output layer has a single node that represents the estimated $\Delta\Lambda$ value. Each of the three hidden layers has 64 nodes. Each model was trained for 10 epochs. Additionally, hyperparameter tuning was conducted by testing a variety of model depths, ranging from 1 to 12 hidden layers. It concludes that the 5-layer model was identified as the optimal model for both performance and model size. All models were trained on a single M1 CPU. The training process took approximately 3 minutes, processing a dataset with injection numbers on the order of 10^4 . The ML models were implemented using the *TensorFlow* [183] library.

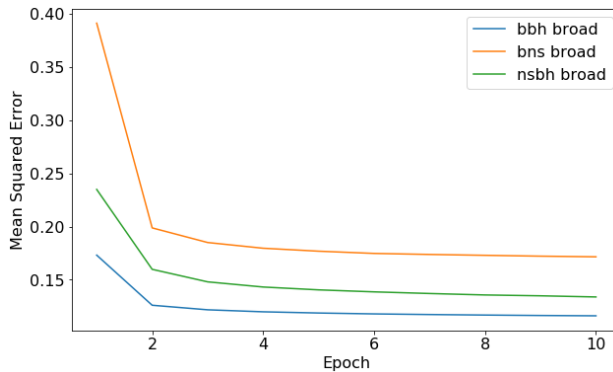


Figure 2-1: Error curves of ML models.

Table 2.2: Results of ML models.

Class Type	Training	N_{inj}	$N_{\text{rec}}^{\text{pAstro}}$	$N_{\text{rec}}^{\text{ML}}$	Error(%)
BBH broad test	BBH broad training	16824	13645.8	13545.7	-0.73
BBH astrophysical imf		40455	32203.0	32077.5	-0.39
BNS broad test	BNS broad training	6813	5518.5	5576.0	1.04
BNS astrophysical		34439	28935.5	28789.3	-0.51
NSBH broad test	NSBH broad training	8316	5966.0	6011.8	0.77
NSBH delta 1p4 10 aligned		36414	25510.6	25241.9	-1.05
NSBH delta 1p4 10 isotropic		29688	19484.6	21096.2	8.27

ML Model Performances

The error curves during the learning process are shown in Fig. 2-1. Although increasing the maximum epoch beyond 10 could potentially decrease the error further, it occasionally leads to greater error in N_{rec} due to overfitting. The N_{rec} values calculated from *pAstro* and estimated by ML models are presented in Table 2.2. More detailed error plots of each ML models for BBH injection set are presented in Fig. 2-2 and other remaining injection sets are presented in Appendix A.1.

2.2.5 Discussion

My machine learning models demonstrated correct results with observed errors under 10%. Notably, these errors are within acceptable bounds, staying below the inherent error scale of the $\langle VT \rangle$ measurements [176]. This establishes that employing machine learning to infer $\langle VT \rangle$ can offer computational cost-efficiency.

However, one should note that overfitting the model can result a significant increase of errors for other injection class. This problem can be observed when the model is trained for a large number of

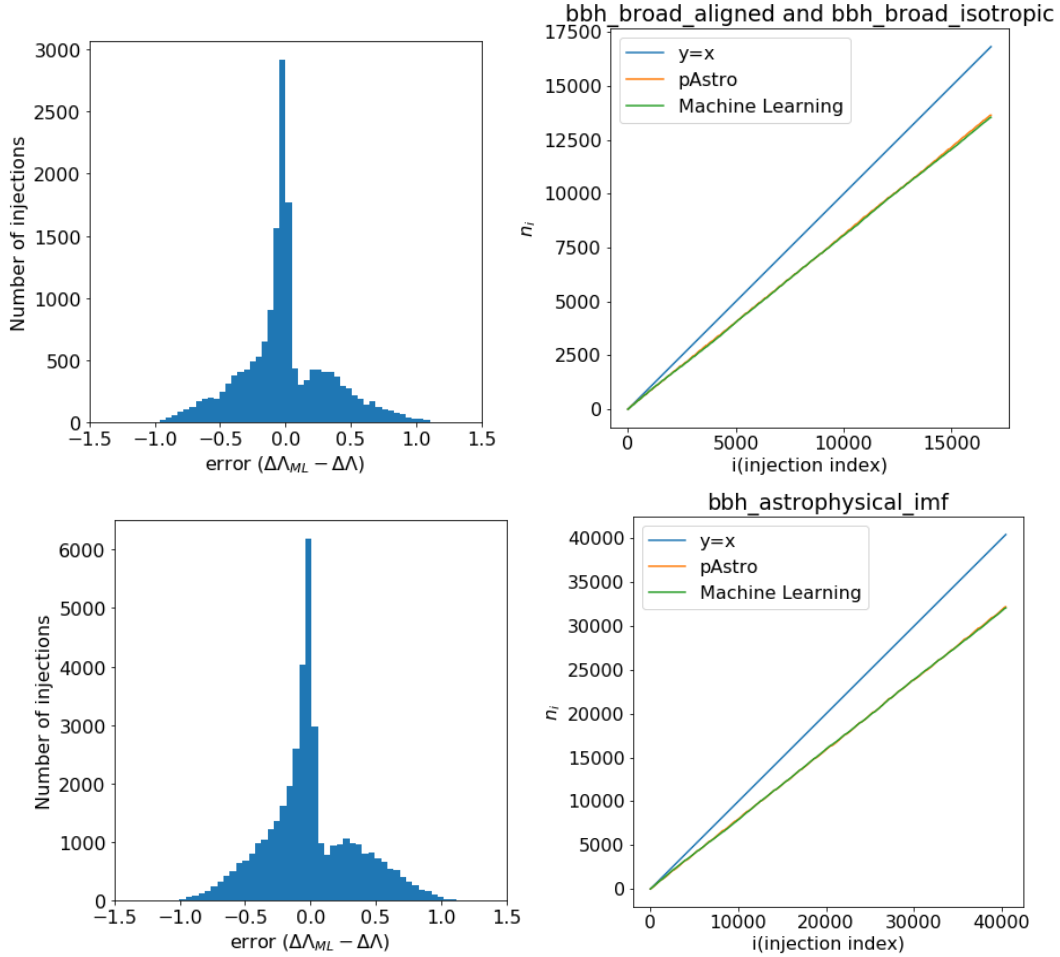


Figure 2-2: Performance of ML models for BBH injections

epochs, for example, training the model with BNS broad injections over 50 epochs and then testing it on BNS astrophysical injections led to an error of -4.64% , a magnitude higher than in prior test.

One of the advantages of the current approach is that our ML models were trained on the broad injection set. This set is typically the primary and the first serving set used during the injection campaign. Hence, once a campaign finish the broad set analysis, the trained ML models are immediately available for application in testing other population distributions, even before the other astrophysical distributions have yet to be done by the actual pipeline campaign.

Unfortunately, the ML models were not utilized for the last O3 data analysis [179], due to their lack of robustness in dealing with far distance injections. To illustrate more details, if the broad set has an injection distance range that maxes out at 100 Mpc, the ML models would not be able to estimate the $\langle VT \rangle$ for the astrophysical set with an injection distance range that reaches up

to 500 Mpc. This highlights an area for improvement if ML models are used in future O4 data analysis. Achieving robustness for far distance injections and enabling the models to extrapolate their estimations to include these far distance injections are key for this applicability.

2.3 Dark Matter Evidence in Blip Glitches

2.3.1 Introduction

LIGO and Virgo have been observing transient like signals called glitches through every observing runs O1, O2, O3a, and O3b [185, 186]. Glitches are non-Gaussian, loud, and short in duration, thus it may often triggers the detection pipeline. The challenge lies in distinguishing high mass binary black hole (BBH) mergers and burst-type signals from these glitches, especially given that glitches do not originate from astrophysical sources, as evidenced by their lack of correlation across the multiple interferometers. The causes of many glitches remain unknown.

The collaborations have been developing a glitch classification pipeline called Gravity Spy. This citizen science project involves human volunteers categorizing glitches based on their visual attributes. The data accumulated from this human classification are then utilized to train a machine learning model, which is applied to actual strain data to categorize glitches. A more detailed description and updates on the Gravity Spy project can be found in Ref. [186, 187].

After the classification, the collaborations have been investigating the origin of glitches. Numerous types of glitches have been identified, some of which are correlated with environmental factors. For instance, during O3b, researchers found a strong correlation between the occurrence of slow scattering arches and the relative motion between the end test mass chain and the reaction-mass chain of the optic suspension system [178]. The rate of these glitches decreased following the implementation of reaction-chain tracking in Hanford. The collaborations also regularly analyze the correlation between glitches and environmental factors, such as seismic noise, weather, and human activity. However, there remain some glitches, such as the blip glitches, whose physical causes and potential correlation with environmental factors are proven to be uncorrelated [188].

In this section, I introduce a hypothesis that decaying dark matter particles generating grav-

itational waves could be a potential source of blip glitches. In subsection 2.3.2, I will introduce the conceptual picture of this hypothesis and share the results of an analysis showing blip glitch rates statistics across all detectors and observing runs. In subsection 2.3.3, I will introduce the Gabor-Morlet wavelet as the blip glitch waveform model. In subsection 2.3.4, I will present a list of dark matter particle results deduced by dimensional analysis. In 2.3.5, I will introduce Bayesian analysis for this problem. Finally in section 2.3.6, I will discuss these results and future work.

2.3.2 Dark matter decay and blip glitch rates

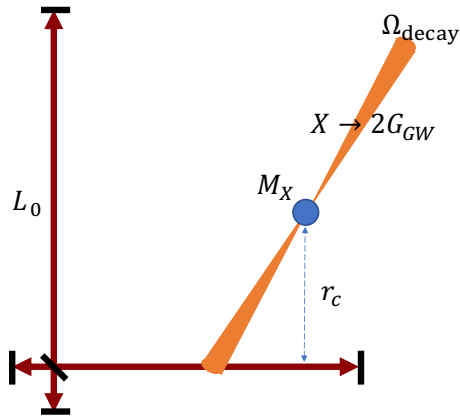


Figure 2-3: A diagram of a dark matter particle X with mass M_X decaying into two gravitons in the limit of cone-shaped classical gravitational waves.

Assume a hypothetical dark matter particle X at rest with rest mass M_X decays into two gravitons in two opposite directions as shown in Fig. ???. The decay process is assumed to be a quantum gravity process. Because G , c , \hbar , and M_X are all the physical parameters involved in this microscopic process, the order of magnitude calculation of the decay rate is given by

$$\Gamma_{X \rightarrow \text{GW}} \sim \left(\frac{M_X}{M_P} \right)^n \frac{1}{T_P}, \quad (2.8)$$

where $\Gamma_{X \rightarrow \text{GW}}$ is the gravitational decay rate of particle X , M_P is the Planck mass, T_P is the Planck time, and n is a number given by a microscopic theory which remains uncertain linked to a quantum gravity theory. After decay process let two gravitons quickly falls into the limit of classical gravitational wave propagating in narrow cone shape with steradian angle Ω_{decay} . Assume

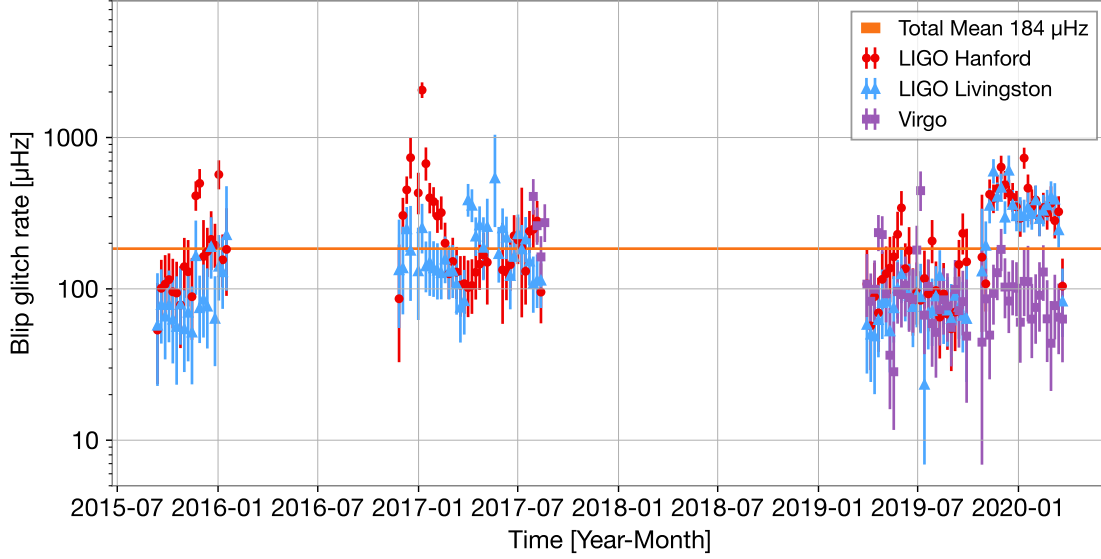


Figure 2-4: Rate of Blip Glitches(Weekly Statistics, ML confidence ≥ 0.99)

a blip glitch is detected when a decay event occurred near the interferometer and gravitational wave direction is oriented to intersect with the interferometer's laser beam line. The order of the glitch rate is given by

$$\Gamma_{\text{glitches}} \sim \frac{\rho_{\text{DM}} V_{\text{LIGO}}}{M_X} \frac{\Omega_{\text{decay}}}{4\pi} \Gamma_{X \rightarrow \text{GW}}, \quad (2.9)$$

where ρ_{DM} is dark matter density, V_{LIGO} is effective volume of the LIGO instruments, and Ω_{decay} is solid angle of decaying gravitational wave. The blip glitch rate Γ_{glitches} is experimentally measured by the number of blip glitch triggers divided by the observation time. The blip glitch rate calculated for all observing runs and each detector sites is shown in Fig. 2-4.

2.3.3 Gabor-Morlet Wavelet Model

To model the blip glitches, Gabor-Morlet wavelet is used here, because a blip glitch is a Gaussian modulated sinusoidal wave by its naming. The specific waveform is given by

$$u(t; \boldsymbol{\theta}) = A(e_0, \sigma_0, f_0) e^{-\frac{(t-t_0)^2}{4\sigma_0^2}} \cos(2\pi f_0(t-t_0) - \phi_0), \quad (2.10)$$

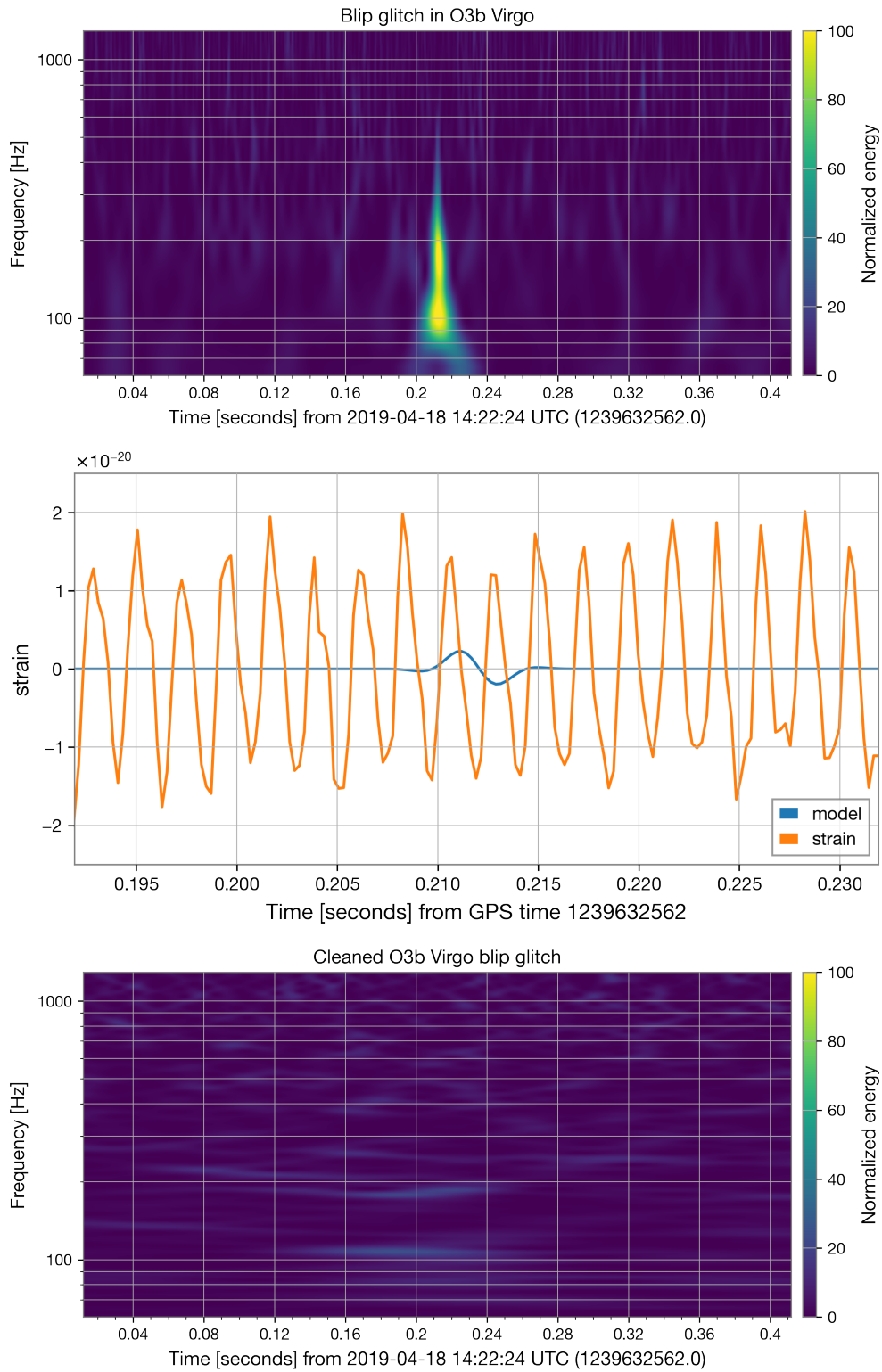


Figure 2-5: Representative blip glitch in O3b Virgo and cleaned q-scan by Gabor-Morlet wavelet. Cleaning is done by the wavelet model Eq. 2.10. Parameters are given as follows: $A = -2.77 \times 10^{-21}$, $f_0 = 213\text{Hz}$, $\sigma_0 = 1.00\text{ms}$, and $\phi_0 = 1.78$

where the amplitude A is an amplitude function of the energy flux e_0 , the width σ_0 , and the frequency f_0 . The energy flux is given by

$$A(e_0, \sigma_0, f_0) = \sqrt{\frac{e_0}{\sigma_0 f_0^2 + (16\pi^2 \sigma_0)^{-1}}} , \quad (2.11)$$

which normalizes the energy flux relation, that is

$$\frac{dE}{dS} = \frac{1}{16\pi} \int_{-\infty}^{\infty} dt (\dot{u}_+^2 + \dot{u}_\times^2) \sim e_0 . \quad (2.12)$$

The waveform parameter consists of five real numbers:

$$\boldsymbol{\theta} = (f_0, \sigma_0, e_0, t_0, \phi_0) . \quad (2.13)$$

As shown in Fig. 2-5, the wavelet model nicely subtract the blip glitches by minimizing the normalized energy flux.

2.3.4 Dark matter parameters estimation

The effective volume of the LIGO instruments V_{LIGO} yields two approximation given by

$$V_{\text{LIGO}} \approx \begin{cases} 2L_0(\pi r_c^2) & , r_c < L_0 \\ 4\pi r_c^3/3 & , \text{otherwise} \end{cases} \quad (2.14)$$

where $L_0 = 4\text{km}$ is the arm length of the interferometer arm length and r_c is a critical radius. Here, assume that $r_c < L_0$ and V_{LIGO} has two cylindrical geometry wrapped around each laser arm with radius r_c . Another limit $r_c \geq L_0$ can also be considered, but it does not give a different dimensional result unless r_c is extremely greater than L_0 . When the energy flux of the gravitational wave is assumed to be e_0 , which can be obtained by Eq. 2.11, then the total energy of the gravitational wave is given by

$$M_X c^2 \sim 2e_0 \Omega_{\text{decay}} r_c^2 , \quad (2.15)$$

where the factor of two represents another gravitational wave packet propagating in the opposite direction. These r_c dependencies are canceled out in the blip glitch rate relation. Recall the rates equation, the blip glitch rate Eq. 2.8 and the dark matter decay rate Eq. 2.9, they are given by

$$\Gamma_{X \rightarrow \text{GW}} \sim \left(\frac{M_X}{M_P} \right)^n \frac{1}{T_P}, \quad \Gamma_{\text{glitches}} \sim \frac{\rho_{\text{DM}} V_{\text{LIGO}} \Omega_{\text{decay}}}{M_X} \frac{1}{4\pi} \Gamma_{X \rightarrow \text{GW}}, \quad (2.16)$$

It is useful to introduce a characteristic mass scale

$$M_c \sim \frac{\rho_{\text{DM}} c^2 V_{\text{LIGO}} \Omega_{\text{decay}}}{\Gamma_{\text{glitches}} T_P} \frac{1}{4\pi} \sim \frac{\rho_{\text{DM}} c^2}{\Gamma_{\text{glitches}} T_P} \frac{L_0}{2e_0}, \quad (2.17)$$

which yields the relation

$$\left(\frac{M_P}{M_X} \right)^n \sim \frac{1}{T_P \Gamma_{X \rightarrow \text{GW}}} \sim \frac{M_c}{M_X}. \quad (2.18)$$

Hence, the quantum gravity microscopic parameter n is given by

$$n \approx \frac{\log(M_c/M_X)}{\log(M_P/M_X)}. \quad (2.19)$$

To deduce unknown parameters, it is imperative to clarify the input parameters. As in the previous subsection, the q-scan parameter estimation (PE) result provides values for $|A|$, f_0 , σ_0 , and ϕ_0 corresponding to the representative blip glitch. The energy flux e_0 is determined by Eq. 2.11. The particle mass M_X is inferred from the internal frequency f_0 . This is because similar in many other microscopic decaying processes the internal characteristic frequency of wave packet is given by the mass of the source particle due to the energy quantization of the wave packets as a particle. Local dark matter density in the solar system $\rho_{\text{DM}} = 6.1 \times 10^{-22} \text{kg/m}^3 (= 0.009 M_{\odot} \text{pc}^{-3})$ is taken from Ref. [189, 190]. Now I can calculate the dark matter decay rate $\Gamma_{X \rightarrow \text{GW}}$ and the quantum gravity parameter n using the given parameters. The results are shown in Table 2.3. The dark matter particle mass is given by $M_X = 8.8 \times 10^{-13} \text{eV}/c^2$, which falls into the light dark matter mass region. Since $n \approx 1.28$ is obtained by the log ratio between extreme magnitude numbers, n is fine-tuned number and immune to the uncertainty of M_X . Note that $\Gamma_{X \rightarrow \text{GW}} T_{\text{universe}} \gg 1$, which casts doubt on the validity of the assumption that the dark matter particle is stable. However,

Table 2.3: List of dark matter parameters

Parameter	Quantity	Method or Equation
$ A $	2.8×10^{-21}	Q-scan PE
f_0	210 Hz	Q-scan PE
σ_0	1.0 ms	Q-scan PE
ϕ_0	1.8 rad	Q-scan PE
e_0	2.0×10^{13} eV/m ²	$\frac{c^3}{16\pi G} A^2 (\sigma_0 f_0^2 + 1/(16\pi^2 \sigma_0))$
M_X	8.8×10^{-13} eV/c ²	$h f_0 / c^2$
$\Omega_{\text{decay}} r_c^2$	2.2×10^{-26} m ²	$M_X c^2 / (2e_0)$
ρ_{DM}	3.4×10^{14} eV/c ² /m ³	Ref. [189, 190]
Γ_{glitch}	1.8×10^{-4} Hz	Fig. 2-4
V_{LIGO}/r_c^2	8 π km	Eq. 2.14
M_c	1.5×10^{39} eV/c ²	Eq. 2.17
n	1.28	Eq. 2.19
$1/T_{\text{universe}}$	2.2×10^{-18} Hz	Inverse Hubble time
$1/T_P$	1.8549×10^{43} Hz	Inverse Planck time
M_P	1.2209×10^{28} eV/c ²	Planck mass
$\Gamma_{X \rightarrow \text{GW}}$	1.1×10^{-8} Hz	$M_X / (M_c T_P)$

this assumption is not necessary for the hypothesis to be valid. The hypothetical particle X can be intermediate dark matter particles in the decay process but not the original source of the mass energy.

2.3.5 Bayesian statistics

The PSD weighted inner product is given by

$$(d, u) = 2 \int_{-\infty}^{\infty} df \frac{\tilde{d}(f) \tilde{u}^*(f)}{S_{\text{PSD}}(|f|)}, \quad (2.20)$$

where $S_{\text{PSD}}(f)$ encodes the detector background noise information. The analytic form of the waveform in the frequency domain is useful to reduce the numerical error when calculating inner product, that is

$$\tilde{u}(f) = \sqrt{\pi} A \sigma e^{-i(2\pi f t_0)} (e^{-4\pi^2 \sigma^2 (f-f_0)^2} e^{-i\phi_0} + e^{-4\pi^2 \sigma^2 (f+f_0)^2} e^{i\phi_0}). \quad (2.21)$$

In order to calculate the likelihood of the hypothesis, I need to calculate the inner product between the data and the model. The likelihood is given by

$$\mathcal{L}(\mathcal{H}_\theta) = \frac{\Pr(\text{data}|\mathcal{H}_\theta)}{\Pr(\text{data}|\mathcal{H}_{\text{null}})} = \frac{e^{-(s-h_\theta, s-h_\theta)/2}}{e^{-(s,s)/2}} = e^{(s, h_\theta) - (h_\theta, h_\theta)/2}, \quad (2.22)$$

where s is the strain data, h_θ is the model waveform, \mathcal{H}_θ is the hypothesis to test, and $\mathcal{H}_{\text{null}}$ null hypothesis. To perform Bayesian inference, I need to calculate the posterior probability of the hypothesis. The posterior probability is given by

$$\Pr(\mathcal{H}_\theta|\text{data}) = \frac{\Pr(\text{data}|\mathcal{H}_\theta) \Pr(\mathcal{H}_\theta)}{\Pr(\text{data})}, \quad (2.23)$$

where $\Pr(\text{data}|\mathcal{H}_\theta)$ is the likelihood, $\Pr(\mathcal{H}_\theta)$ is the prior probability, and $\Pr(\text{data})$ is the evidence. The evidence is given by

$$\Pr(\text{data}) = \int d\theta \Pr(\text{data}|\mathcal{H}_\theta) \Pr(\mathcal{H}_\theta). \quad (2.24)$$

The posterior probability is used to calculate the Bayes factor. The Bayes factor is given by

$$\mathcal{B} = \frac{\Pr(\mathcal{H}_\theta|\text{data})}{\Pr(\mathcal{H}_{\text{null}}|\text{data})}. \quad (2.25)$$

The Bayes factor is used to test the hypothesis. The hypothesis is accepted when the Bayes factor is greater than 1. The hypothesis is rejected when the Bayes factor is less than 1. The Bayes factor is used to calculate the probability of the hypothesis given by

$$\Pr(\mathcal{H}_\theta|\text{data}) = \frac{\mathcal{B}}{1 + \mathcal{B}}, \quad \Pr(\mathcal{H}_{\text{null}}|\text{data}) = \frac{1}{1 + \mathcal{B}}. \quad (2.26)$$

2.3.6 Discussion

I tested the hypothesis that dark matter particles decaying into gravitational waves can be a source of blip glitches with dimensional analysis and wavelet modeling. Glitch rate is given by $184\mu\text{Hz}$. The mass of the dark matter particle is estimated by the model parameter $f_0 = 210\text{Hz}$ which is corresponding to the dark matter particle mass of $10^{-12}\text{eV}/c^2$ and $n = 1.28$, where these

parameters may give a rope to the quantum gravity theory and dark matter model. However, the microscopic decay model need to be improved with intermediate particles, because current model is not consistent with the assumption that the dark matter particle is stable, that is $\Gamma_{X \rightarrow \text{GW}} T_{\text{universe}} \gg 1$.

Since this analysis was based on a single representative blip glitch trigger, a complete statistical analysis are needed to draw a conclusion. There are two steps to be conducted in the future. First, more precise analysis can be done by using all blip glitches as a population in all observing runs. Second, the statistical analysis introduced in 2.3.5 need to be conducted to test the hypothesis instead of using exact values of the parameters. One of the challenging point is that Bayesian analysis requires the inner product calculation between the data and the model on parameter space grid points, which is computationally intensive. By employing Bayesian statistics, the validity of my hypothesis can be further assessed by comparing the likelihood of this hypothesis against the likelihood of the null hypothesis.

Bibliography

- [1] H. G. Suh, H. Menke, P. M. R. Brydon, C. Timm, A. Ramires, and D. F. Agterberg, *Stabilizing even-parity chiral superconductivity in Sr_2RuO_4* , Phys. Rev. Res. **2**, 032023 (2020), <https://link.aps.org/doi/10.1103/PhysRevResearch.2.032023>.
- [2] T. Shishidou, H. G. Suh, P. M. R. Brydon, M. Weinert, and D. F. Agterberg, *Topological band and superconductivity in UTe_2* , Phys. Rev. B **103**, 104504 (2021), <https://link.aps.org/doi/10.1103/PhysRevB.103.104504>.
- [3] H. G. Suh, Y. Yu, T. Shishidou, M. Weinert, P. M. R. Brydon, and D. F. Agterberg, *Superconductivity of anomalous pseudospin* (2023), 2301.11458.
- [4] K. Ishida, H. Mukuda, Y. Kitaoka, K. Asayama, Z. Q. Mao, Y. Mori, and Y. Maeno, *Spin-triplet superconductivity in Sr_2RuO_4 identified by ^{17}O knight shift*, Nature **396**, 658 (1998).
- [5] J. A. Duffy, S. M. Hayden, Y. Maeno, Z. Mao, J. Kulda, and G. J. McIntyre, *Polarized-neutron scattering study of the cooper-pair moment in Sr_2RuO_4* , Phys. Rev. Lett. **85**, 5412 (2000).
- [6] G. M. Luke, Y. Fudamoto, K. M. Kojima, M. I. Larkin, J. Merrin, B. Nachumi, Y. J. Uemura, Y. Maeno, Z. Q. Mao, Y. Mori, H. Nakamura, and M. Sgrist, *Time-reversal symmetry breaking superconductivity in Sr_2RuO_4* , Nature **394**, 558 (1998).
- [7] J. Xia, Y. Maeno, P. T. Beyersdorf, M. M. Fejer, and A. Kapitulnik, *High resolution polar kerr effect measurements in Sr_2RuO_4 : Evidence for broken time-reversal symmetry in the superconducting state*, Phys. Rev. Lett. **97**, 167002 (2006).
- [8] Y. Maeno, H. Hashimoto, K. Yoshida, S. Nishizaki, T. Fujita, J. G. Bednorz, and F. Lichtenberg, *Superconductivity in a layered perovskite without copper*, Nature **372**, 532 (1994).
- [9] T. M. Rice and M. Sgrist, *Sr_2RuO_4 : an electronic analogue of ^3He ?*, J. Phys.: Condens. Matter **7**, L643 (1995).
- [10] I. I. Mazin and D. J. Singh, *Competitions in layered ruthenates: ferromagnetism versus antiferromagnetism and triplet versus singlet pairing*, Phys. Rev. Lett. **82**, 4324 (1999).
- [11] K. Miyake and O. Narikiyo, *Model for unconventional superconductivity of Sr_2RuO_4 : Effect of impurity scattering on time-reversal breaking triplet pairing with a tiny gap*, Phys. Rev. Lett. **83**, 1423 (1999).
- [12] T. Kuwabara and M. Ogata, *Spin-triplet superconductivity due to antiferromagnetic spin-fluctuation in Sr_2RuO_4* , Phys. Rev. Lett. **85**, 4586 (2000).

- [13] M. Sato and M. Kohmoto, *Mechanism of spin-triplet superconductivity in sr_2ruo_4* , J. Phys. Soc. Jpn. **69**, 3505 (2000).
- [14] T. Takimoto, *Orbital fluctuation-induced triplet superconductivity: mechanism of superconductivity in sr_2ruo_4* , Phys. Rev. B **62**, 14641 (2000).
- [15] T. Nomura and K. Yamada, *Roles of electron correlations in the spin-triplet superconductivity of sr_2ruo_4* , J. Phys. Soc. Jpn. **71**, 1993 (2002).
- [16] Y. Yanase and M. Ogata, *Microscopic identification of the d-vector in triplet superconductor sr_2ruo_4* , J. Phys. Soc. Jpn. **72**, 673 (2003).
- [17] J. F. Annett, G. Litak, B. L. Gyorffy, and K. I. Wysokinski, *Spin-orbit coupling and symmetry of the order parameter in strontium ruthenate*, Phys. Rev. B **73**, 134501 (2006).
- [18] Y. Yoshioka and K. Miyake, *Pairing mechanism and anisotropy of d-vector of spin-triplet superconductor sr_2ruo_4* , J. Phys. Soc. Jpn. **78**, 074701 (2009).
- [19] S. Raghu, A. Kapitulnik, and S. Kivelson, *Hidden quasi-one-dimensional superconductivity in sr_2ruo_4* , Phys. Rev. Lett. **105**, 136401 (2010).
- [20] Q. H. Wang, C. Platt, Y. Yang, C. Honerkamp, F. C. Zhang, W. Hanke, T. M. Rice, and R. Thomale, *Theory of superconductivity in a three-orbital model of sr_2ruo_4* , Europhys. Lett. **104**, 17013 (2013).
- [21] J.-W. Huo, T. M. Rice, and F. C. Zhang, *Spin density wave fluctuations and p-wave pairing in sr_2ruo_4* , Phys. Rev. Lett. **110**, 167003 (2013).
- [22] T. Scaffidi, J. C. Romers, and S. H. Simon, *Pairing symmetry and dominant band in sr_2ruo_4* , Phys. Rev. B **89**, 220510(R) (2014).
- [23] M. Tsuchiizu, Y. Yamakawa, S. Onari, Y. Ohno, and H. Kontani, *Spin-triplet superconductivity in sr_2ruo_4 due to orbital and spin fluctuations: analyses by two-dimensional renormalization group theory and self-consistent vertex-correction method*, Phys. Rev. B **91**, 155103 (2015).
- [24] A. P. Mackenzie, T. Scaffidi, C. W. Hicks, and Y. Maeno, *Even odder after twenty-three years: the superconducting order parameter puzzle of sr_2ruo_4* , njp Quantum Materials **2**, 40 (2017).
- [25] J. R. Kirtley, C. Kallin, C. W. Hicks, E.-A. Kim, Y. Liu, K. A. Moler, Y. Maeno, and K. D. Nelson, *Upper limit on spontaneous supercurrents in sr_2ruo_4* , Phys. Rev. B **76**, 014526 (2007).
- [26] C. Lupien, W. A. MacFarlane, C. Proust, L. Taillefer, Z. Q. Mao, and Y. Maeno, *Ultrasound attenuation in sr_2ruo_4 : An angle-resolved study of the superconducting gap function*, Phys. Rev. Lett. **86**, 5986 (2001).
- [27] E. Hassinger, P. Bourgeois-Hope, H. Taniguchi, S. R. de Cotret, G. Grissonnanche, M. S. Anwar, N. Doiron-Leyraud, and L. Taillefer, *Vertical line nodes in the superconducting gap structure of sr_2ruo_4* , Phys. Rev. X **7**, 011032 (2017).
- [28] S. Kittaki, S. Nakamura, T. Sakakibara, N. Kikugawa, T. Terashima, S. Uji, D. Sokolov, A. P. Mackenzie, K. Irie, Y. Tsutsumi, K. Suzuki, and K. Machida, *Searching for gap zeros in sr_2ruo_4 via field-angle-dependent specific-heat measurement*, J. Phys. Soc. Jpn. **87**, 093703 (2018).

- [29] S. Kittaka, A. Kasahara, T. Sakakibara, D. Shibata, S. Yonezawa, Y. Maeno, K. Tenya, and K. Machida, *Sharp magnetization jump at the first-order superconducting transition in sr_2ruo_4* , Phys. Rev. B **90**, 220502 (2014).
- [30] C. W. Hicks, D. O. Brodsky, E. A. Yeland, A. S. Gibbs, J. A. N. Bruin, M. E. Barber, S. D. Edkins, K. Nishimura, S. Yonezawa, Y. Maeno, and A. P. Mackenzie, *Strong increase in t_c of sr_2ruo_4 under both tensile and compressive strain*, Science **344**, 283 (2014).
- [31] A. Steppke, L. Zhao, M. E. Barber, T. Scaffidi, F. Jerzembeck, H. Rosner, A. S. Gibbs, Y. Maeno, S. H. Simon, A. P. Mackenzie, and C. W. Hicks, *Strong peak in t_c of sr_2ruo_4 under uniaxial pressure*, Science **355**, 9398 (2017).
- [32] C. Kallin and A. J. Berlinsky, *Is sr_2ruo_4 a chiral p -wave superconductor?*, J. Phys.: Condens. Matter **21**, 164210 (2009).
- [33] S. B. Etter, A. Bouhon, and M. Sigrist, *Spontaneous surface flux pattern in chiral p -wave superconductors*, Phys. Rev. B **97**, 064510 (2018).
- [34] A. Pustogow, Y. Luo, A. Chronister, Y. S. Su, D. A. Sokolov, F. Jerzembeck, A. P. Mackenzie, C. W. Hicks, N. Kikugawa, S. Raghu, E. D. Bauer, and S. E. Brown, *Constraints on the superconducting order parameter in sr_2ruo_4 from oxygen-17 nuclear magnetic resonance*, Nature **574**, 72 (2019).
- [35] K. Ishida, M. Manago, and Y. Maeno (2019), arXiv:1907.12236.
- [36] V. Grinenko, S. Ghosh, R. Sarkar, J.-C. Orain, A. Nikitin, M. Elender, D. Das, Z. Guguchia, F. Bruckner, M. E. Barber, J. Park, N. Kikugawa, D. A. Sokolov, J. S. Bobowski, T. Miyoshi, et al., *Split superconducting and time-reversal symmetry-breaking transitions, and magnetic order in sr_2ruo_4 under uniaxial stress*, arXiv:2001.08512 (2020).
- [37] S. Benhabib, C. Lupien, I. Paul, L. Berges, M. Dion, M. Nardone, A. Zitouni, Z. Mao, Y. Maeno, A. Georges, L. Taillefer, and C. Proust (2020), arXiv:2002.05916.
- [38] S. Ghosh, A. Shekhter, F. Jerzembeck, N. Kikugawa, D. Sokolov, M. Brando, A. P. Mackenzie, C. Hicks, and B. Ramshaw (2020), arXiv:2002.06130.
- [39] M. Sigrist and K. Ueda, *Phenomenological theory of unconventional superconductivity*, Rev. Mod. Phys. **63**, 239 (1991).
- [40] I. Žutić and I. I. Mazin, *Phase-sensitive tests of the pairing state symmetry in sr_2ruo_4* , Phys. Rev. Lett. **95**, 217004 (2005).
- [41] I. Schnell, I. I. Mazin, and A. Y. Liu, *Unconventional superconducting pairing symmetry induced by phonons*, Phys. Rev. B **74**, 184503 (2006).
- [42] H. S. Røising, T. Scaffidi, F. Flicker, G. F. Lange, and S. H. Simon, *Superconducting order of sr_2ruo_4 from a three-dimensional microscopic model*, Phys. Rev. Research **1**, 033108 (2019).
- [43] C. M. Puetter and H.-Y. Kee, *Identifying spin-triplet pairing in spin-orbit coupled multi-band superconductors*, EPL **98**, 27010 (2012).
- [44] J. Spalek, *Spin-triplet superconducting pairing due to local hund's rule and dirac exchange*, Phys. Rev. B **63**, 104513 (2001).

- [45] J. E. Han, *Spin-triplet s-wave local pairing induced by hund's rule coupling*, Phys. Rev. B **70**, 054513 (2004).
- [46] O. Vafek and A. V. Chubukov, *Hund interaction, spin-orbit coupling, and the mechanism of superconductivity in strongly hole-doped iron pnictides*, Phys. Rev. Lett. **118**, 087003 (2017).
- [47] A. K. C. Cheung and D. F. Agterberg, *Superconductivity in the presence of spin-orbit interactions stabilized by hund coupling*, Phys. Rev. B **99**, 024516 (2019).
- [48] A. W. Lindquist and H.-Y. Kee (2019), arXiv:1912.02215.
- [49] S. Hoshino and P. Werner, *Superconductivity from emerging magnetic moments*, Phys. Rev. Lett. **115**, 247001 (2015).
- [50] O. Gingras, R. Nourafkan, A.-M. S. Tremblay, and M. Côté, *Superconducting symmetries of sr_2ruo_4 from first-principles electronic structure*, Phys. Rev. Lett. **123**, 217005 (2019).
- [51] A. Tamai, M. Zingl, E. Rozbicki, E. Cappelli, S. Riccò, A. de la Torre, S. M. Walker, F. Y. Bruno, P. D. C. King, W. Meevasana, M. Shi, M. Radović, N. C. Plumb, A. S. Gibbs, A. P. Mackenzie, et al., *High-resolution photoemission on sr_2ruo_4 reveals correlation-enhanced effective spin-orbit coupling and dominantly local self-energies*, Phys. Rev. X **9**, 021048 (2019).
- [52] L. Fu and E. Berg, *Odd-parity topological superconductors: theory and application to $cu_xbi_2se_2$* , Phys. Rev. Lett. **105**, 097001 (2010).
- [53] S. Sasaki, M. Kriener, K. Segawa, K. Yada, Y. Tanaka, M. Sato, and Y. Ando, *Topological superconductivity in $cu_xbi_2se_3$* , Phys. Rev. Lett. **107**, 217001 (2011).
- [54] A. Yamakage, K. Yada, M. Sato, and Y. Tanaka, *Theory of tunneling conductance and surface-state transition in superconducting topological insulators*, Phys. Rev. B **85**, 180509 (2012).
- [55] A. Ramires and M. Sgrist, *Identifying detrimental effects for multi-orbital superconductivity: Application to sr_2ruo_4* , Phys. Rev. B **94**, 104501 (2016).
- [56] A. Ramires, D. F. Agterberg, and M. Sgrist, *Tailoring t_c by symmetry principles: The concept of superconducting fitness*, Phys. Rev. B **98**, 024501 (2018).
- [57] D. F. Agterberg, P. M. R. Brydon, and C. Timm, *Bogoliubov fermi surfaces in superconductors with broken time-reversal symmetry*, Phys. Rev. Lett. **118**, 127001 (2017).
- [58] P. M. R. Brydon, D. F. Agterberg, H. Menke, and C. Timm, *Bogoliubov fermi surfaces: general theory, magnetic order, and topology*, Phys. Rev. B **98**, 224509 (2018).
- [59] A. Ramires and M. Sgrist, *Superconducting order parameter of sr_2ruo_4 : A microscopic perspective*, Phys. Rev. B **100**, 104501 (2019).
- [60] C. N. Veenstra, Z.-H. Zhu, M. Raichle, B. M. Ludbrook, A. Nicolaou, B. Slomski, G. Landolt, S. Kittaka, Y. Maeno, J. H. Dil, I. S. Elfimov, M. W. Haverkort, and A. Damascelli, *Spin-orbital entanglement and the breakdown of singlets and triplets in sr_2ruo_4 revealed by spin- and angle-resolved photoemission spectroscopy*, Phys. Rev. Lett. **112**, 127002 (2014).
- [61] G. Zhang, E. Gorelov, E. Sarvestani, and E. Pavarini, *Fermi surface of sr_2ruo_4 : Spin-orbit and anisotropic coulomb interaction effects*, Phys. Rev. Lett. **116**, 106402 (2016).

- [62] E. Dagotto, T. Hotta, and A. Moreo, *Colossal magnetoresistant materials: the key role of phase separation*, Phys. Rep. **344**, 1 (2001).
- [63] D. F. Agterberg, M. Sigrist, and T. M. Rice, *Orbitally dependent superconductivity in Sr_2RuO_4* , Phys. Rev. Lett. **78**, 3374 (1997).
- [64] Y. Yu, A. K. C. Cheung, S. Raghu, and D. F. Agterberg, *Residual spin susceptibility in the spin-triplet orbital-singlet model*, Phys. Rev. B **98**, 184507 (2018).
- [65] S. Kashiwaya, K. Saitoh, H. Kashiwaya, M. Koyanagi, M. Sato, K. Yada, Y. Tanaka, and Y. Maeno, *Time-reversal invariant superconductivity of Sr_2RuO_4 revealed by Josephson effects*, Phys. Rev. B **100**, 094530 (2019), <https://link.aps.org/doi/10.1103/PhysRevB.100.094530>.
- [66] C. J. Lapp, G. Börner, and C. Timm, *Experimental consequences of Bogoliubov Fermi surfaces*, Phys. Rev. B (2019), to be published, arXiv:1909.10370.
- [67] R. Sharma, S. D. Edkins, Z. Wang, A. Kostin, C. Sow, Y. Maeno, A. P. Mackenzie, J. C. S. Davis, and V. Madhavan, *Momentum resolved superconducting energy gaps of Sr_2RuO_4 from quasiparticle interference imaging* (2019).
- [68] S. Ran, C. Eckberg, Q.-P. Ding, Y. Furukawa, T. Metz, S. R. Saha, I.-L. Liu, M. Zic, H. Kim, J. Paglione, and N. P. Butch, *Nearly ferromagnetic spin-triplet superconductivity*, Science **365**, 684 (2019), <https://science.sciencemag.org/content/365/6454/684>.
- [69] S. Ran, I.-L. Liu, Y. S. Eo, D. J. Campbell, P. M. Neves, W. T. Fuhrman, S. R. Saha, C. Eckberg, H. Kim, D. Graf, F. Balakirev, J. Singleton, J. Paglione, and N. P. Butch, *Extreme magnetic field-boosted superconductivity*, Nature Physics **15**, 1250 (2019).
- [70] D. Braithwaite, M. Valiska, G. Knebel, G. Lapertot, J.-P. Brison, A. Pourret, M. E. Zhitomirsky, J. Flouquet, F. Honda, and D. Aoki, *Multiple superconducting phases in a nearly ferromagnetic system*, Communications Physics **2**, 147 (2019).
- [71] I. M. Hayes, D. S. Wei, T. Metz, J. Zhang, Y. S. Eo, S. Ran, S. R. Saha, J. Collini, N. P. Butch, D. F. Agterberg, A. Kapitulnik, and J. Paglione, *Weyl superconductivity in UTe_2* (2020).
- [72] S. M. Thomas, F. B. Santos, M. H. Christensen, T. Asaba, F. Ronning, J. D. Thompson, E. D. Bauer, R. M. Fernandes, G. Fabbri, and P. F. S. Rosa, *Evidence for a pressure-induced antiferromagnetic quantum critical point in intermediate valence UTe_2* (2020), 2005.01659.
- [73] S. Bae, H. Kim, S. Ran, Y. S. Eo, I.-L. Liu, W. Fuhrman, J. Paglione, N. P. Butch, and S. Anlage, *Anomalous normal fluid response in a chiral superconductor* (2019), 1909.09032.
- [74] L. Jiao, S. Howard, S. Ran, Z. Wang, J. O. Rodriguez, M. Sigrist, Z. Wang, N. P. Butch, and V. Madhavan, *Chiral superconductivity in heavy-fermion metal UTe_2* , Nature **579**, 523 (2020).
- [75] D. Aoki, K. Ishida, and J. Flouquet, *Review of U-based ferromagnetic superconductors: Comparison between UGe_2 , URhGe , and UCoGe* , J. Phys. Soc. Jpn. **88**, 022001 (2019).
- [76] A. B. Shick and W. E. Pickett, *Spin-orbit coupling induced degeneracy in the anisotropic unconventional superconductor UTe_2* , Phys. Rev. B **100**, 134502 (2019).

- [77] Y. Xu, Y. Sheng, and Y.-F. Yang, *Quasi-two-dimensional Fermi surfaces and unitary spin-triplet pairing in the heavy fermion superconductor UTe_2* , Phys. Rev. Lett. **123**, 217002 (2019).
- [78] J. Ishizuka, S. Sumita, A. Daido, and Y. Yanase, *Insulator-metal transition and topological superconductivity in UTe_2 from a first-principles calculation*, Phys. Rev. Lett. **123**, 217001 (2019).
- [79] T. Metz, S. Bae, S. Ran, I.-L. Liu, Y. S. Eo, W. T. Fuhrman, D. F. Agterberg, S. Anlage, N. P. Butch, and J. Paglione, *Point-node gap structure of the spin-triplet superconductor UTe_2* , Phys. Rev. B **100**, 220504 (2019).
- [80] L. Miao, S. Liu, Y. Xu, E. C. Kotta, C.-J. Kang, S. Ran, J. Paglione, G. Kotliar, N. P. Butch, J. D. Denlinger, and L. A. Wray, *Low energy band structure and symmetries of UTe_2 from angle-resolved photoemission spectroscopy*, Phys. Rev. Lett. **124**, 076401 (2020).
- [81] S.-i. Fujimori, I. Kawasaki, Y. Takeda, H. Yamagami, A. Nakamura, Y. Homma, and D. Aoki, *Electronic structure of ute_2 studied by photoelectron spectroscopy*, Journal of the Physical Society of Japan **88**, 103701 (2019), <https://doi.org/10.7566/JPSJ.88.103701>.
- [82] A. Ramires and M. Sigrist, *Identifying detrimental effects for multiorbital superconductivity: Application to Sr_2RuO_4* , Phys. Rev. B **94**, 104501 (2016).
- [83] A. Ramires, D. F. Agterberg, and M. Sigrist, *Tailoring T_c by symmetry principles: The concept of superconducting fitness*, Phys. Rev. B **98**, 024501 (2018).
- [84] G. Knebel, W. Knafo, A. Pourret, Q. Niu, M. Vališka, D. Braithwaite, G. Lapertot, M. Nardone, A. Zitouni, S. Mishra, I. Sheikin, G. Seyfarth, J.-P. Brison, D. Aoki, and J. Flouquet, *Field-reentrant superconductivity close to a metamagnetic transition in the heavy-fermion superconductor ute_2* , Journal of the Physical Society of Japan **88**, 063707 (2019), <https://doi.org/10.7566/JPSJ.88.063707>.
- [85] D. Aoki, F. Honda, G. Knebel, D. Braithwaite, A. Nakamura, D. Li, Y. Homma, Y. Shimizu, Y. J. Sato, J.-P. Brison, and J. Flouquet, *Multiple superconducting phases and unusual enhancement of the upper critical field in ute_2* , Journal of the Physical Society of Japan **89**, 053705 (2020), <https://doi.org/10.7566/JPSJ.89.053705>.
- [86] W.-C. Lin, D. J. Campbell, S. Ran, I.-L. Liu, H. Kim, A. H. Nevidomskyy, D. Graf, N. P. Butch, and J. Paglione, *Tuning magnetic confinement of spin-triplet superconductivity* (2020), 2002.12885.
- [87] P. M. R. Brydon, D. F. Agterberg, H. Menke, and C. Timm, *Bogoliubov Fermi surfaces: General theory, magnetic order, and topology*, Phys. Rev. B **98**, 224509 (2018), <https://link.aps.org/doi/10.1103/PhysRevB.98.224509>.
- [88] P. M. R. Brydon, D. S. Abergel, D. F. Agterberg, and V. M. Yakovenko, *Loop currents and anomalous Hall effect from time-reversal symmetry-breaking superconductivity on the honeycomb lattice*, Phys. Rev. X **9**, 031025 (2019), <http://dx.doi.org/10.1103/PhysRevX.9.031025>.
- [89] A. Manchon, H. C. Koo, J. Nitta, S. M. Frolov, and R. A. Duine, *New perspectives for Rashba spin-orbit coupling*, Nature Materials **14**, 871 (2015), <https://doi.org/10.1038/nmat4360>.

- [90] M. Smidman, M. B. Salamon, H. Q. Yuan, and D. F. Agterberg, *Superconductivity and spin-orbit coupling in non-centrosymmetric materials: a review*, Reports on Progress in Physics **80**, 036501 (2017), <http://stacks.iop.org/0034-4885/80/i=3/a=036501>.
- [91] V. Baltz, A. Manchon, M. Tsoi, T. Moriyama, T. Ono, and Y. Tserkovnyak, *Antiferromagnetic spintronics*, Rev. Mod. Phys. **90**, 015005 (2018), <https://link.aps.org/doi/10.1103/RevModPhys.90.015005>.
- [92] X. Zhang, Q. Liu, J.-W. Luo, A. J. Freeman, and A. Zunger, *Hidden spin polarization in inversion-symmetric bulk crystals*, Nature Physics **10**, 387 (2014).
- [93] M. H. Fischer, M. Sigrist, D. F. Agterberg, and Y. Yanase, *Superconductivity and local inversion-symmetry breaking*, Annual Review of Condensed Matter Physics **14** (2023), <https://doi.org/10.1146/annurev-conmatphys-040521-042511>.
- [94] T. Yoshida, M. Sigrist, and Y. Yanase, *Pair-density wave states through spin-orbit coupling in multilayer superconductors*, Phys. Rev. B **86**, 134514 (2012).
- [95] S. Khim, J. F. Landaeta, J. Banda, N. Bannor, M. Brando, P. M. R. Brydon, D. Hafner, R. K uchler, R. Cardoso-Gil, U. Stockert, A. P. Mackenzie, D. F. Agterberg, C. Geibel, and E. Hassinger, *Field-induced transition within the superconducting state of CeRh₂As₂*, Science **373**, 1012 (2021), <https://www.science.org/doi/abs/10.1126/science.abe7518>.
- [96] J. F. Landaeta, P. Khanenko, D. C. Cavanagh, C. Geibel, S. Khim, S. Mishra, I. Sheikin, P. M. R. Brydon, D. F. Agterberg, M. Brando, and E. Hassinger, *Field-Angle Dependence Reveals Odd-Parity Superconductivity in CeRh₂As₂*, Phys. Rev. X **12**, 031001 (2022), <https://link.aps.org/doi/10.1103/PhysRevX.12.031001>.
- [97] D. C. Cavanagh, T. Shishidou, M. Weinert, P. M. R. Brydon, and D. F. Agterberg, *Nonsymmetric Symmetry and Field-Driven Odd-Parity Pairing in CeRh₂As₂*, Physical Review B **105** (2022), <http://dx.doi.org/10.1103/PhysRevB.105.L020505>.
- [98] L. Yuan, Q. Liu, X. Zhang, J.-W. Luo, S.-S. Li, and A. Zunger, *Uncovering and tailoring hidden Rashba spin-orbit splitting in centrosymmetric crystals*, Nature Communications **10** (2019), <https://doi.org/10.1038/41467-019-08836-4>.
- [99] P. Li and I. Appelbaum, *Illuminating "spin-polarized" bloch wave-function projection from degenerate bands in decomposable centrosymmetric lattices*, Phys. Rev. B **97**, 125434 (2018), <https://link.aps.org/doi/10.1103/PhysRevB.97.125434>.
- [100] Y. Nakamura and Y. Yanase, *Odd-parity superconductivity in bilayer transition metal dichalcogenides*, Phys. Rev. B **96**, 054501 (2017).
- [101] P. W. Anderson, *Structure of "triplet" superconducting energy gaps*, Phys. Rev. B **30**, 4000 (1984).
- [102] C. J. Bradley and A. P. Cracknell, *The Mathematical Theory of Symmetry in Solids* ((Oxford University Press), 1972).
- [103] P. Zhang, K. Yaji, T. Hashimoto, Y. Ota, T. Kondo, K. Okazaki, Z. Wang, J. Wen, G. D. Gu, H. Ding, and S. Shin, *Observation of topological superconductivity on the surface of an iron-based superconductor*, Science **360**, 182 (2018), <https://science.sciencemag.org/content/360/6385/182>.

- [104] M. M. Hirschmann, A. Leonhardt, B. Kilic, D. H. Fabini, and A. P. Schnyder, *Symmetry-enforced band crossings in tetragonal materials: Dirac and Weyl degeneracies on points, lines, and planes*, Phys. Rev. Mater. **5**, 054202 (2021), <https://link.aps.org/doi/10.1103/PhysRevMaterials.5.054202>.
- [105] A. Leonhardt, M. M. Hirschmann, N. Heinsdorf, X. Wu, D. H. Fabini, and A. P. Schnyder, *Symmetry-enforced topological band crossings in orthorhombic crystals: Classification and materials discovery*, Phys. Rev. Mater. **5**, 124202 (2021), <https://link.aps.org/doi/10.1103/PhysRevMaterials.5.124202>.
- [106] M. R. Norman, *Odd parity and line nodes in heavy-fermion superconductors*, Physical Review B **52**, 15093 (1995), <https://doi.org/10.1103/physrevb.52.15093>.
- [107] T. Micklitz and M. Norman, *Symmetry-enforced line nodes in unconventional superconductors*, Physical Review Letters **118** (2017), <https://doi.org/10.1103/physrevlett.118.207001>.
- [108] T. Micklitz and M. R. Norman, *Nodal lines and nodal loops in nonsymmorphic odd-parity superconductors*, Physical Review B **95** (2017), <https://doi.org/10.1103/physrevb.95.024508>.
- [109] A. Daido, T. Yoshida, and Y. Yanase, Z_4 Topological Superconductivity in UCoGe, Phys. Rev. Lett. **122**, 227001 (2019), <https://link.aps.org/doi/10.1103/PhysRevLett.122.227001>.
- [110] Y. Yanase, *Nonsymmorphic Weyl superconductivity in UPt₃ based on E_{2u} representation*, Phys. Rev. B **94**, 174502 (2016), <https://link.aps.org/doi/10.1103/PhysRevB.94.174502>.
- [111] S. Sumita and Y. Yanase, *Unconventional superconducting gap structure protected by space group symmetry*, Phys. Rev. B **97**, 134512 (2018), <https://link.aps.org/doi/10.1103/PhysRevB.97.134512>.
- [112] S. Kobayashi, Y. Yanase, and M. Sato, *Topologically stable gapless phases in nonsymmorphic superconductors*, Phys. Rev. B **94**, 134512 (2016), <https://link.aps.org/doi/10.1103/PhysRevB.94.134512>.
- [113] S. Kobayashi, K. Shiozaki, Y. Tanaka, and M. Sato, *Topological blount's theorem of odd-parity superconductors*, Phys. Rev. B **90**, 024516 (2014), <https://link.aps.org/doi/10.1103/PhysRevB.90.024516>.
- [114] T. Micklitz and M. R. Norman, *Odd parity and line nodes in nonsymmorphic superconductors*, Phys. Rev. B **80**, 100506(R) (2009), <https://link.aps.org/doi/10.1103/PhysRevB.80.100506>.
- [115] J. R. Badger, Y. Quan, M. C. Staab, S. Sumita, A. Rossi, K. P. Devlin, K. Neubauer, D. S. Shulman, J. C. Fettinger, P. Klavins, S. M. Kauzlarich, D. Aoki, I. M. Vishik, W. E. Pickett, and V. Taufour, *Dirac lines and loop at the fermi level in the time-reversal symmetry breaking superconductor LaNiGa₂*, Communications Physics **5** (2022), <https://doi.org/10.1038/s42005-021-00771-5>.

- [116] Y. Mizuguchi, *Review of superconductivity in BiS₂-based layered materials*, Journal of Physics and Chemistry of Solids **84**, 34 (2015), focus issue on the Study of matter at extreme conditions and related phenomena, <https://www.sciencedirect.com/science/article/pii/S0022369714002157>.
- [117] G. R. Stewart, *Superconductivity in iron compounds*, Rev. Mod. Phys. **83**, 1589 (2011), <https://link.aps.org/doi/10.1103/RevModPhys.83.1589>.
- [118] R. Joynt and L. Taillefer, *The superconducting phases of UPt₃*, Rev. Mod. Phys. **74**, 235 (2002), <https://link.aps.org/doi/10.1103/RevModPhys.74.235>.
- [119] L. Fu, *Parity-breaking phases of spin-orbit-coupled metals with gyrotropic, ferroelectric, and multipolar orders*, Phys. Rev. Lett. **115**, 026401 (2015), <https://link.aps.org/doi/10.1103/PhysRevLett.115.026401>.
- [120] P. M. R. Brydon, L. Wang, M. Weinert, and D. F. Agterberg, *Pairing of $j = 3/2$ fermions in half-Heusler superconductors*, Phys. Rev. Lett. **116**, 177001 (2016), <https://link.aps.org/doi/10.1103/PhysRevLett.116.177001>.
- [121] C. Wang, B. Lian, X. Guo, J. Mao, Z. Zhang, D. Zhang, B.-L. Gu, Y. Xu, and W. Duan, *Type-II Ising superconductivity in two-dimensional materials with spin-orbit coupling*, Phys. Rev. Lett. **123**, 126402 (2019).
- [122] J. Falson, Y. Xu, M. Liao, Y. Zang, K. Zhu, C. Wang, Z. Zhang, H. Liu, W. Duan, K. He, H. Liu, J. H. Smet, D. Zhang, and Q.-K. Xue, *Type-II Ising pairing in few-layer stanene*, Science **367**, 1454 (2020).
- [123] K. V. Samokhin, *Symmetry of superconducting pairing in non-pseudospin electron bands*, Phys. Rev. B **100**, 054501 (2019), <https://link.aps.org/doi/10.1103/PhysRevB.100.054501>.
- [124] K. V. Samokhin, *Exotic interband pairing in multiband superconductors*, Phys. Rev. B **101**, 214524 (2020), <https://link.aps.org/doi/10.1103/PhysRevB.101.214524>.
- [125] K. V. Samokhin, *Spin Susceptibility of Superconductors with Strong Spin-Orbit Coupling*, Physical Review B **103**, 174505 (2021), <https://doi.org/10.1103/physrevb.103.174505>.
- [126] M. Sigrist and K. Ueda, *Phenomenological theory of unconventional superconductivity*, Rev. Mod. Phys. **63**, 239 (1991), <http://link.aps.org/doi/10.1103/RevModPhys.63.239>.
- [127] L. P. Gor'kov and E. I. Rashba, *Superconducting 2d system with lifted spin degeneracy: Mixed singlet-triplet state*, Phys. Rev. Lett. **87**, 037004 (2001), <https://link.aps.org/doi/10.1103/PhysRevLett.87.037004>.
- [128] M. I. Aroyo, J. M. Perez-Mato, C. Capillas, E. Kroumova, S. Ivantchev, G. Madariaga, A. Kirov, and H. Wondratschek, *Bilbao crystallographic server: I. databases and crystallographic computing programs*, Zeitschrift für Kristallographie - Crystalline Materials **221**, 15 (2006), <https://doi.org/10.1524/zkri.2006.221.1.15>.
- [129] M. I. Aroyo, A. Kirov, C. Capillas, J. M. Perez-Mato, and H. Wondratschek, *Bilbao Crystallographic Server. II. Representations of crystallographic point groups and space groups*, Acta Crystallographica Section A **62**, 115 (2006), <https://doi.org/10.1107/S0108767305040286>.

- [130] H. T. Stokes, B. J. Campbell, and R. Cordes, *Tabulation of irreducible representations of the crystallographic space groups and their superspace extensions*, Acta Crystallographica Section A **69**, 388 (2013), <https://doi.org/10.1107/S0108767313007538>.
- [131] Y. X. Zhao and A. P. Schnyder, *Nonsymmorphic symmetry-required band crossings in topological semimetals*, Phys. Rev. B **94**, 195109 (2016), <https://link.aps.org/doi/10.1103/PhysRevB.94.195109>.
- [132] D. Huang and J. E. Hoffman, *Monolayer FeSe on SrTiO₃*, Annual Review of Condensed Matter Physics **8**, 311 (2017), <https://doi.org/10.1146/annurev-conmatphys-031016-025242>.
- [133] J. P. Ruf, H. Paik, N. J. Schreiber, H. P. Nair, L. Miao, J. K. Kawasaki, J. N. Nelson, B. D. Faeth, Y. Lee, B. H. Goodge, B. Pamuk, C. J. Fennie, L. F. Kourkoutis, D. G. Schlom, and K. M. Shen, *Strain-stabilized superconductivity*, Nature Communications **12** (2021), <https://doi.org/10.1038/41467-020-20252-7>.
- [134] M. Uchida, T. Nomoto, M. Musashi, R. Arita, and M. Kawasaki, *Superconductivity in Uniquely Strained RuO₂ Films*, Phys. Rev. Lett. **125**, 147001 (2020), <https://link.aps.org/doi/10.1103/PhysRevLett.125.147001>.
- [135] L. Šmejkal, J. Sinova, and T. Jungwirth, *Emerging research landscape of altermagnetism*, Phys. Rev. X **12**, 040501 (2022), <https://link.aps.org/doi/10.1103/PhysRevX.12.040501>.
- [136] E. I. Blount, *Symmetry properties of triplet superconductors*, Phys. Rev. B **32**, 2935 (1985), <https://link.aps.org/doi/10.1103/PhysRevB.32.2935>.
- [137] K. Samokhin, *On the pseudospin description of the electron Bloch bands*, Annals of Physics **407**, 179 (2019), <https://doi.org/10.1016/j.aop.2019.04.016>.
- [138] D. C. Cavanagh, D. F. Agterberg, and P. M. R. Brydon, *Pair-breaking in superconductors with strong spin-orbit coupling* (2022), <https://arxiv.org/abs/2207.01191>.
- [139] Y. Yanase and K. Shiozaki, *Möbius topological superconductivity in UPt₃*, Phys. Rev. B **95**, 224514 (2017), <https://link.aps.org/doi/10.1103/PhysRevB.95.224514>.
- [140] A. V. Chubukov, O. Vafek, and R. M. Fernandes, *Displacement and annihilation of dirac gap nodes in d-wave iron-based superconductors*, Phys. Rev. B **94**, 174518 (2016), <https://link.aps.org/doi/10.1103/PhysRevB.94.174518>.
- [141] D. F. Agterberg, P. M. R. Brydon, and C. Timm, *Bogoliubov Fermi surfaces in superconductors with broken time-reversal symmetry*, Phys. Rev. Lett. **118**, 127001 (2017).
- [142] L. Fu and E. Berg, *Odd-parity topological superconductors: Theory and application to Cu_xBi₂Se₃*, Phys. Rev. Lett. **105**, 097001 (2010), <https://link.aps.org/doi/10.1103/PhysRevLett.105.097001>.
- [143] S. Qin, C. Fang, F.-C. Zhang, and J. Hu, *Spin-triplet superconductivity in nonsymmorphic crystals* (2022), <https://arxiv.org/abs/2208.09409>.
- [144] O. Vafek and A. V. Chubukov, *Hund interaction, spin-orbit coupling, and the mechanism of superconductivity in strongly hole-doped iron pnictides*, Phys. Rev. Lett. **118**, 087003 (2017), <https://link.aps.org/doi/10.1103/PhysRevLett.118.087003>.

- [145] A. K. C. Cheung and D. F. Agterberg, *Superconductivity in the presence of spin-orbit interactions stabilized by Hund coupling*, Phys. Rev. B **99**, 024516 (2019), <https://link.aps.org/doi/10.1103/PhysRevB.99.024516>.
- [146] C. Wang, Y. Xu, and W. Duan, *Ising Superconductivity and Its Hidden Variants*, Accounts of Materials Research **2**, 526 (2021), <https://doi.org/10.1021/accountsmr.1c00068>.
- [147] A. Skurativska, M. Sigrist, and M. H. Fischer, *Spin response and topology of a staggered-Rashba superconductor*, Phys. Rev. Res. **3**, 033133 (2021), <https://link.aps.org/doi/10.1103/PhysRevResearch.3.033133>.
- [148] K. Hoshi, R. Kurihara, Y. Goto, M. Tokunaga, and Y. Mizuguchi, *Extremely high upper critical field in BiCh₂-based (Ch: S and Se) layered superconductor LaO_{0.5}F_{0.5}BiS_{2-x}Se_x (x = 0.22 and 0.69)*, Scientific Reports **12** (2022), <https://doi.org/10.1038/41598-021-04393-3>.
- [149] H. Usui, K. Suzuki, and K. Kuroki, *Minimal electronic models for superconducting BiS₂ layers*, Phys. Rev. B **86**, 220501(R) (2012), <https://link.aps.org/doi/10.1103/PhysRevB.86.220501>.
- [150] S. Cobo-Lopez, M. S. Bahramy, R. Arita, A. Akbari, and I. Eremin, *Spin-orbit coupling, minimal model and potential Cooper-pairing from repulsion in BiS₂-superconductors*, New Journal of Physics **20**, 043029 (2018), <https://dx.doi.org/10.1088/1367-2630/aaaf87>.
- [151] M. Weinert, G. Schneider, R. Podloucky, and J. Redinger, *FLAPW: Applications and implementations*, J. Phys. Condens. Matter **21**, 084201 (2009).
- [152] J. P. Perdew, K. Burke, and M. Ernzerhof, *Generalized Gradient Approximation Made Simple*, Phys. Rev. Lett. **77**, 3865 (1996).
- [153] Y. Mizuguchi, S. Demura, K. Deguchi, Y. Takano, H. Fujihisa, Y. Gotoh, H. Izawa, and O. Miura, *Superconductivity in Novel BiS₂-Based Layered Superconductor LaO_{1-x}F_xBiS₂*, Journal of the Physical Society of Japan **81**, 114725 (2012), <https://doi.org/10.1143/JPSJ.81.114725>.
- [154] J. lei Zhang, L. Jiao, Y. Chen, and H. qiu Yuan, *Universal behavior of the upper critical field in iron-based superconductors*, Frontiers of Physics **6**, 463 (2011), <https://doi.org/10.1007/11467-011-0235-7>.
- [155] P. Fulde and R. A. Ferrell, *Superconductivity in a strong spin-exchange field*, Phys. Rev. **135**, A550 (1964).
- [156] A. Larkin and Y. Ovchinnikov, *Inhomogeneous state of superconductors*, Sov. Phys. JETP **20**, 762 (1965).
- [157] D. F. Agterberg, J. S. Davis, S. D. Edkins, E. Fradkin, D. J. Van Harlingen, S. A. Kivelson, P. A. Lee, L. Radzihovsky, J. M. Tranquada, and Y. Wang, *The physics of pair-density waves: Cuprate superconductors and beyond*, Annual Review of Condensed Matter Physics **11**, 231 (2020), <https://doi.org/10.1146/annurev-conmatphys-031119-050711>.
- [158] M. Sigrist, *Introduction to Unconventional Superconductivity*, AIP Conference Proceedings **789**, 165 (2005), <https://aip.scitation.org/doi/abs/10.1063/1.2080350>.

- [159] V. Mineev and K. Samokhin, *Introduction to Unconventional Superconductivity* (Gordon and Breach Science Publishers, 1999), ISBN 90-5699-209-0.
- [160] K. Machida, T. Ohmi, and M.-A. Ozaki, *Anisotropy of Upper Critical Fields for d- and p-Wave Pairing Superconductivity*, Journal of the Physical Society of Japan **54**, 1552 (1985), <https://doi.org/10.1143/JPSJ.54.1552>.
- [161] J. A. Sauls, *The order parameter for the superconducting phases of UPt_3* , Advances in Physics **43**, 113 (1994), <https://doi.org/10.1080/00018739400101475>.
- [162] C. H. Choi and J. A. Sauls, *Identification of odd-parity superconductivity in UPt_3 from paramagnetic effects on the upper critical field*, Phys. Rev. Lett. **66**, 484 (1991), <https://link.aps.org/doi/10.1103/PhysRevLett.66.484>.
- [163] H. Tou, Y. Kitaoka, K. Asayama, N. Kimura, Y. Onuki, E. Yamamoto, and K. Maezawa, *Odd-Parity Superconductivity with Parallel Spin Pairing in UPt_3 : Evidence from ^{195}Pt Knight Shift Study*, Phys. Rev. Lett. **77**, 1374 (1996), <https://link.aps.org/doi/10.1103/PhysRevLett.77.1374>.
- [164] B. J. Wieder, Y. Kim, A. M. Rappe, and C. L. Kane, *Double dirac semimetals in three dimensions*, Phys. Rev. Lett. **116**, 186402 (2016), <https://link.aps.org/doi/10.1103/PhysRevLett.116.186402>.
- [165] B. Bradlyn, J. Cano, Z. Wang, M. G. Vergniory, C. Felser, R. J. Cava, and B. A. Bernevig, *Beyond dirac and weyl fermions: Unconventional quasiparticles in conventional crystals*, Science **353**, aaf5037 (2016), <https://www.science.org/doi/abs/10.1126/science.aaf5037>.
- [166] M. Samsel-Czekala, S. Elgazzar, P. M. Oppeneer, E. Talik, W. Walerczyk, and R. Troć, *The electronic structure of $UCoGe$ by ab initio calculations and XPS experiment*, Journal of Physics: Condensed Matter **22**, 015503 (2009), <https://dx.doi.org/10.1088/0953-8984/22/1/015503>.
- [167] S.-I. Fujimori, T. Ohkochi, I. Kawasaki, A. Yasui, Y. Takeda, T. Okane, Y. Saitoh, A. Fujimori, H. Yamagami, Y. Haga, E. Yamamoto, and Y. Onuki, *Electronic structures of ferromagnetic superconductors UGe_2 and $UCoGe$ studied by angle-resolved photoelectron spectroscopy*, Phys. Rev. B **91**, 174503 (2015), <https://link.aps.org/doi/10.1103/PhysRevB.91.174503>.
- [168] A. Daido, T. Yoshida, and Y. Yanase, *Z_4 Topological Superconductivity in $UCoGe$* , Phys. Rev. Lett. **122**, 227001 (2019), <https://link.aps.org/doi/10.1103/PhysRevLett.122.227001>.
- [169] G. Bastien, A. Gourgout, D. Aoki, A. Pourret, I. Sheikin, G. Seyfarth, J. Flouquet, and G. Knebel, *Lifshitz transitions in the ferromagnetic superconductor $ucoge$* , Phys. Rev. Lett. **117**, 206401 (2016), <https://link.aps.org/doi/10.1103/PhysRevLett.117.206401>.
- [170] F. Canepa, P. Manfrinetti, M. Pani, and A. Palenzona, *Structural and transport properties of some UTX compounds where $T = Fe, Co, Ni$ and $X = Si, Ge$* , Journal of Alloys and Compounds **234**, 225 (1996), <https://www.sciencedirect.com/science/article/pii/0925838895020373>.
- [171] M. Kawamura, *FermiSurfer: Fermi-surface viewer providing multiple representation schemes*, Computer Physics Communications **239**, 197 (2019), <https://www.sciencedirect.com/science/article/pii/S0010465519300347>.

- [172] Y. Shimizu, D. Braithwaite, D. Aoki, B. Salce, and J.-P. Brison, *Spin-Triplet p-Wave Superconductivity Revealed under High Pressure in UBe₁₃*, Phys. Rev. Lett. **122**, 067001 (2019), <https://link.aps.org/doi/10.1103/PhysRevLett.122.067001>.
- [173] K. Ma, K. Gornicka, R. Lefè vre, Y. Yang, H. M. Rønnow, H. O. Jeschke, T. Klimczuk, and F. O. von Rohr, *Superconductivity with High Upper Critical Field in the Cubic Centrosymmetric η -Carbide Nb₄Rh₂C_{1- δ}* , ACS Materials Au **1**, 55 (2021), <https://doi.org/10.1021/acsmaterialsau.1c00011>.
- [174] B.-B. Ruan, M.-H. Zhou, Q.-S. Yang, Y.-D. Gu, M.-W. Ma, G.-F. Chen, and Z.-A. Ren, *Superconductivity with a Violation of Pauli Limit and Evidences for Multigap in η -Carbide Type Ti₄Ir₂O*, Chinese Physics Letters **39**, 027401 (2022), <https://doi.org/10.1088/0256-307x/39/027401>.
- [175] B. P. Abbott, R. Abbott, T. D. Abbott, M. R. Abernathy, F. Acernese, K. Ackley, C. Adams, T. Adams, P. Addesso, R. X. Adhikari, V. B. Adya, C. Affeldt, M. Agathos, K. Agatsuma, N. Aggarwal, et al. (LIGO Scientific Collaboration and Virgo Collaboration), *Observation of gravitational waves from a binary black hole merger*, Phys. Rev. Lett. **116**, 061102 (2016), <https://link.aps.org/doi/10.1103/PhysRevLett.116.061102>.
- [176] B. P. Abbott, R. Abbott, T. D. Abbott, S. Abraham, F. Acernese, K. Ackley, C. Adams, R. X. Adhikari, V. B. Adya, C. Affeldt, M. Agathos, K. Agatsuma, N. Aggarwal, O. D. Aguiar, L. Aiello, et al. (LIGO Scientific Collaboration and Virgo Collaboration), *Gwtc-1: A gravitational-wave transient catalog of compact binary mergers observed by ligo and virgo during the first and second observing runs*, Phys. Rev. X **9**, 031040 (2019), <https://link.aps.org/doi/10.1103/PhysRevX.9.031040>.
- [177] R. Abbott, T. D. Abbott, S. Abraham, F. Acernese, K. Ackley, A. Adams, C. Adams, R. X. Adhikari, V. B. Adya, C. Affeldt, M. Agathos, K. Agatsuma, N. Aggarwal, O. D. Aguiar, L. Aiello, et al. (LIGO Scientific Collaboration and Virgo Collaboration), *Gwtc-2: Compact binary coalescences observed by ligo and virgo during the first half of the third observing run*, Phys. Rev. X **11**, 021053 (2021), <https://link.aps.org/doi/10.1103/PhysRevX.11.021053>.
- [178] T. L. S. Collaboration, the Virgo Collaboration, the KAGRA Collaboration, R. Abbott, T. D. Abbott, F. Acernese, K. Ackley, C. Adams, N. Adhikari, R. X. Adhikari, V. B. Adya, C. Affeldt, D. Agarwal, M. Agathos, K. Agatsuma, et al., *Gwtc-3: Compact binary coalescences observed by ligo and virgo during the second part of the third observing run* (2021), 2111.03606.
- [179] R. Abbott, T. D. Abbott, F. Acernese, K. Ackley, C. Adams, N. Adhikari, R. X. Adhikari, V. B. Adya, C. Affeldt, D. Agarwal, M. Agathos, K. Agatsuma, N. Aggarwal, O. D. Aguiar, L. Aiello, et al. (LIGO Scientific Collaboration, Virgo Collaboration, and KAGRA Collaboration), *Population of merging compact binaries inferred using gravitational waves through gwtc-3*, Phys. Rev. X **13**, 011048 (2023), <https://link.aps.org/doi/10.1103/PhysRevX.13.011048>.
- [180] R. Abbott, T. D. Abbott, F. Acernese, K. Ackley, C. Adams, N. Adhikari, R. X. Adhikari, V. B. Adya, C. Affeldt, D. Agarwal, M. Agathos, K. Agatsuma, N. Aggarwal, O. D. Aguiar, L. Aiello, et al. (LIGO Scientific Collaboration, Virgo Collaboration, and KAGRA Collaboration), *Constraints on dark photon dark matter using data from ligo's and virgo's third*

- observing run*, Phys. Rev. D **105**, 063030 (2022), <https://link.aps.org/doi/10.1103/PhysRevD.105.063030>.
- [181] S. J. Kapadia, S. Caudill, J. D. E. Creighton, W. M. Farr, G. Mendell, A. Weinstein, K. Cannon, H. Fong, P. Godwin, R. K. L. Lo, R. Magee, D. Meacher, C. Messick, S. R. Mohite, D. Mukherjee, et al., *A self-consistent method to estimate the rate of compact binary coalescences with a poisson mixture model*, Classical and Quantum Gravity **37**, 045007 (2020), <https://doi.org/10.1088/1361-6382/2fab5f2d>.
- [182] F. Rosenblatt, *The perceptron: a probabilistic model for information storage and organization in the brain.*, Psychological review **65** **6**, 386 (1958).
- [183] M. Abadi, A. Agarwal, P. Barham, E. Brevdo, Z. Chen, C. Citro, G. S. Corrado, A. Davis, J. Dean, M. Devin, S. Ghemawat, I. Goodfellow, A. Harp, G. Irving, M. Isard, et al., *TensorFlow: Large-scale machine learning on heterogeneous systems* (2015), software available from tensorflow.org, <https://www.tensorflow.org/>.
- [184] A. Paszke, S. Gross, F. Massa, A. Lerer, J. Bradbury, G. Chanan, T. Killeen, Z. Lin, N. Gimelshein, L. Antiga, A. Desmaison, A. Kopf, E. Yang, Z. DeVito, M. Raison, et al., *Pytorch: An imperative style, high-performance deep learning library*, in *Advances in Neural Information Processing Systems 32* (Curran Associates, Inc., 2019), pp. 8024–8035, <http://papers.neurips.cc/paper/9015-pytorch-an-imperative-style-high-performance-deep-learning-library.pdf>.
- [185] D. Davis, T. B. Littenberg, I. M. Romero-Shaw, M. Millhouse, J. McIver, F. D. Renzo, and G. Ashton, *Subtracting glitches from gravitational-wave detector data during the third ligo-virgo observing run*, Classical and Quantum Gravity **39**, 245013 (2022), <https://dx.doi.org/10.1088/1361-6382/aca238>.
- [186] J. Glanzer, S. Banagiri, S. B. Coughlin, S. Soni, M. Zevin, C. P. L. Berry, O. Patane, S. Bahaadini, N. Rohani, K. Crowston, V. Kalogera, C. østerlund, L. Trouille, and A. Katsaggelos, *Data quality up to the third observing run of advanced ligo: Gravity spy glitch classifications*, Classical and Quantum Gravity **40**, 065004 (2023), <https://dx.doi.org/10.1088/1361-6382/acb633>.
- [187] M. Zevin, S. Coughlin, S. Bahaadini, E. Besler, N. Rohani, S. Allen, M. Cabero, K. Crowston, A. K. Katsaggelos, S. L. Larson, T. K. Lee, C. Lintott, T. B. Littenberg, A. Lundgren, C. østerlund, et al., *Gravity spy: integrating advanced ligo detector characterization, machine learning, and citizen science*, Classical and Quantum Gravity **34**, 064003 (2017), <https://dx.doi.org/10.1088/1361-6382/aa5cea>.
- [188] M. Cabero, A. Lundgren, A. H. Nitz, T. Dent, D. Barker, E. Goetz, J. S. Kissel, L. K. Nuttall, P. Schale, R. Schofield, and D. Davis, *Blip glitches in advanced ligo data*, Classical and Quantum Gravity **36**, 155010 (2019), <https://dx.doi.org/10.1088/1361-6382/ab2e14>.
- [189] X. Xu and E. R. Siegel, *Dark matter in the solar system* (2008), 0806.3767.
- [190] I. B. KHRIPLOVICH, *DENSITY OF DARK MATTER IN THE SOLAR SYSTEM AND PERIHELION PRECESSION OF PLANETS*, International Journal of Modern Physics D **16**, 1475 (2007), <https://doi.org/10.1142/S0218271807010869>.

Appendix

A.1 ML model performance figures

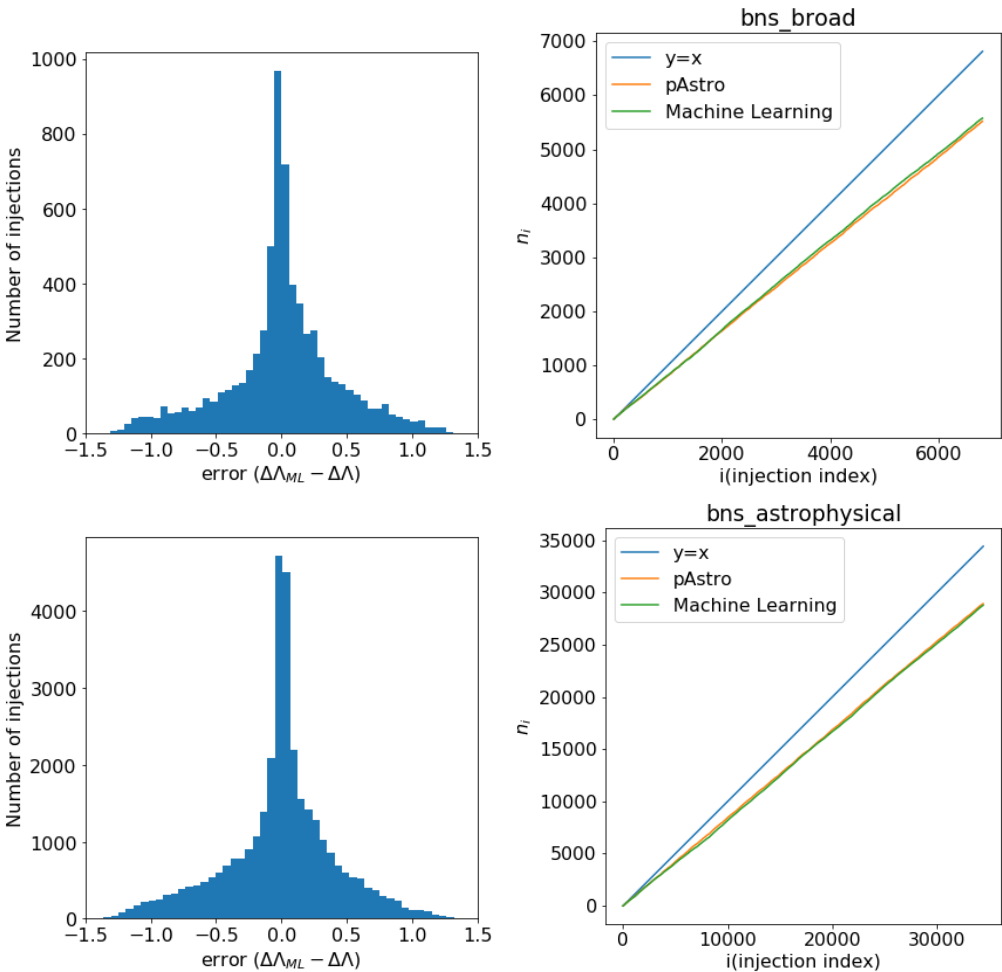


Figure A-6: Performance of ML models for BNS injections.

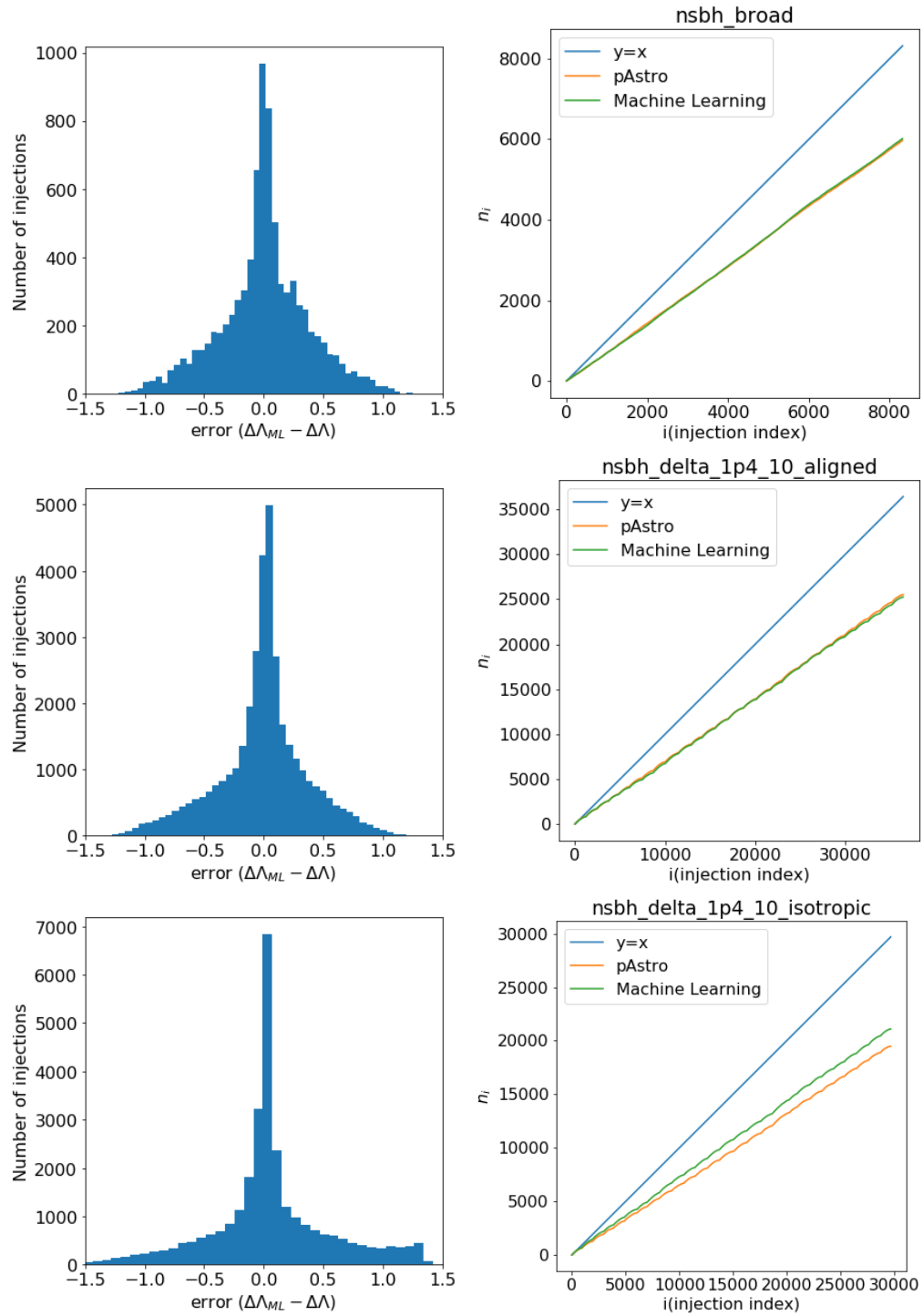


Figure A-7: Performance of ML models for NSBH injections.